Spring 5-31-2019

The Investigation of Methylidyne Radical (CH) Reactions with Furan, 2-Methylfuran, and 2,5-Dimethlyfuran and the Photoionization and Photodissociation of Valeric Acid

Erica Carrasco
ericarrrasco@gmail.com

The Investigation of Methylidyne Radical (CH) Reactions with Furan, 2-Methylfuran, and 2,5-Dimethlyfuran and the Photoionization and Photodissociation of Valeric Acid

A thesis presented to the faculty of the

Department of Chemistry at the

University of San Francisco

in partial fulfillment of the requirements for the

Degree of Master of Science in Chemistry

Written by

Erica Carrasco

Bachelor of Science in Biochemistry

Loyola Marymount University

05/09/2019

The Investigation of Methylidyne Radical (CH) Reactions with Furan, 2-Methylfuran, and 2,5-Dimethlyfuran and the Photoionization and Photodissociation of Valeric Acid

Thesis written by Erica Carrasco

This thesis is written under the guidance of the Faculty Advisory Committee, and approved by all its members, has been accepted in partial fulfillment of the requirements for the degree of

Master of Science in Chemistry
at
the University of San Francisco

Thesis Committee

Giovanni Meloni, Ph.D.
Research Advisor

Ryan West, Ph.D.
Assistant Professor

William Melaugh, Ph.D.
Professor

Marcelo Camperi, Ph.D.
Dean, College of Arts and Sciences

Acknowledgements

A sincere thank you to my research advisor Dr. Giovanni Meloni for the wonderful opportunity to work in his research lab. My experience as his student has taught me invaluable lessons that will continue to benefit me in my future career as a scientist and researcher. I am immensely grateful for his teachings and support that have fostered my ambition to pursue a career in the scientific research field. I would also like to thank our collaborators at the Paul Scherrer Institute for their support in the PEPICO experiments. A special thank you to my research group, my experience would not have been as fulfilling without your daily support.

I would like to thank all the faculty and staff of the Chemistry Department at USF for a wonderful two years. Thank you to my Thesis committee, Dr. Ryan West and Dr. William Melaugh, for taking the time to review and provide guidance for my thesis. I want to give a special thank you to Deidre Shymanski for going above and beyond to help me and my fellow graduate students in any way she could.

Finally, a huge thank you to all my friends and family for their unwavering support, encouragement, and love. I truly could not have done it without all of you by my side.

Table of Contents

Abstract

This thesis presents the combustion study of three furanic compounds using synchrotron radiation coupled with multiplexed photoionization mass spectrometry at 298 K. The experiments were performed at the Chemical Dynamics Beamline 9.0.2 at the Advanced Light Source of the Lawrence Berkeley National Laboratory. The reactions of the three furanic compounds with methylidyne (CH) radicals were analyzed based on their photoionization spectra and kinetic profiles.

Additionally, the unimolecular dissociation of valeric acid was also studied and presented in this work using the double imaging photoelectron photoion spectrometry (i2PEPICO) coupled with synchrotron radiation from the VUV beamline. The experiments were carried out at the Swiss Light Source of the Paul Scherrer Institute in Villigen, Switzerland. The unimolecular dissociation dynamics of valeric acid were studied by analyzing ions with a well-defined internal energy state and used to derive thermochemical values for unknown reaction species.

Chapter 1 of this thesis discuss the importance of biofuel research due to the negative impacts of fossil fuel combustion on the environment. The experimental methods and apparatuses of the ALS and SLS beamlines are described in detail in Chapter 2. In Chapter 3, the theory behind the experimental and computational methods used to analyze the experiments presented in this thesis are thoroughly explained. The combustion study of furan and 2-methlyfuran with CH ($X^2\Pi$) radicals is presented in Chapter 4. Chapter 5 continues with the combustion study of 2,5-dimethlyfuran with CH ($X^2\Pi$) and CD radicals. To conclude, Chapter 6 presents the photoionization and photodissociation study of valeric acid.

Chapter 1 Introduction

1.1 Greenhouse Gas Emissions

To sustain life, the Earth's surface relies on the warming from greenhouse gases (GHG) to maintain a temperature balance.[1] However, in the recent century the average surface temperature of the Earth has risen 2 ℉, resulting in overheating and global warming.[2] The increase in anthropogenic GHG emissions, such as carbon dioxide, water vapor, and methane, is the main cause of the temperature rise.[1] Figure 1 illustrates the differences between a natural and human enhanced greenhouse gas effect. Anthropogenic GHG are trapping more heat and warming the Earth by blocking the infrared radiation emitted by the Earth's surface that is supposed to be released into space.[1] Both NASA and NOAA report that the warmest five years in history have occurred since 2010.2 Temperature increase has and will continue to lead to climate and weather changes, such as floods, droughts, heat waves.[1]

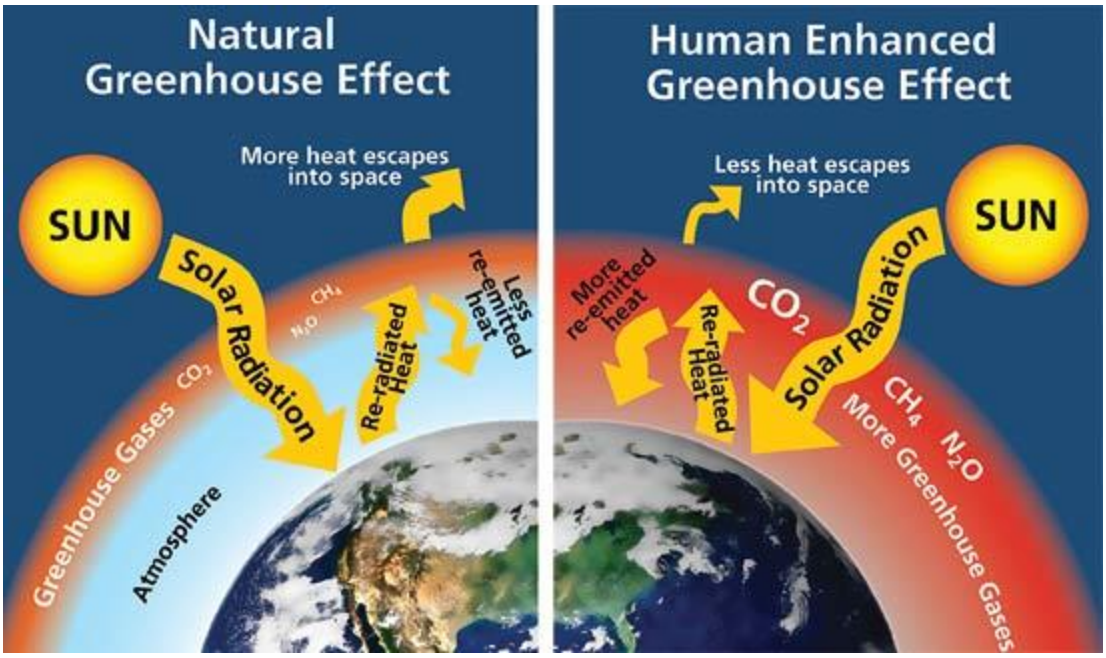

Figure 1.1 Comparison of Natural and Human Enhanced GHG Effect[2]

Even though GHG gases currently only make up 0.5% of the Earth's atmosphere, their impact is very substantial.[3] All greenhouse gas emissions stay in the atmosphere for thousands of years and diffuse well enough that the concentration of each gas is the same across the world.[4] Therefore, the negative effects of these emissions will be seen globally and affect all human life.[4] For example, the increase in carbon dioxide (CO_2) absorption by the oceans has already lead to an increase in the acidity of the ocean.[3] Even a tiny rise in acidity can negatively affect marine ecosystems and the impact has already been observed by the bleaching and death of the coral reefs.[3] Continued climate and weather change will also lead to disruption of Earth's terrestrial ecosystems and the extinction of many species.[5] Current ecosystems and habitats will become unsuitable for the residing species causing forced migration and extinction.[5] This will lead to increased stressor on surviving ecosystems, scarcity of resources, and changes in the food web.[5] If current predictions for global temperature increase are reached, the IPPC estimates that 20-30% of plant and animal species will be at risk for extinction by the end of the century.[5] Global warming changes will cause loss of food crops, shifts in regional weather patterns, and advancement of tropical diseases.[5, 6] Additionally, all direct changes will have feedback effects that further enhance emissions levels, such as volcanic eruptions which will produce sulfur dioxide and thawing of the tundra, which will release high levels of methane. [6]

A more direct impact of climate change and GHG emissions is a decrease in air quality. In 2014, 57 million Americans were reported to be living in counties that did not meet national air quality standards.[5] Not only do airborne allergens rise with rising CO_2 levels, ground ozone from smog is also rapidly increasing.[5] Ozone is known to cause respiratory problems, damage lung tissue, and lead to premature death.[5] Cardiovascular and chronic pulmonary diseases are also a

result of poor air quality and have increased in the recent years mirroring the rise in emission levels.[5]

The large increase in GHG emissions initially began with the industrial revolution in the 1750s.[4] More recently, from 1990 to 2015 there has been a 6% rise in U.S. emission levels.[4] This spike is found to align with patterns of the expanding economy and population.[4] The latest reports from Environmental Protection Agency state that in 2015 82.2% of all U.S. GHG emissions were from human activities.[4] Additionally, 65% of global GHG emissions were CO_2, specifically from fossil fuel combustion and industrial activities.[4] In fact, CO_2 emissions have now overwhelmed the natural carbon cycle sinks to the point where they are unable to decrease the concentration of atmospheric CO_2.[4] In the U.S., 35% of CO_2 emissions was attributed to electricity, followed by transportation, which includes gasoline and diesel combustion, at 32%.[4] The significant rise of CO_2 emissions makes it the largest contributor to the global warming.[1, 7] Fossil fuel combustion is not only the largest source of CO_2 emissions, but also responsible for contributing to nitrous oxides (NOx) and particulate matter (PM) emissions.[4]

1.2 Fossil Fuels and Energy Consumption

Fossil fuels are generally known to be nonrenewable sources of coal, oil, and natural gas.[3, 8] They are formed when the biomass of dead plants and microorganisms that lie under the Earth's surface are subjected to high temperature and pressure for thousands of years.[3] Burning fossil fuels is the main energy source for all electricity and transportation needs.[8] In fact, electricity and transportation were reported to be 39% and 29% of all energy consumption in 2016, respectively.[8] Energy is a necessity to sustain human life and, therefore, fossil fuel combustion is inherently linked to economic and population growth.[6] In 2016, 81% of the total energy consumption in the U.S. was sourced from fossil fuels, whereas only 10% was attributed

to renewable energy sources (Figure 2).[8] Of the 81%, petroleum oil accounted for the largest portion.[8] Global oil production alone was at 85 million barrels per day in 2010 and is predicted to increase up to 300 million barrels per day by 2100. [6]

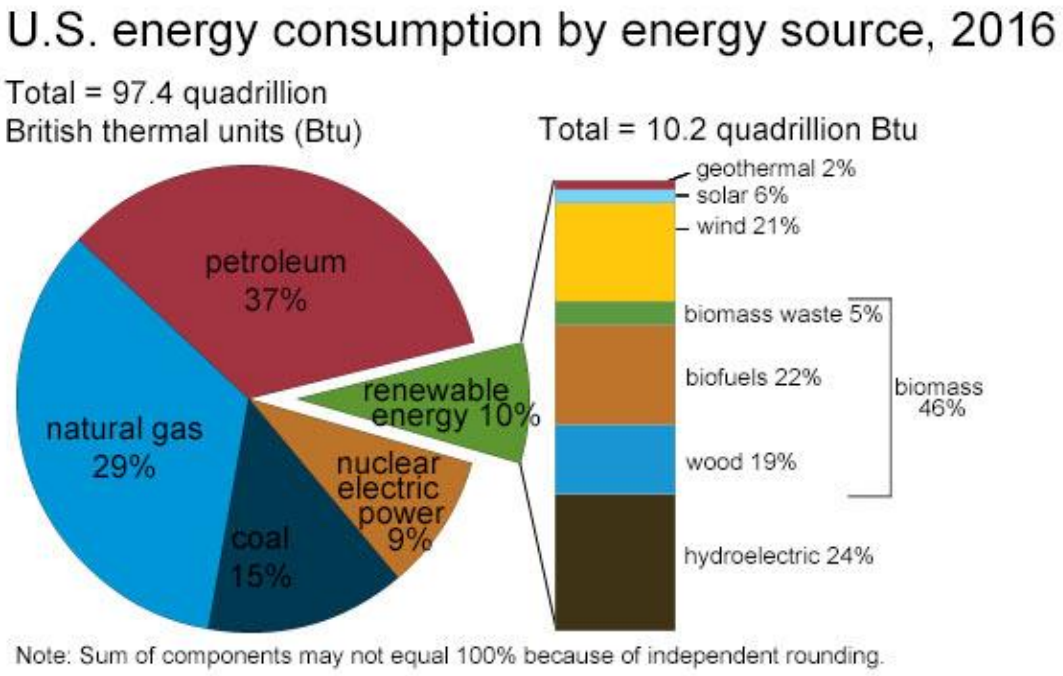

Figure 1.2 2016 U.S. Energy Consumption by Source[8]

Along with CO_2, fossil fuel combustion also contributes to the creation of PM, soot, and NOx.[4] Inhaling PM, which are extremely small particles suspended in the atmosphere, can lead to lung cancer and cardiovascular diseases.[5] NOx emission levels have increased asthma patients and has been linked to deteriorating lung function.[9, 10] Fossil fuel combustion will continue to decrease air quality and worsen the already harmful health effects. Aside from air pollution concerns, implementing viable alternatives to fossil fuels is increasing necessity because fossil fuels are rapidly diminishing.

Despite the many complex and conflicting prediction models for fossil fuel depletion, it is agreed that available fossil fuels sources are going to disappear within the near future, simply

because the rate of formation cannot keep up with the rate of extraction.[6, 11, 12] Currently, many reports are considered optimistic and overestimate fossil fuel reserves because they account for unconventional hydrocarbons, such as tar sands and gas hydrates.[6, 11, 12] Modern technology cannot process these hydrocarbons that are beyond physical limitations.[6] Many industry, national, and international governmental sources estimate that oil will end by 2050 and that the peak of availability has already occurred.[11, 12] Reserves for coal and gas are also estimated to only last 200 and 70 more years, respectively.[12] Therefore, the majority of current fuel sources are going to finish in within this century and the need for renewable energy resources is vital.

1.3 Combustion

Nearly all the energy used today is a result of combustion. On a rudimentary level, combustion is a set of reactions between an oxidant and a fuel that produces carbon dioxide, water, and heat.[13, 14] The equation below models the simplified reaction:

$$\text{Organic molecule} + O_2 \rightarrow CO_2 + H_2O + \text{Heat}\ ^{14}$$

However, since fuels are complex hydrocarbons, actual combustion reactions produce many species that further react with other combustion radicals and intermediates in the atmosphere.[15] Polycyclic aromatic hydrocarbons (PAHs), methane, and ozone are commonly formed by the secondary and tertiary reactions.[15] Even simple hydrocarbons, such as methane, have multiple reaction paths and lead to many intermediates and products.[16] Methylidyne radical (CH) is one of the most reactive radicals in the atmosphere and can greatly affect the energetics of gas-phase environments due to having fast, barrier-less reactions with unsaturated hydrocarbons.[17, 18] In this thesis, the combustion reactions of three potential biofuels with CH radical are studied. Understanding combustion reactions is essential to produce more efficient and cleaner engine designs as well as fuels in the future.

The automobile industry has already began developing alternatives such as electric, fuel cell, and hybrid engines in newer model cars.[19] One of the new and promising engine designs is homogeneous charge compression ignition (HCCI) engine. HCCI engines can utilize current spark ignition (SI) and compression ignition (CI) engines, while maintaining high engine efficiency and low emission levels of NOx, soot, and PM. [19] In Figure 3, the differences between SI, CI, and HCCI engines are illustrated. [19] SI engines use spark plugs with a flame front that lies along the combustion chamber to initiate combustion, while a CI engines uses fuel injects to inject diesel into a compressed hot air region where combustion takes place. [19] HCCI engines relies completely on chemical kinetics and allows for combustion to initiate in multiple locations when the necessary activation energy of the fuel mixture has been reached. [19] The combustion process is much faster that CI or SI engines and improves engine efficiency by up to 37%.[19] However, the biggest advantages of HCCI engines is its fuel versatility and ease of implementation through small modifications to any type of current engine configuration already in use. [19] The major disadvantages of the HCCI are engine knocking, low operating load range, and high levels of unburned hydrocarbons and carbon monoxide. [19] Ongoing research and development is working to reduce and eliminate these problems. [19]

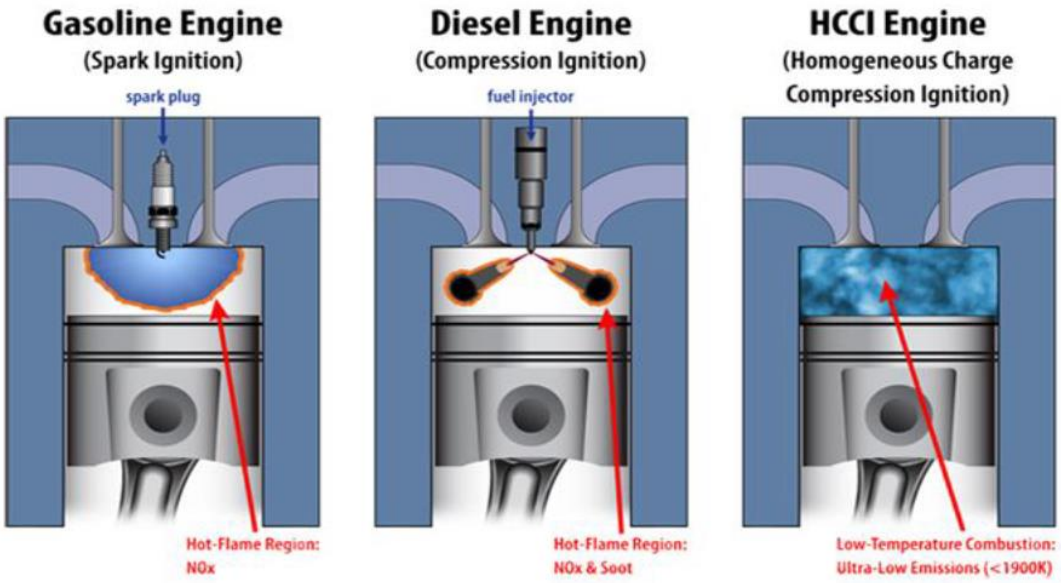

Figure 1.3 Differences among SI, CI, and HCCI Engine Configurations[19]

1.4 Biofuels and Fuel Additives

Global energy consumption is not going to decrease and, therefore, the move to using renewable energy sources is imminent. As previously mentioned, transportation accounts for 32% of GHG emissions; therefore, it is necessary to minimize the emission levels produced by fuel combustion to create a positive change and reduce global emissions for the future. An ideal alternative would be biomass-derived fuels that could be mass produced by a process that is able to recycle and reduce atmospheric CO_2. Photosynthetic production to yield simple sugars and eventually produce carbon-based fuels, such as ethanol and 2,5-dimethylfuran, has already been proven possible by several studies.[20-23]

Carbon-based fuels are one of the most promising immediate alternative biofuels because they can be utilized in current combustion engines with little to no modifications.[20, 24] Many of these fuels, including furan derivatives studied in this thesis, are second generation biofuels meaning that are produced from unconsumable biomass.[21-23] Therefore, mass production would

not compete with food production for humans. Second generation biofuels are also nontoxic and biodegradable.[25] Combustion and emissions studies have found that many biofuels have lower PAH, CO_2, NOx and PM emissions that current gasoline and diesel fuels.[26, 27] Several engine studies have also confirmed these fuels to have higher energy density, octane ratings, and knock resistance.[26, 27]

Fuel additives can also be easily implemented to help decrease emissions and reduce global warming. The main advantage presented by fuel additives is the reduction in engine knocking, which results in emission of toxic intermediates and radicals from incomplete fuel combustion.[25] For example, the addition of aromatic hydrocarbon compounds, such as 2-methylfuran, to gasoline increases energy density and octane rating, which aids in achieving complete combustion. [8, 19] In order to reduce air pollution and negative health impacts in the future, the study of the reactivity of biofuels and fuel additives is necessary.

1.5 Overview of Thesis

This thesis investigates the reactions of methylidene radical (CH) with three furan compounds: furan, 2-methylfuran, and 2,5-dimethlyfuran. The furan compounds are all possible biofuels and fuel additives and their combustion reactions are of high interest for their possible future implementation. As previously mentioned, reactions with CH radical are also of interest due to the fast and exothermic nature of their reactivity. Detailed reaction mechanisms of CH with furan and 2-methylfuran are presented in Chapter 4. Continued in Chapter 5, the reaction of 2,5-dimethlyfuran with CH and CD radicals are also explained. The additional reaction with CD radicals allows for further confirmation of the proposed mechanism. All three reactions shared a CH addition entrance channel to the pi bond systems, as well as patterns of cyclic and acyclic products. The combustion experiments were carried out at the Advanced Light Source (ALS) of

the Lawrence Berkeley National Laboratory using a multiplex time- and energy-resolved photoionization mass spectrometer. The experimental apparatus is described in detail in Chapter 2.

Studying unimolecular dissociation reactions are also important to understanding combustion behavior of given compounds. Chapter 6 presents the investigation of the photodissociation of valeric acid. Along with dissociation products and experimental appearance energies, accurate thermochemistry for the reactions were also calculated. Experiments were conducted using the double imaging photoelectron photoion coincidence spectroscopy (i^2PEPICO) of the VUV beamline at the Swiss Light Source in the Paul Scherrer Institute.

1.6 References

1. U. S. E. P. Agency, Climate Change: Basic Information, https://19january2017snapshot.epa.gov/climatechange/climate-change-basic-information_.html).
2. N. P. Service, What is Climate Change?, https://www.nps.gov/goga/learn/nature/climate-change-causes.htm).
3. N. O. a. A. Administration, The Earth's Atmosphere, https://www.esrl.noaa.gov/gmd/outreach/carbon_toolkit/basics.html).
4. U. S. E. P. Agency, Overview of Greenhouse Gases, https://www.epa.gov/ghgemissions/overview-greenhouse-gases).
5. U. S. E. P. Agency, Climate Changes Impacts on Human Health).
6. M. Höök and X. Tang, *Energy Policy*, 2013, **52**, 797-809.
7. N. A. a. S. Administration, Long-Term Warming Trend Continued in 2017: NASA, NOAA, https://www.giss.nasa.gov/research/news/20180118/).
8. U. S. E. I. Administration, What Is Energy? Explained, https://www.eia.gov/energyexplained/index.php?page=about_home).
9. U. S. E. P. Agency, *Motor Vehicle-Related Air Toxics Study*, NEPIS, 1993.
10. T. O. Yoshinori Murakami, Kohtaro Hashimoto, and Yoshio Nosaka, *The Journal of Chemical Physics A*, 2009, **113**, 10652-10666.
11. P. Droege, *Bulletin of Science, Technology & Society*, 2002, **22**, 87-99.
12. S. Shafiee and E. Topal, *Energy Policy*, 2009, **37**, 181-189.
13. N. De Leon, Combustion Reactions, http://www.iun.edu/~cpanhd/C101webnotes/chemical%20reactions/combustion.html).

14. C. E. Ophardt, Combustion of Fossil Fuels, http://chemistry.elmhurst.edu/vchembook/511natgascombust.html).

15. J. S. Gaffney and N. A. Marley, *Atmospheric Environment*, 2009, **43**, 23-36.

16. T. L. Nguyen, J. Peeters and L. Vereecken, *The Journal of Physical Chemistry A*, 2007, **111**, 3836-3849.

17. F. Goulay, A. J. Trevitt, G. Meloni, T. M. Selby, D. L. Osborn, C. A. Taatjes, L. Vereecken and S. R. Leone, *J. Am. Chem. Soc.*, 2009, **131**, 993-1005.

18. A. J. Trevitt, M. B. Prendergast, F. Goulay, J. D. Savee, D. L. Osborn, C. A. Taatjes and S. R. Leone, *J. Phys. Chem. A*, 2013, **117**, 6450-6457.

19. A. A. Hairuddin, A. Wandel and T. F. Yusaf, *AN INTRODUCTION TO A HOMOGENEOUS CHARGE COMPRESSION IGNITION ENGINE*, 2014.

20. M. Mascal and E. B. Nikitin, *Angew. Chem., Int. Ed.*, 2008, **47**, 7924-7926.

21. G. D. Tian, R. ; Xu, H., *A New Biofuel Candidate, Biofuel Production - Recent Developments and Prospects*, InTech, 2011.

22. Y. Román-Leshkov, C. J. Barrett, Z. Y. Liu and J. A. Dumesic, *Nature*, 2007, **447**, 982.

23. H. Zhao, J. E. Holladay, H. Brown and Z. C. Zhang, *Science*, 2007, **316**, 1597.

24. E. Christensen, J. Yanowitz, M. Ratcliff and R. L. McCormick, *Energy Fuels*, 2011, **25**, 4723-4733.

25. R. F. Colwell, *Benzene in Gasoline Regulations & Remedies*, PROCESS Engineering Associates.

26. S. Gouli, E. Lois and S. Stournas, *Energy Fuels*, 1998, **12**, 918-924.

27. M. A. Eldeeb and B. Akih-Kumgeh, *Energy Fuels*, 2014, **28**, 6618-6626.

Chapter 2 Experimental Methods

The photoionization reactions of furan, 2-methlyfuran, and 2,5-dimethyfuran with methylidyne radicals (CH) presented in this work were conducted at the Advanced Light Source (ALS) located in the Lawrence Berkeley National Laboratory (LNBL). Synchrotron radiation from the ALS is coupled with a multiplexed time- and energy-resolved mass spectrometer (PIMS) at the Chemical Dynamics Beamline 9.0.2 to simulate the combustion reactions of the potential biofuels. The unimolecular dissociations of valeric was completed at the Swiss Light Source (SLS) of the Paul Scherrer Institute (PSI). The dissociation reactions were carried out using the VUV beamline and double imaging photoelectron photoion coincidence spectroscopy (i^2PEPICO). Details about the experimental apparatus, components, and instrumentation of the ALS and SLS experiments will be discussed in this chapter.

2.1 The Advanced Light Source Experimental Methods

2.1.1 Sample Preparation

All three furanic compounds used in the ALS studies presented in this work were prepared using a freeze-pump-thaw purification method. Each compound was obtained from Sigma-Aldrich commercially and stored as a liquid at room temperature. The sample preparation apparatus consists of a bubbler, vacuum pump, and gas cylinder connected by steal lines regulated by valves. A small amount of the compound is transferred to the bubbler and immerged in liquid nitrogen until frozen. The vacuum is then opened to pull out any dissolved gaseous impurities that were in the liquid sample. After the valve to the vacuum is closed, the sample is allowed to thaw and this process is repeated at least two more times to ensure the sample has been purified. The valves are opened to allow the vaporized sample compound to flow into the gas cylinder until the pressure has stabilized. Helium is then flowed into the gas cylinder until

the vaporized sample reaches a molar fraction of about 1%. The total pressure is typically within 2000 – 2500 torr. This addition is essential as the PIMS experiments require a constant flow from the gas cylinder to last for several hours. Before use the gas cylinders are flushed with helium and pumped for several hours to clean and remove any remaining gas molecules from previous fillings. Two Baratron digital pressure readers each with MKS pressure transducers are used to convert pressure into an analog signal output. One of the readers is used to measure high pressures of up to 10,000 torr and the other is used to measure low pressures of 1-10 torr. Readings from the digital pressure readers for the vaporized sample and the total pressure within the gas cylinder must also be recorded. Now, the sample preparation is complete and ready to use in the PIMS apparatus described in detail later in this chapter.

2.1.2 The Advanced Light Source Components

The purpose of the ALS is to produce a very bright and focused light through the acceleration of electrons. The light from the ALS is an X-ray that is highly concentrated in a very small region and this brightness allows for very specific targets to be studied.[1-2] Also, the energy of the light allows the ALS X-rays to interact with electrons of smaller compounds, such as simple hydrocarbons.[2] The ALS at the LBNL is a third-generation synchrotron that is composed of an electron source, linear accelerator (linac), booster ring, and storage ring that eventually leads to multiple experiment end stations through different beamlines. (Figure 2.1)[3]

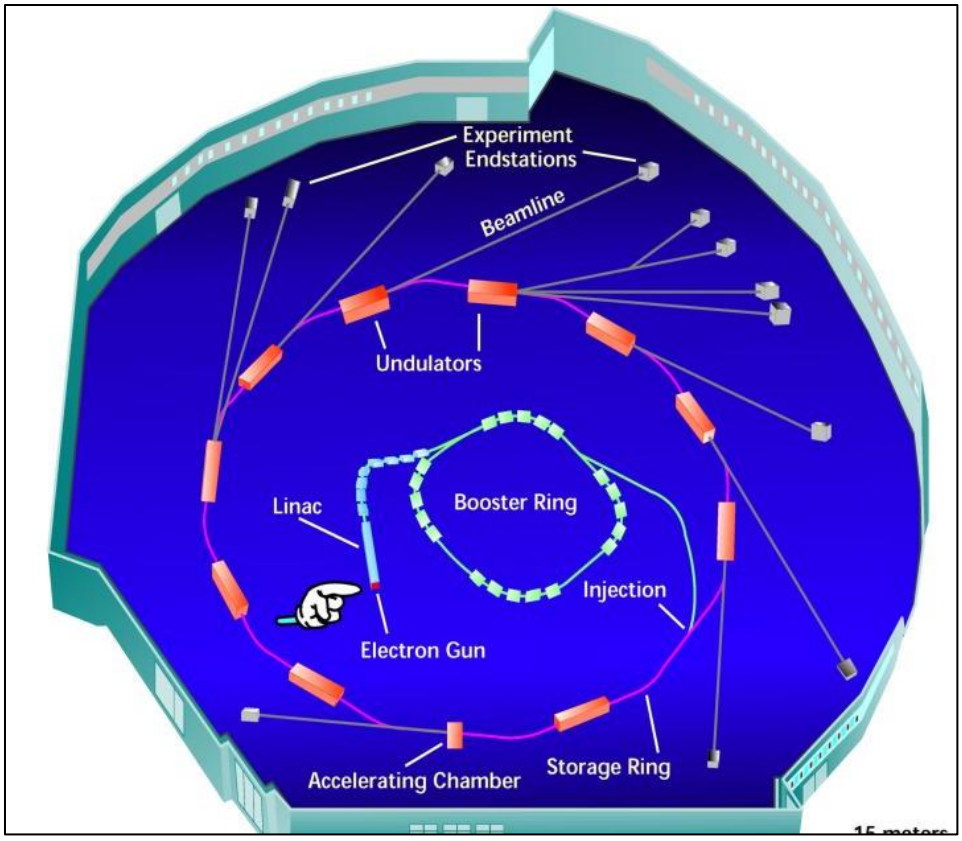

Figure 2.1 Basic layout of the Advanced Light Source at the Lawrence National Berkeley Laboratory[3]

Electrons are first produced by an electron gun and initially accelerated to nearly the speed of light with 50 MeV by the buncher and linac.[3] The sections are illustrated in more detail in Figure 2.2.[2] The electron gun is made up of a cathode, copper screen or gate, and an anode.[3] The cathode is a piece of barium aluminate that is heated to release electrons from its surface.[2] The freed electrons then move towards the surface of the copper gate.[2] A voltage is applied to the gate every 500 millionth of a second to create a pulsing anode, which causes the electrons to move towards the gate in bunches. [2] Beyond the gate, there is a stronger anode that pulls the electrons through the gate and into the buncher section of the linac.[2] The buncher section is used to accelerate and increase the density of the electron bunches.[2] Each bunch contains approximately 1.5 x 10^{11} electrons.[3] Microwave radiation from the klystron of the radio

frequency (RF) system, which will be discussed later in this section, is used to accelerate and move the electron bunches in a wave pattern down to the actual linac section.[2] The electrons leave the buncher at about 60% the speed of light and with 120 keV of kinetic energy.[3] The linac section continues the wave pattern and receives additional microwaves from the RF system to speed up and increase the density of the electron bunches even more.[2] Electromagnets that lie along the length of the linac are used to counteract the electron repulsion affects and maintain the density of the electron bunches.[2] At the end of the entire electron gun and linac section, the electrons are travelling nearly at the speed of light with 50 MeV of kinetic energy.[2-3] A vacuum is also created and maintained throughout the entire apparatus to avoid any unwanted collisions between the electrons and other molecules.[3]

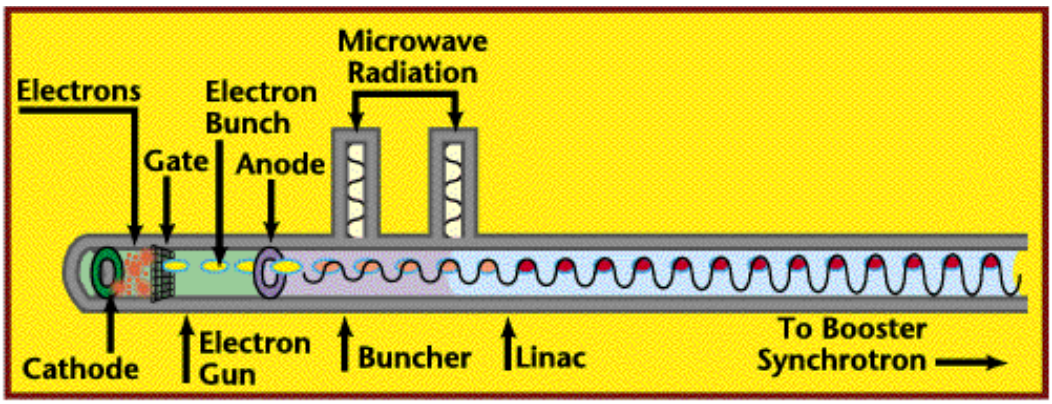

Figure 2.2 Detailed illustration of the electron gun and linac components of the ALS[2]

From the linac, the high-density electron bunches enter the booster ring as an electron beam and circle around until they reach 99.999994% the speed of light with 1.5 GeV of kinetic energy.[2-3] A section of the ring is an accelerating chamber that transfers energy from the UHF transmitter to the electrons every time they circle the ring.[3] This energy counter acts and surpasses the energy electrons lose by giving off radiation.[3] The electrons circle the booster ring about 1.3 million times, which is 98,000 km, in less than a second.[2-3] Quadrupole and dipole magnets throughout the booster ring are used to focus and turn the electron beam, respectively.[3]

The electron beam leaves the booster ring and moves into the storage ring through an injection system.[2-3] The purpose of the storage ring is to hold and maintain the electron beam's high energy, which is 1.5 – 1.9 billion eV.[1-2] As the electrons circle, photons are emitted in a fan-like beam and led to the individual beamlines.[2] Like the booster ring, one of the sections has an RF cavity that transfers energy to the electrons each time they pass around the ring to recuperate any energy the electrons may lose as they turn.[3] The storage ring is made of 12 arc-shaped and 12 straight sections, which are 10 and 6 meters long, respectively.[2] They are interchanging and connect to form a circle with a diameter of 63 meters.[2-3] Each arc-shaped section has three precision electromagnets laid out in a "triple bend achromat" arrangement that focus and bend the electron beam around the ring.[2-3] The straight sections are lined with insertion devices called undulators and wigglers.[2] The devices serve to wiggle the electrons and form a beam of light from the emitted photons, which is directed by beam ports to individual beamlines.[2] The undulators and wigglers contain many magnets oriented in an alternating format that move the electrons in a wave pattern.[3] The distance between the opposing magnets determines the energy of the radiation and can be adjusted to best suit the experimental needs. [3] The undulators are 14 feet long and contain over 100 magnetic poles.[2-3] The wigglers function in a similar way, but with fewer magnets and produce synchrotron radiation with a broader spectrum than the radiation produced from the undulators. [3]

As previously mentioned, the RF system is used throughout the ALS sections to provide energy to the electrons. The RF system is made up of the klystrons, wave guides, and RF cavities.[2] A klystron is a microwave amplifier that moves the waves down coaxial cables known as wave guides to the different RF cavities throughout the ALS.[2] The RV cavities then transfer the microwave radiation, with a wavelength of 0.6 meters, directly to the electrons.[2] The RF

energy creates a wave pattern and the acceleration increases because there is a section of the wave that electrons prefer to be as shown in Figure 2.3 below.[2-3] This causes the electrons to slow down or speed up based on their location relative to this section.[3]

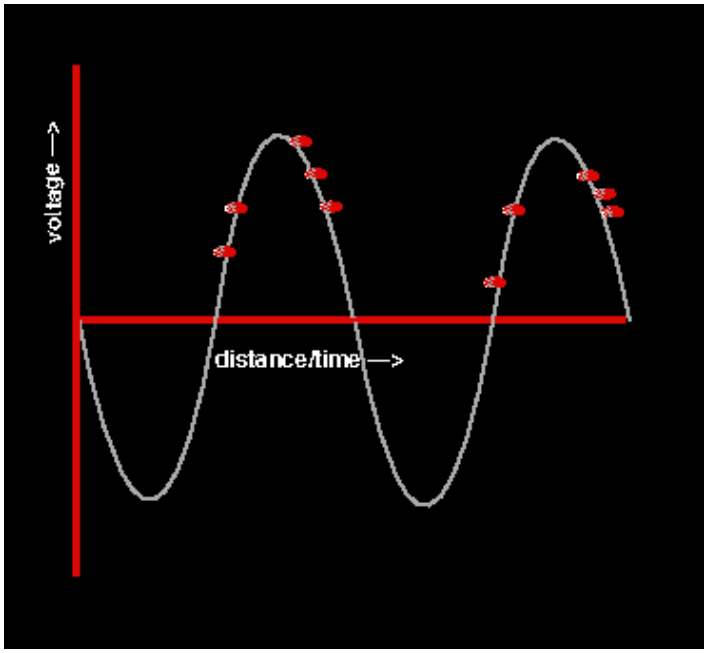

Figure 2.3 Illustration of the acceleration of electron bunches (red disks) by microwave radiation produced from the radiofrequency system of the ALS[2]

2.1.3 Chemical Dynamics Beam Line

Once the light, or synchrotron radiation, is directed to the Chemical Dynamics beam line, it is narrowed and filtered to a 2.5% bandwidth with a 7.2 – 25 eV range before entering the ionization chamber of the PIMS at the experimental end station.[4-5] The pathway from the storage ring to the ionization chamber is completely windowless.[6] The light is refined first by an absorption cell filled with Ar or Kr gas then by an Eagle monochromator.[6] When the light reaches the absorption cell, only harmonic radiation that is lower than the ionization energy of either Ar or Kr can pass through.[5] Continuing to the Eagle monochromator, the synchrotron radiation bandwidth is further narrowed to 10 – 50 meV range before exiting through slits to the

PIMS.[5] The Eagle monochromator narrows the bandwidth of the light beam's photon energies according to Bragg's Law.[6]

$$n\lambda = 2\,d\sin\theta, \text{ where n is an integer} \quad \text{(Equation 2.1)}$$

Bragg's law states that since the incident beam hits the reflecting plane of the monochromator at a specific angle (θ), only a specific wavelength (λ) can be reflected from the original beam. [3, 6] Therefore, different wavelengths can be selected by adjusting the angles of reflecting plane and the incident beam.[3, 6] In the experiments presented here, the atomic resonances of Xe, from 12.545 to 12.575 eV, are used to calibrate the bandwidth and photon energies.[5] The synchrotron radiation is considered "quasi-continuous" because the detection bandwidth is significantly smaller than the repetition rate that the light is pulsed at.[5] The continuous and rapidly tunable radiation source allows for reactions with continuous probing to be conducted, which will be further discussed later in this chapter.

2.1.4 Multiplexed Photoionization Mass Spectrometer Apparatus

The experimental apparatus located at the end of the Chemical Dynamics beamline consists of an excimer laser, ionization chamber, time-of-flight mass spectrometer (TOF-MS), and a microchannel plates (MCP) detector. A vacuum system is used to maintain very low pressure throughout the entire apparatus.[3] The basic schematic of the experimental set-up is shown in Figure 2.4.

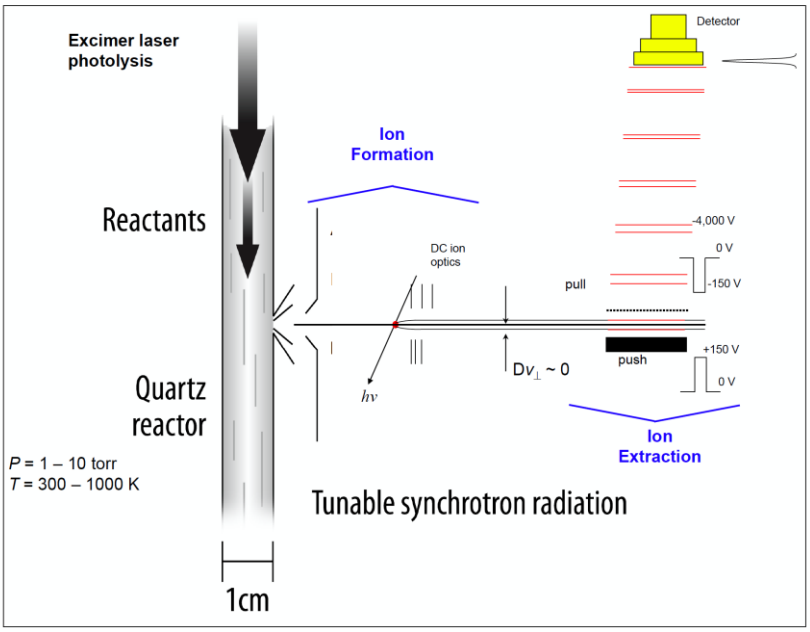

Figure 2.4 Schematic of the multiplexed chemical kinetics orthogonal mass spectrometer

From previously prepared gas mixtures described in Sec. 2.2.1, the sample and precursor gases are flowed into the quartz reactor tube by calibrated mass flow controllers.[5] The gases then leave the reactor tube through a 650 μm pinhole to enter the source chamber as an effusive molecular beam.[5] An excimer laser is used to photolyze the gaseous precursor to produce free radicals that will react with the sample gas.[5] The resulting reaction mixture, which could consist of products and intermediates, is side-sampled and skimmed by a 0.15 cm skimmer before entering the ionization chamber as a molecular beam.[5] The synchrotron radiation intersects the molecular beam perpendicularly.[5] Any reaction species will be ionized with higher photon energy than their ionization energy and continue through the experimental apparatus to the TOF-MS.[5]

The quartz reactor tube is a slow-flow reactor and is 62 cm long with a 1.27 cm outer diameter and 1.05 cm inner diameter.[5] An 18 μm Nichrome tape is wrapped around the reactor tube to prevent short circuits, maintain temperature uniformity, and minimize radiating heat transfer into the source chamber.[5] The tape itself is also covered with a square-weave, ZYW-15

cloth, and gold-plated copper sheath.[5] A thermocouple monitors the temperature of the reactor tube and provides measurements to the closed-loop feedback circuit to control the temperature.[5] The side-sampling of reactor is essential to capturing time dependent concentration changes caused by a chemical reaction because the position of the species at sampling does not affect their concentrations.[5] A capacitive manometer and closed-loop feedback valves, which connect to the Roots pump, are used to measure the pressure within the reactor tube.[5] The Roots pump is used to remove gases from the reactor tube. Three turbomolecular pumps with speeds of 3200 L/s, 1600 L/s, and 600 L/s are used throughout the experimental apparatus to vacuum the source chamber, ionization chamber, and detector, respectively.[5] The vacuum pumps are described in further detail later in this chapter. All the ALS reactions presented in this work maintained the pressure and temperature of the reactor tube at 4 Torr and 298 K.

2.1.4.1 The Excimer Laser

As previously mentioned, the purpose of the excimer laser is to photolyze a selected precursor to produce free radicals that will react with the sample gas molecules.

A laser functions as a result of population inversion and stimulated emission. Population inversion is the redistribution of atomic or molecular energy levels within a system.[7] As shown in Figure 2.5, when a system is at thermal equilibrium, or "normal distribution", there are a more atoms at lower energy levels than at higher energy levels.[7-8] Population inversion occurs when there is a disturbance in system's equilibrium, such as an input of energy, that causes more atoms or molecules to be at higher energy levels instead of lower levels.[7-8] Eventually, the excited atoms in the higher energy levels will return to the lower levels and emit energy as photons in the process.[7-8]

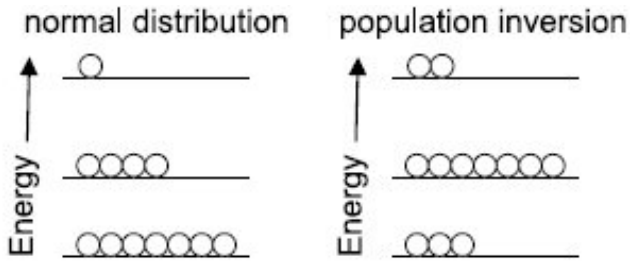

Figure 2.5 Energy level diagrams for equilibrium and population inversion[7]

Stimulated emission of radiation is used to ensure that the emitted photons are all the same wavelength.[7] The emission of photons from population inversion are stimulated by an incoming photon from outside the system, which already has the desired wavelength.[7] The incoming photon is a source of radiation that then becomes amplified because the emitted photons from the system move in the same direction as the incoming photon.[7] This event results in what is known as light amplification by stimulated emission of radiation (LASER).

A xenon fluoride (XeF) excimer laser is used to produce the photons at 248 nm that are necessary for the photolysis of bromoform. To prompt the population inversion that is needed to produce a laser, xenon and fluorine gas are flowed into the gas chamber of the laser apparatus. Energy discharge will produce a spark that will then excite the xenon atoms and the excited xenon will react with molecular fluorine as shown below.

$$Xe^* + F_2 \rightarrow (XeF)^* + F$$

The bound excited (XeF)* will then drop to the ground state to form the unbound XeF while emitting photons at 248 nm. The (XeF)* compound is known as a "excimer", or excited dimer, that only exists in the excited state.[9] The laser in this experimental apparatus is pulsed at 4 Hz and 160 mJ per pulse.

In the ALS experiments presented here, bromoform, $CHBr_3$, is photolyzed to produce methylidyne radicals, CH ($X^2\prod$), with the photons at 248 nm emitted from the XeF excimer

laser. The bromoform molecules are in a gas mixture of 1% bromoform/helium and prepared as described in Sec. 2.1.1. As shown below, CH ($X^2\prod$) radicals are only produced from multi-step dissociation pathways of bromoform, with $CHBr_2$ and CHBr radicals as intermediates.[10-11]

$$CHBr_3 \xrightarrow{hv=248\ nm} CHBr_2 + Br \xrightarrow{hv=248\ nm} CH + Br_2$$

$$CHBr_3 \xrightarrow{hv=248\ nm} CHBr + Br_2 \xrightarrow{hv=248\ nm} CH + Br$$

Due to the multiple photodissociation products and pathways, quantification of the dissociation species is not feasible.[10-11] Chapter 4 and 5 describes these pathways and quantification issues further.

2.1.4.2 Time-of-Flight Mass Spectrometer

The multiplexed photoionization mass spectrometer in this work uses a Wiley-McLaren TOF-MS design, which allows for continuous and simultaneous detection of ionic species at multiple m/z ratios.[12] The Wiley-McLaren design is allows for high resolution to be maintained using only electric fields.[12] The reaction species that ionize after intersecting with the synchrotron radiation beam are now cations and directed to the TOF analyzer by a series of DC electric fields.[13] The electric fields serve to focus and align the cations to the end of the flight tube of the TOF-MS.[13] Then, the cations are guided to the detector by opposing positive ("repeller") and negative electric fields ("puller") of 150 V and -150 V, respectively.[13] The accelerated ions are separated as they travel down the flight tube based on their different velocities. The velocity of an ion is solely reflective of its specific m/z ratio because the same electric field (U) will be applied to all ions resulting in the same initial kinetic energy (KE) for all ions.[13] Therefore, these two factors are constants and m/z ratio is the only variable. The equation below shows this relationship between the velocity (v) and mass (m):

$$\nu = \sqrt{\frac{2ezU}{m}} = \sqrt{\frac{2KE}{m}} \quad \text{(Equation 2.2)}$$

where z is the integer of the electron charge and e is the electron charge. Therefore, ions with a lighter mass will have a faster velocity whereas heavier ions will be slower and reach the end of the flight tube last. Finally, the cations reach their terminus location at the MCP detector.

2.1.4.3 Microchannel Plates Detector

To collect data from the TOF-MS, the MCP detector amplifies the signal of the detected ions based on their arrival times to the detector plate. A single MCP plate is made up of channel electron multiplier (CEM) tubes that are placed very close together to increase the possibility of ion collisions.[13] Since the CEM tubes are semiconductors, ion collisions with the MCP plate can form secondary electrons that are then accelerated by an electric field.[13]

In our experimental apparatus, 2 MCP plates are alternatingly stacked in a "v-stack" or chevron plate arrangement for signal amplification from plate to plate.[13] The "v-stack" reaches a capacity and forms 10^7 electrons for each incoming cation that collides with the MCPs.[5] Figure 2.6 depicts the chevron plate arrangement in further detail. Raw data is outputted as a 3-D block and details about data processing are discussed in Chapter 3.

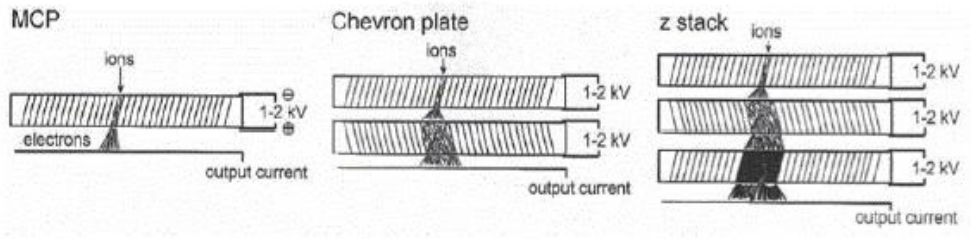

Figure 2.6 From left to right, diagrams of the ion signal amplification of a single MCP plate, chevron plate arrangement of 2 stacked MCPs, and a z-stack arrangement of 3 stacked MCPs.

2.1.4.4 Vacuum Pumps

As previously mentioned, several vacuum pumps are used throughout the experimental apparatus to eliminate contamination from unwanted molecules within the system. The three types of pumps utilized are turbomolecular, Roots, and scroll pumps.

Three turbomolecular pumps are individually connected to the source chamber, ionization chamber, and the detector. A turbomolecular pump is made up of circular blades layered on top of one another in "stages".[14] Each stage has a moving blade, known as a rotor or turbine blade, and a stationary blade, or stator.[14] A simple illustration and cross section of a roots pump is shown in Figure 2.7 below. As gas molecules enter the vacuum, the gas collides with the moving rotors and momentum is given to the gas molecules.[14-15] The molecules then move towards the stator, which leads them to the pair of blades in the next stage.[14-15] The gas molecules are compressed and increase in pressure as they move down the stages in the vacuum pump until they are removed by a backing pump.[14-15]

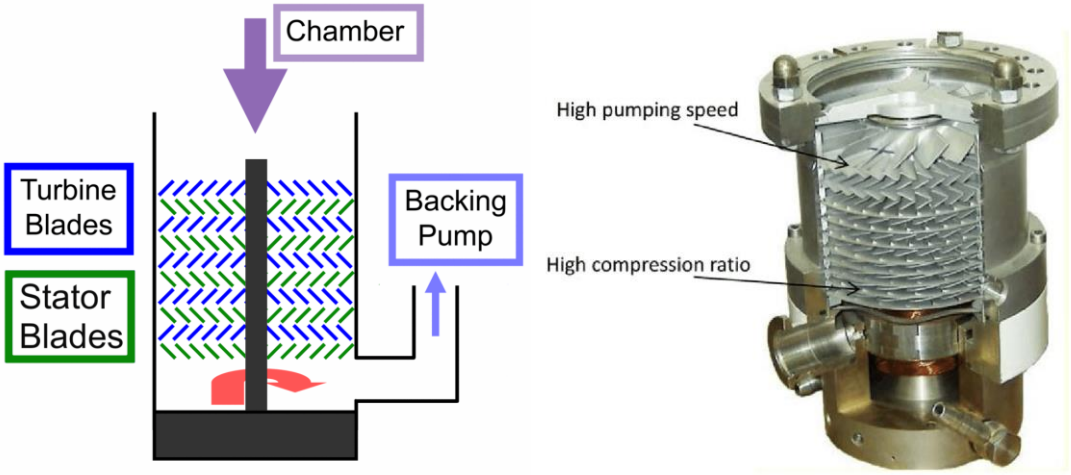

Figure 2.7 Diagram and cross section of a turbomolecular pump.

The Roots and scroll pump are coupled to the highest speed (3200 L/s) turbomolecular pump, which connects to the source chamber at the bottom of the quartz reactor tube. The scroll

pump serves specifically as the backing pump and removes the high-pressure gas from the turbomolecular pump. Within the scroll pump, there is one rotating and one stationary scroll that move gas molecules to the center of the pump in order to compress the gas and increase the pressure.[16] A schematic of the scroll pump's function is shown in Figure 2.8, where the black line represents the stationary scroll and the red line represents the rotating scroll. As the rotating scroll moves, the area between the two scrolls changes. Therefore, gas molecules within the pump become trapped and pushed into the vacant space until they reach the outlet in the center of the pump.[15-16] The scroll pump maintains a pressure of 10^{-2} torr and a pumping speed of 6 – 13 L/s.[17]

Figure 2.8 Schematic of gas moving through the scroll pump.[16]

The Roots pump consists of two rotors that spin in opposite directions without touching in order to move gas molecules to a higher pressure. A basic diagram of the pump is detailed in Figure 2.9. The two rotors are synchronized and spin at a rotation speed of 1000- 3000 rpm.[17] Gas molecules enter at the inlet of the pump with a low pressure and are pushed and carried towards the outlet where the pressure increases as the gas exits the pump.[14] The Roots pump has a pressure range of 10 – 10^3 mbar and pumping speed range up to 8333 L/s.[17]

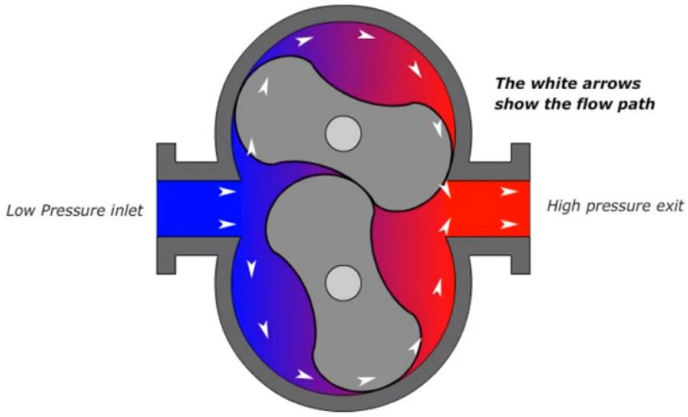

Figure 2.9 A general diagram of a Roots pump.[18]

2.2 The Swiss Light Source Experimental Methods

2.2.1 The Swiss Light Source

The SLS instrumentation is very similar to that of the ALS and is also used to produce synchrotron electromagnetic radiation with very high brightness from the acceleration of electrons to nearly the speed of light. The light spectrum can range from infrared to hard x-rays and the specific wavelength depends on the energy of the electrons.[19-20] At the PSI, the SLS is a third-generation synchrotron made up of a linac, booster, and storage ring that generate a photon beam with an energy of 2.4 GeV to use in photoionization and photodissociation experiments.[19] Figure 2.10 depicts a general layout of the SLS.

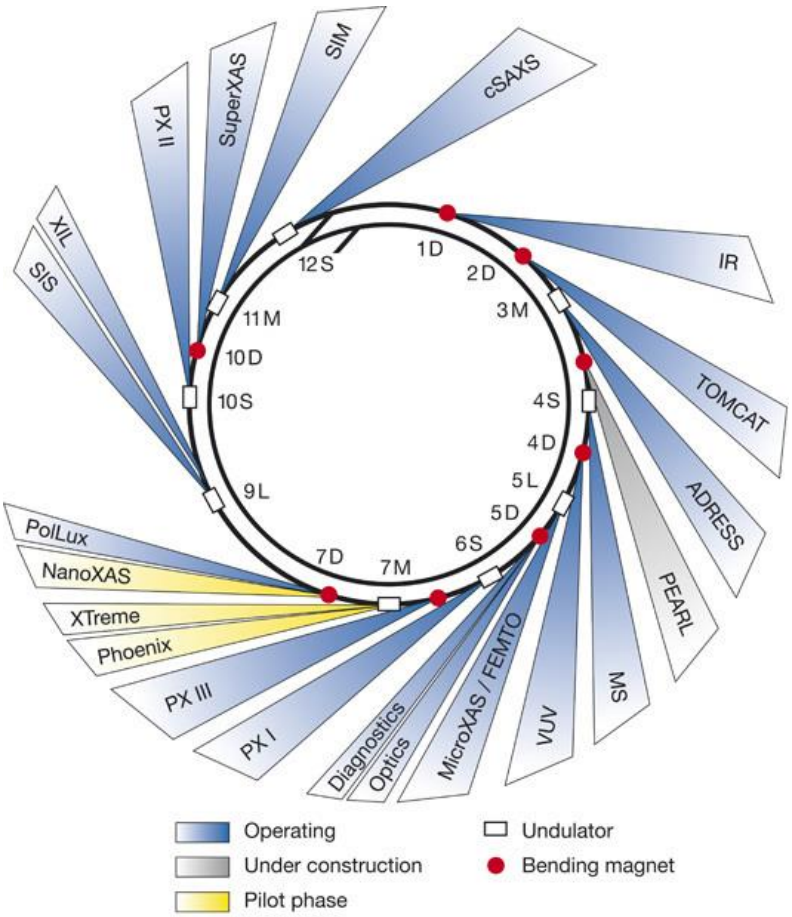

Figure 2.10. Basic layout of the Swiss Light Source at the Paul Scherrer Institute. Inner ring is the booster and the outer ring is the storage ring.[19]

Like the ALS, an electron gun apparatus is used to generate electrons from a heated cathode surface and direct them to an anode using an applied voltage of 90 kV from an RF system.[19] The linac is made up of two 5.2 m long accelerating sections that increase the electrons energy to 100 MeV.[19] Electrons then travel from the linac through a 16 m transport beam and are injected into the booster ring by kicker magnets,[19] where the electrons are further accelerated until their energy reaches 2.4 GeV.[19] The energy is provided by the RF system, just like in the ALS apparatus.[19] The booster ring has a 270 m circumference and is lined with 237 magnets that produce a magnetic field that is adjusted as the electrons increase in energy.[19] A 20 m transport beam then directs the electrons to the storage ring[19] in which the electrons are "top-up" injected.

This means that the electrons are injected intermittently, about every 1-2 minutes, in order to maintain their high intensity constant.[19, 21] The high energy electrons circle around the storage ring for hours and emit electromagnetic radiation, or light.[19] The light is directed to specific experimental end stations by beamlines that utilize the same insertion devices as the ALS.[19] Mirrors and monochromators in the beamlines serve to filter and select the desired wavelength of the SLS light.[21] Ultrahigh vacuums throughout the entire SLS apparatus and beamlines are used to prevent loss of electrons from unwanted collisions with molecules in the air.[19-20]

2.2.2 VUV Beamline

The VUV beamline uses magnets, mirrors, and monochromators to focus and refine the electromagnetic radiation to a monochromatic light with 104 resolving power and a 5-30 eV range that will be used in experimentation.[20, 22] The light emitted from the electrons is linearly polarized on the plane of the storage ring and elliptically polarized above and below that plane.[21-23] The vertical acceptance angle has to be wide in order to accept VUV radiation since it extends beyond the plane. However, this wider range allows for undesirable X-rays and high harmonics to enter the beamline as well, which will need to be filtered out before the light can be used at the experimental end station. The light passes through an X-ray blocker made up of a water-cooled copper tube that removes X-rays and a large amount of heat.[21-22] Next, the light reaches the first mirror that removes photon energies higher than 150 eV and continues to the monochromator plane grating.[21-22] The monochromator along with a second mirror refines the light to the desired resolving power and photon energy range.[21-22] Similar to the monochromator of the ALS, the angle of the planes in the monochromators allow the VUV radiation to be tunable.[21-22] The final third mirror directs the light to the experimental end station apparatus.[21-22] Before entering the ionization chamber of the PEPICO instrument, the light passes through a specialized gas filter.

The gas filter is like the absorption cell of the Chemical Dynamics Beamline in that it uses an argon and neon gas mixture to remove any higher photon energies than the ionization energies of these two gases. [21-22]

2.2.3 i^{2}PEPICO Experimental Apparatus and Electron Velocity Imaging

The SLS experiments presented in this research were conducted using double imaging photoelectron photoion coincidence (i^{2}PEPICO) in the symmetric set-up that allows for both photoelectrons and photoions to be imaged. (Figure 2.11)

Once the light passes through the specialized gas filter, it enters the experimental chamber and orthogonally intersects the molecular beam of the sample molecule. To produce the molecular beam, a liquid sample is placed in a glass vial and exposed to a high vacuum.[24] The gas in the headspace is drawn into the experimental chamber through a simple nozzle technique designed by Buckland et al.[24] The nozzle is very compact, and the opening has a diameter of 10 - 100 μm.[24] The molecular beam is refined and narrowed by the 1 mm slit of an in-house designed skimmer and enters the 2 mm by 2 mm ionization region, shown as the purple oval in Figure 2.11, of the experimental chamber.[20, 25] Like the ALS, ionization will occur if the energy of the VUV light is greater than the ionization energy of the sample molecule. The molecular beam is considered continuous throughout the experiment and can be pulsed.[22] The pressure in the experimental chamber is maintained through nine differentially pumped sections.[22] Most reactions are carried out at 10^{-6} mbar.[22] A 500 L/s turbomolecular pump and a 1500 L/s cryogenic pump are used to clear out the experiment chamber.[22] The source chamber is kept at a pressure of 5 x 10^{-7} mbar and pumped out by a 1500 L/s turbomolecular pump and a 5000 L/s cryogenic pump.[20, 22]

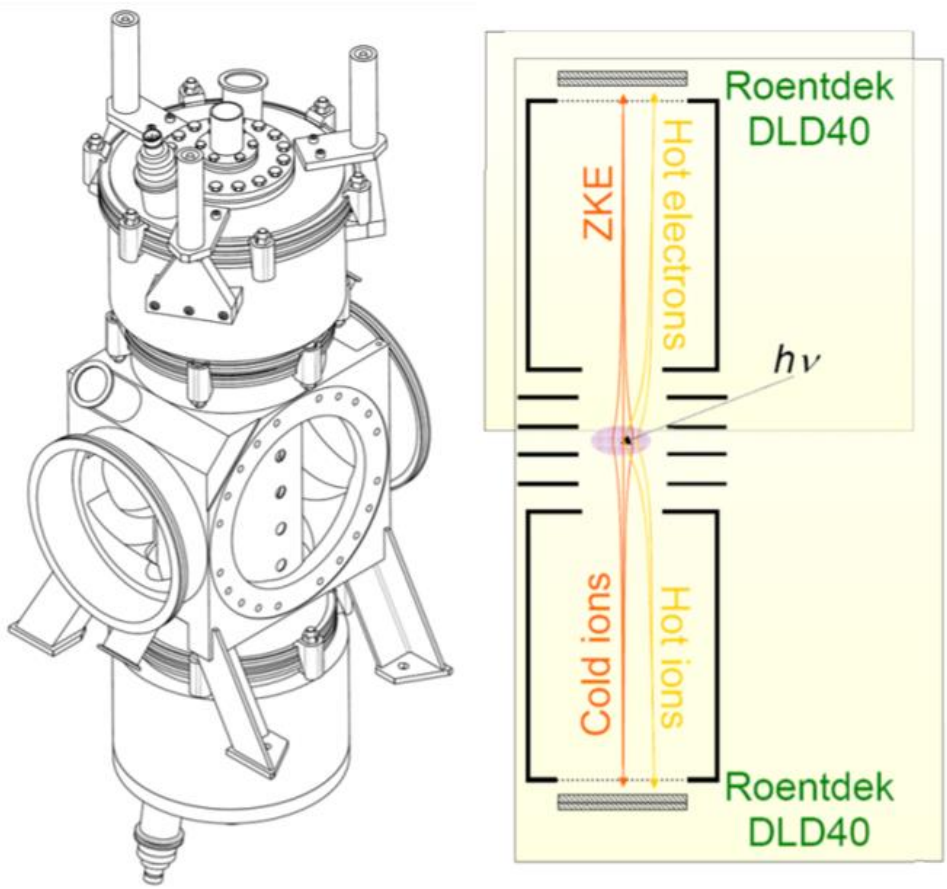

Figure 2.11 Drawing and Schematic of the symmetric set-up of the i^{2}PEPICO apparatus[22]

After ionization, a photoelectron is produced to trigger the ion time-of-flight analysis. As shown in the schematic presented in Figure 2.11, photoions and photoelectrons move in opposite directions from the ionization chamber. The zero kinetic energy electrons (ZKE) and "cold ions" are the species of interest in the PEPICO studies presented in this thesis. Electric fields created by two plates are used to accelerate and pull the photoelectrons (ZKE and "hot electrons") and photoions ("cold ions" and "hot ions") in their respective directions.[20, 25] To reach the detector, photoelectrons and photoions pass through a 20 mm opening, where velocity imaging occurs, and down a 265 mm electron flight tube that connects to the Roentdek DLD40 delay line detector.[20, 25-26] ZKE electrons and "cold ions" move in a straight direction and hit the center of the detector, while "hot electrons" and "hot ions" travel at an angle and do not hit the center.[25]

The ZKE electrons and "cold ions" are considered to be in coincidence and correspond to the photoionization event.[25] Opposingly, the "hot electrons" and "hot ions" do not have zero kinetic energy and are subtracted out of the velocity imaging during data analysis.[25] An electron velocity image showing the distinction between ZKE and "hot" electrons is shown in Figure 2.12.

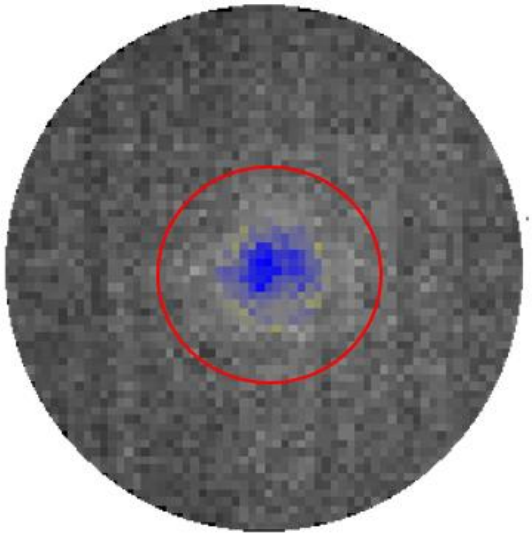

Figure 2.12 Electron velocity map image from i^{2}PEPICO experiment. Red circle indicates the "hot electrons" and the blue circle indicates the ZKE electrons.

Electron velocity images are produced by a customized program designed by Dr. Andras Bodi and is available on the official PSI website. The purpose of the i^{2}PEPICO program is to visualize the raw data outputted from the i^{2}PEPICO apparatus based on mapping information of the location of the photoelectrons collisions with the detector and TOF-MS data of the photoions.[27] The detector outputs data that represents the distribution of electrons as a function of their velocities before the final acceleration to the detector. The resulting image output is the electron velocity image. In reference to the velocity image in Figure 2.13, a yellow ring is graphically adjusted to lay on the "hot electrons" (red ring) and enclose the ZKE electrons (blue circle). Then, the program will average the area of the yellow ring and subtract the counts from the signal to ensure the signal is only a result of the ions in coincidence. A multichannel analyzer

is used to count the total number of active channels that give number points and these numbers are controlled by an input script to the i^{2}PEPICO program. The script is optimized to best visualize the signal and further reduce noise produced from the "hot electrons". The i^{2}PEPICO program produces a list of the coincidence counts from the entire electron velocity map image as a series of numbers.[27] The data is extrapolated, and a weight factor is applied to determine the count of only the ZKE electrons. From the counts, fraction abundances for each mass-to-charge ratio are determined and plotted as a function of photon energy to produce a breakdown diagram. Further details about data processing are described in Chapter 3.

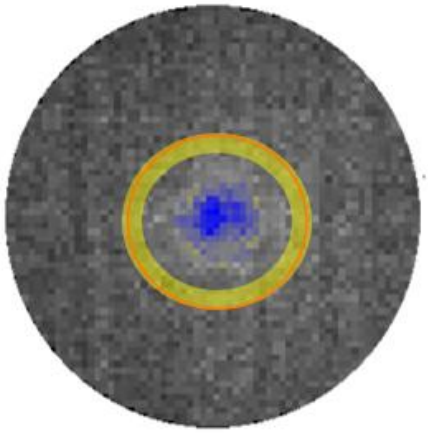

Figure 2.13 Electron velocity map image from i^{2}PEPICO experiment during image processing. The yellow ring is graphically adjusted and inputted by the i2PEPICO program.

2.3 References

1. Advanced Light Source 2017 Quick Facts. https://als.lbl.gov/wp-content/uploads/2016/06/quick-facts.pdf.
2. The Advanced Light Source-a Tool for Solving the Mysteries of Materials. http://www2.lbl.gov/MicroWorlds/ALSTool.
3. Hardware Beamline 9.0.2 Mini-Tour. http://www.chemicaldynamics.lbl.gov/tour.html.
4. Suits, A. G.; Heimann, P.; Yang, X.; Evans, M.; Hsu, C.-W.; Lu, K.-t.; Lee, Y. T.; Kung, A. H., A Differentially Pumped Harmonic Filter on the Chemical Dynamics Beamline at the Advanced Light Source. *Rev. Sci. Instrum.* **1995,** *66* (10), 4841-4.
5. Osborn, D. L.; Zou, P.; Johnsen, H.; Hayden, C. C.; Taatjes, C. A.; Knyazev, V. D.; North, S. W.; Peterka, D. S.; Ahmed, M.; Leone, S. R., The Multiplexed Chemical Kinetic

Photoionization Mass Spectrometer: A New Approach to Isomer-Resolved Chemical Kinetics. *Rev. Sci. Instrum.* **2008,** *79* (10, Pt. 1), 104103/1-104103/10.
6. Heimann, P. A.; Koike, M.; Hsu, C. W.; Blank, D.; Yang, X. M.; Suits, A. G.; Lee, Y. T.; Evans, M.; Ng, C. Y.; et, a., Performance of the Vacuum Ultraviolet High-Resolution and High-Flux Beamline for Chemical Dynamics Studies at the Advanced Light Source. *Rev. Sci. Instrum.* **1997,** *68* (5), 1945-1951.
7. Ball, D. W., *Field Guide to Spectroscopy*. Vol. FG08, p 124.
8. Laboratory, L. L. N. How Lasers Work. https://lasers.llnl.gov/education/how_lasers_work.
9. Whiteman, D. N.; Murphy, W. F.; Walsh, N. W.; Evans, K. D., Temperature sensitivity of an atmospheric Raman lidar system based on a XeF excimer laser. *Opt. Lett.* **1993,** *18* (3), 247-249.
10. Romanzin, C.; Boye-Peronne, S.; Gauyacq, D.; Benilan, Y.; Gazeau, M. C.; Douin, S., CH Radical Production from 248 nm Photolysis or Discharge-Jet Dissociation of CHBr3 Probed by Cavity Ring-Down Absorption Spectroscopy. *J. Chem. Phys.* **2006,** *125* (11), 114312/1-114312/9.
11. Zou, P.; Shu, J.; Sears, T. J.; Hall, G. E.; North, S. W., Photodissociation of Bromoform at 248 nm: Single and Multiphoton Processes. *J. Phys. Chem. A* **2004,** *108* (9), 1482-1488.
12. Wiley, W. C.; McLaren, I. H., Time-of-Flight Mass Spectrometer with Improved Resolution. *Review of Scientific Instruments* **1955,** *26* (12), 1150-1157.
13. Gross, J. H., *Mass Spectrometry*. 2nd ed.; Berlin Heidelber Springer: 2011.
14. Vacuum, P. Turbomolecular Pumps Operating Principles. https://www.pfeiffer-vacuum.com.
15. Vacuum Technology. In *Ullmann's Encyclopedia of Industrial Chemistry*.
16. Liu, F. C. H. A (not so) short introduction to MEMS. http://memscyclopedia.org/introMEMS.html.
17. Muller, G. Photooxidation Reactions of Small-Chain Methyl Esters, Aerosol Photoelectron

Spectroscopy, and the Photodissocation of Ethylenediamine. University of San Francisco, 2015.
18. 2 Lobes Roots Pump. http://www.mekanizmalar.com/.
19. Institute, P. S. Swiss Light Source. https://www.psi.ch/sls/swiss-light-source.
20. Winfough, M.; Voronova, K.; Muller, G.; Laguisma, G.; Sztáray, B.; Bodi, A.; Meloni, G., Furfural: The Unimolecular Dissociative Photoionization Mechanism of the Simplest Furanic Aldehyde. *The Journal of Physical Chemistry A* **2017,** *121* (18), 3401-3410.
21. Johnson, M.; Bodi, A.; Schulz, L.; Gerber, T., Vacuum ultraviolet beamline at the Swiss Light Source for chemical dynamics studies. *Nuclear Instruments and Methods in Physics Research Section A: Accelerators, Spectrometers, Detectors and Associated Equipment* **2009,** *610* (2), 597-603.
22. VUV Photoionizaition Overview. Institute, P. S., Ed. Villigen PSI, Switzerland.
23. Baer, T., Ion dissociation dynamics and thermochemistry by photoelectron photoion coincidence (PEPICO) spectroscopy. *International Journal of Mass Spectrometry* **2000,** *200* (1), 443-457.
24. Buckland, J. R.; Folkerts, R. L.; Balsod, R. B.; Allison, W., A simple nozzle design for high speed-ratio molecular beams. *Measurement Science and Technology* **1997,** *8* (8), 933.

25. Bodi, A.; Johnson, M.; Gerber, T.; Gengeliczki, Z.; Sztáray, B.; Baer, T., Imaging photoelectron photoion coincidence spectroscopy with velocity focusing electron optics. *Review of Scientific Instruments* **2009,** *80* (3), 034101.
26. Bouwman, J.; Sztáray, B.; Oomens, J.; Hemberger, P.; Bodi, A., Dissociative Photoionization of Quinoline and Isoquinoline. *The Journal of Physical Chemistry A* **2015,** *119* (7), 1127-1136.
27. Bodi, A. *i2PEPICO software tools*.

Chapter 3 Theory

Understanding theoretical concepts of photoionization (PI) and kinetics is essential to the research presented in this thesis. PI spectra and kinetic time traces are used to identify and characterize reaction species from a given reaction. Computational methods are used to produce potential energy surface (PES) scans to determine all the proposed reaction mechanisms. The process to analyze ALS experimental data, which utilizes these theoretical concepts, will be explained in detail. Additionally, photodissociation and thermodynamic concepts related to i^2PEPICO experiments will also be described, along with details about computational modeling to analyze experimental data.

3.1 Theoretical Concepts

3.1.1 Ionization

A photochemical reaction occurs when light interacts with an atom or molecule and causes a chemical or physical change.[1] In this research, two types of photochemical reaction are studied and illustrated below:[1]

$$\text{Ionization: } A + h\nu \rightarrow A^+ + e^-$$

$$\text{Dissociation (Dissociative Ionization): } A + h\nu \rightarrow B^+ + C$$

In an ionization reaction, a compound becomes charged due to the loss of electrons. More specifically, this research investigates photoionization where light (or photons (hν)) is used to eject an electron from a neutral compound (A) that becomes a cation (A^+). In spectroscopy, the minimum amount of energy needed to eject an electron is known as the compound's adiabatic ionization energy (AIE).[1-2] The ionization energies are influenced by the molecules bonding and electronic characteristics.[1-2]

The two types of ionization energies are adiabatic and vertical. Their main difference is the geometry of the resulting ion, which is based on the specific final energy level of the transition. [1-3] Vertical ionization energy (VIE) refers to the ionization energy where the ion has the same geometry as the neutral compound. On the other hand, AIE refers to ionization energy where the ion is at the lowest and most relaxed geometry, which may or may not be different from the neutral. Figure 3.1 illustrates the two transitions in a potential energy diagram for a diatomic molecule. The adiabatic transition would result in an ion with a slightly longer bond length than the neutral. Both types of transitions are further explained by Born-Oppenheimer approximation and Franck-Condon principles later in this chapter.

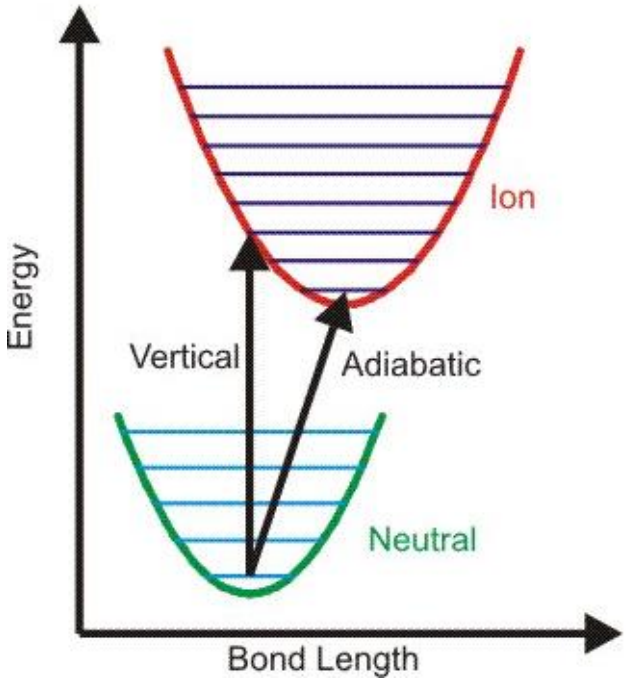

Figure 3.1 Potential energy diagram for a diatomic molecule[3]

The adiabatic ionization energy (AIE) is always smaller than vertical ionization energy and represents the energy difference between the two potential energy surfaces absolute

minima.[1-2] AIE is calculated from the differences of the vibronic ground states using the equation below:

$$AIE = E_0 \text{ cation} - E_0 \text{ neutral} \qquad \text{(Equation 3.1)}$$

The greater the overlap between the two ground states in the transition, the closer the AIE is to the VIE.[2] Calculated AIE can be compared to experimental AIE to help identify unknown species.

3.1.2 Photoionization Spectra

In spectroscopy, a photoelectron spectrum measures the energy change in an ion when an electron is lost from a neutral molecule. When a PE spectrum is integrated, it yields a photoionization (PI) spectrum, which is used to characterize the ionization of a molecule. Also, a PI spectrum can provide useful information about an unknown molecule's structure and bonding. Each PI spectrum is unique to a specific molecule and can even help differentiating between isomers. The onset of a curve is the same as the AIE and the shape of the curve is determined by the specific ion geometry and, therefore, Franck-Condon (FC) factors.

Experimentally, PI spectra are known as photoionization efficiency (PIE) curves and are generated when photoionization is coupled with mass spectrometry. The resulting ions are separated by mass and assigned to single mass-to-charge (m/z) ratios. A PIE spectrum shows a specific m/z ratio's relative ion signal as a function of photon energy and is proportional to its photoionization cross section. Further details on experimental data processing and cross sections will be discussed later in this chapter. A PI spectrum can also be generated by integrating a FC simulated PE spectrum with a calculated AIE. In this research, these methods are utilized when experimental reference PI or PE spectra are unavailable. As previously mentioned, PE spectra

are reflective of molecule's unique FC factors. To calculate these FC factors, the Born-Oppenheimer approximation and Frank-Condon principle must be applied.

3.1.3 Born-Oppenheimer approximation and Franck-Condon principle

The Born-Oppenheimer approximation allows for electron and nucleus wave functions to be separated based on velocity differences.[4-5] Electrons move at a much faster velocity than nuclei, therefore, an electronic transition takes place so quickly that nuclei can be considered initially stationary in the ionization process.[4-5] Using the equation below, the Schrödinger equation is now solvable to yield values for energy and wavefunction of the given molecule.[5]

$$\Psi \text{ molecule} = \Psi \text{ nucleus} \times \Psi \text{ electron} \qquad \text{(Equation 3.2)}$$

The Franck-Condon principle builds upon the Born-Oppenheimer approximation and explains that since the nuclei are considered stationary, it can be also assumed that bond lengths, bond angles, and positions do not change during ionization.[1, 4, 6] Therefore, an electronic transition can be considered a vertical transition. After the electronic transition or ionization, electron density increases enough to cause the nucleus to vibrate and displace energy.[1, 4, 6-7] The energy displacement causes a vibrational transition, where an electron moves from one vibrational level to another, to occur in sequence with an electronic transition.[4, 7] The combination of these two transitions is known as a vibronic transition.[1] The FC principle is used to describe the intensity of a vibronic transition by stating that the probability of a transition to a certain vibrational energy level is higher when the overlap of the ground states between the two levels is greater.[4, 7] As previously mentioned, the greater the overlap, the less change in molecular geometry occurred in the ionization process. In the energy diagram below, the FC principle is illustrated where each vibrational level is expressed as a wave function. (Figure 3.2) The blue and green arrows show the vibronic transitions where minimal configuration change

occurs for electron emission and absorption, respectively. These transitions have the greatest overlap and would, therefore, have the highest probability of occurring.

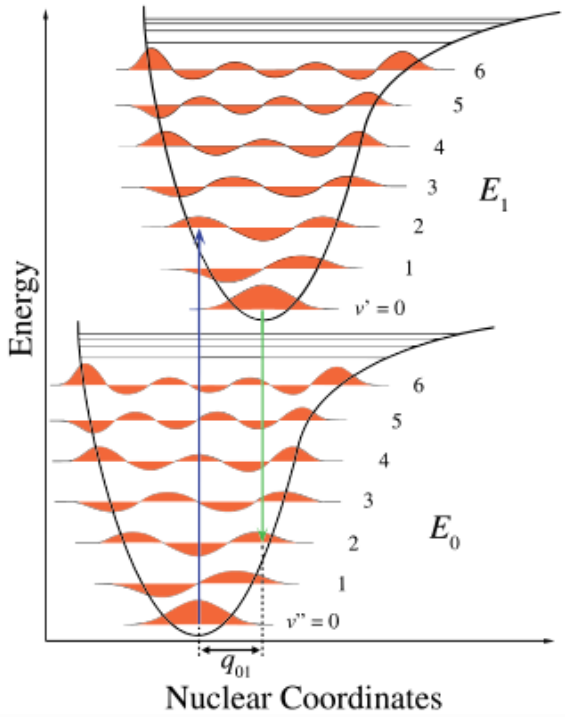

Figure 3.2 Potential energy diagram illustrating Franck-Condon Principle for a diatomic molecule[8]

The probability of a specific vertical transition is represented as a Franck-Condon factor and is calculated using the equation below.[4, 6, 8]

$$\text{Franck-Condon Factor } (R_e) = \left|\int \Psi_e' \, \mu \, \Psi_e'' dR\right|^2, \qquad \text{(Equation 3.3)}$$

where Ψ are the wavefunctions of the initial and final state of the electronic transition and μ is the electric dipole moment operator. As shown in the equation, a FC factor is proportional to the square of the first overlap integral between the wavefunctions of the vibrational levels involved in the transition. Utilizing a recursive formula developed by Ruhoff, FC factors and overlap integrals are calculated to simulate PE spectra, with FC and Franck-Condon-Herzberg-Teller methods, for use in the research presented in this thesis.[6]

3.1.4 Photoionization Cross Sections

Photoionization cross sections (PICS) refer to the area in which there is the highest probability that a molecule will ionize.[1, 9] More specifically, PICS is the area in which there is the highest probability of an electron being emitted from a gaseous molecule, which is directly proportional to the number of photons that collide with the molecule.[9, 10-12]

Absolute Photoionization Efficiency (APIE) spectra can be determined by comparing experimental data with data of well-known species. In experimentation, a known concentration of the compound of interest is flowed in with a calibration gas consisting of well-known species and the results are compared. The individual compounds' relationship can be shown and calculated by the equation below:[9, 11]

$$S(E) = k\sigma(E)\delta C \qquad \text{(Equation 3.4)}$$

S is the ion signal, σ is the PI cross section, δ is the mass dependent response, and C is the concentration of the specified compound. The ion signal and PICS of the compound of interest are all relative in relation to the well-established values of the compounds in the calibration gas and are energy dependent. Therefore, it is important to use the same energy (E) throughout all calculations. Due to the relative nature of the results, unknown cross sections are typically expressed as a ratio of the factors in the equation above to those factors for the species' in the calibration gas. The ratio is expressed by the equation below where X represents the unknown and S represents the standard:[9, 11]

$$\sigma_X = S_X\sigma s\delta s C s \,/\, S s\delta_X C_X \qquad \text{(Equation 3.5)}$$

PICs are necessary to calculate branching fractions of reaction products. A branching fraction is the comparison of the concentration of a product to the concentration of the reactant. They are also directly proportional to the efficiency of ionization, which is low at energies close

to the ionization energy of a given species. Like the equation above, the equation used to calculate branching fractions, shown below, is a ratio of concentrations and ion signal of the reactant to that of the product: [9, 11, 13]

$$C_P/C_R = S_P\sigma_R\delta_R/ S_R\sigma_P\delta_P \qquad \text{(Equation 3.6)}$$

P denotes the product's factors and R represents the reactant's factors. The mass dependent response is calculated by the mass of a given species taken to the power of 0.67.[11]

When APIE are unavailable or PI spectra result from a summation of species, PICS can be calculated using the additivity rule. The equation below is used to calculate PICS based on the additivity rule:[14]

$$\sigma = \Sigma \sum_{i=1}^{n} x_i\sigma_i \qquad \text{where } \sum_{i=1}^{n} x_i = 1 \qquad \text{(Equation 3.7)}$$

The additivity rule uses the mole fraction (x) and PICS (σ) of the of the ith isomer for its estimation.[14]

3.2 Computational Methods

Using Gaussian 09 computational program, electronic structure calculations (ESC) and PES scans are used to calculate energy values, simulate PI spectra, find activation barriers, and determine optimal mechanism pathways.[15] The purpose of these calculations is to support identification and characterization of reaction species from experimental data. All calculations in this thesis are computed using the Becke, 3-parameter, Lee-Yang-Parr (B3LYP) level of theory and the Complete Basis Set Quadratic B3LYP (CBS-QB3) composite method.

3.2.1 Electronic Structure Calculations

Electronic structure calculations (ESC) are performed using the CBS-QB3 model, which yields the most reliable and accurate geometries and energetics for the capabilities of our

research lab at a relatively low computational cost. Zero-point vibrational corrected electronic energies (ZPE) and molecular harmonic frequencies are the useful values produced from ESC.

In an ESC, a structure is drawn in GaussView 5.0 and the coordinates are optimized to find the geometry with the lowest energy. ZPE corrected total electronic energies of the cation and neutral structures are used to calculate AIE for a given molecule. As previously mentioned, the calculated AIE is then used in FC simulations and to compare to experimental data. Any enthalpy change calculations also use the ZPE-corrected values as shown in the equation below:

$$AIE = ZPE_{cation} - ZPE_{neutral},$$

$$\Delta H = \Sigma ZPE_{products} - \Sigma ZPE_{reactants} \qquad \text{(Equation 3.8)}$$

The "B3", or B3LYP, portion of the method is used in ESC to calculate bond distances and harmonic vibrational frequencies.[16-17] The approximated molecular orbitals, which are based on the inputted molecular structure, is mathematically represented by the all electron 6-311+G* basis.[17-18] The basis set in any level of theory is composed of linear combinations of pre-defined one-electron functions.[17-18] The treatment of electrons is essential and unique to the different methods and will be discussed later in this section.

3.2.2 Potential Energy Scans

PES uses the B3LYP method to calculate energy changes as a specific bond length or atom is modified. These modifications can be programmed to break or form new bonds as well as transfer atoms within the molecule. A PES shows changes in enthalpy as a graph for each "step" of a movement with regards to ideal gas conditions, kinetics, and the laws of thermodynamics. Thermochemistry values for structures at each "step" are influenced by electronic, vibrational, and rotational frequencies.[18-19] The structures at local minimum and

maximum points are further optimized by CBS-QB3 to report more accurate energetics. An example of a PES scan with a complimentary energy graph is shown in Figure 3.3.

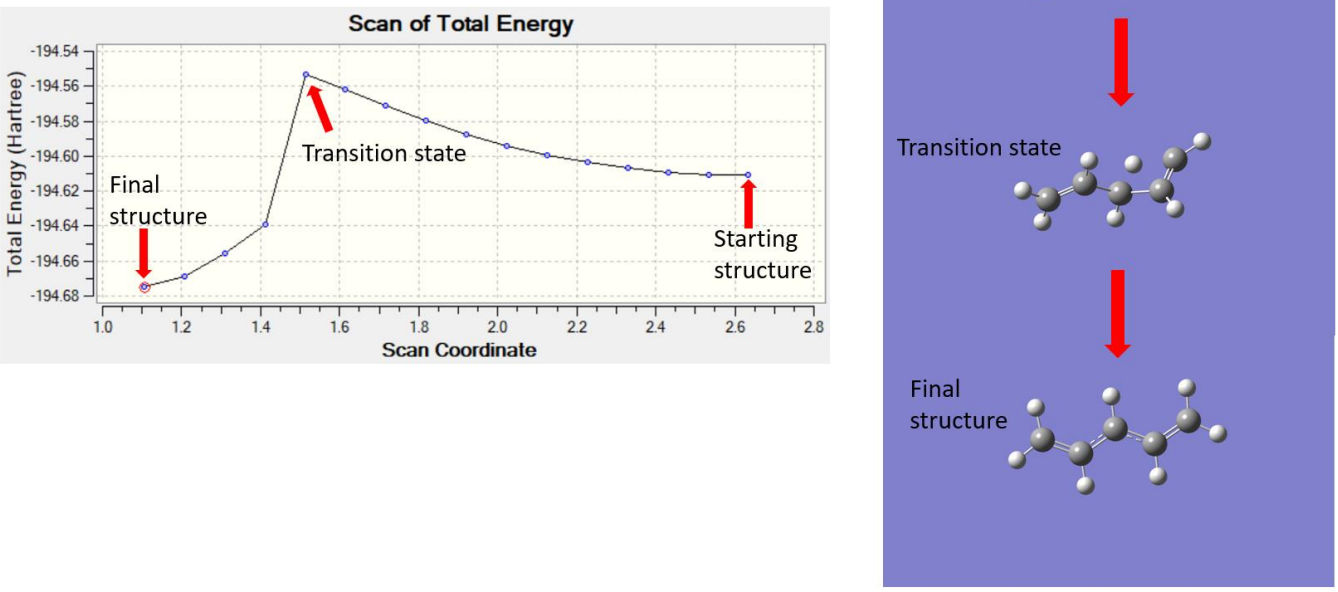

Figure 3.3 PES energy change graph from GaussView for a hydrogen transfer run on Gaussian 09. The starting structure, local maximum/transition state, and local minimum/final structure are labeled.

B3LYP method is used in PES to determine any barriers in a mechanism pathway and identify reaction species, including products and intermediates. Transition states and their CBS-QB3 calculated energies are considered the activation energy barriers for the proposed mechanism. In the PES scan shown in Figure 3.3, the transition state, also known as the saddle point or local maximum, is found from the top point of the scan. The transition state has 1 imaginary frequency and the positive frequencies are used to calculate rate constants and thermochemistry values of a dissociation with the RRKM theory discussed later in this section. PES is also used to find the global minimum, which has the lowest possible vibrational electronic

level (Figure 3.3). This structure is then optimized by CBS-QB3 to report the most energetically favorable energy state and molecular configuration.

3.2.3 Computational Theories

CBS-QB3 is composed of several methods in a specific order to compute electronic thermochemical values while optimizing molecular geometry and ZPE. [16-18] The B3LYP method is included in the CBS-QB3 composite method to better optimize the molecular geometry and frequencies.[16-17] The method order of CBS-QB3 is listed below: [17]

(i) B3LYP/6-31G
(ii) UMP2/6-311+G(3d2f,2df,2p)
(iii) MP4(SDQ)/(6-31+G(d(f), p)
(iv) QCCSD(T)/6-31+G

Steps (ii)-(iv) are all performed at the optimized geometry yielded from step (i) and calculate ZPE values.[17] Step (iii) also calculates CBS extrapolation to deduce the total energy to an infinite-basis-set limit.[17] CBS-QB3 composite method works to overcome as much basis set truncation error as possible and was found to have a relatively small error of 1-1.5 kcal/mol.[18]

The B3LYP method belongs to the density functional theory (DFT) that builds upon the Hartree-Fock (HF) method. Both the Hartree-Fock and CBS methods do not take into consideration electron-electron interactions and the purpose of B3LYP addition is to consider them for molecular geometry optimization and energy calculations.[16-18] HF method is an ab initio method that calculates the lowest energy state of a system with the all electron effects viewed as an average.[16-17, 19] Whereas, DFT method uses a function to describe the ground state energy and density of a molecule while accounting for the kinetic energy of electrons.[16-17] The contributing electron energy includes any attraction or repulsion between electrons and nuclei, electron-electron interactions, and an exchange correlation for other electron-electron interactions.[16-17, 19]

B3LYP is a DFT method that depends on both electron density and gradient in a molecule, also known as a gradient-correct exchange functional.[16-17] B3LYP method used in this research is the combination of HF, BLYP, and potential energy from the exchange correlation of electron-electron interactions.[17, 19]

3.3 ALS Data Analysis

Experimental data from ALS synchrotron photoionization reactions is collected as a three-dimensional data set of intensity as a function of photon energy, reaction time, and m/z ratio. Using a kinetic procedure file developed by researchers at Sandia Laboratories, the 3-D data is visualized and processed using Igor 6.37 Wavemetrics program.[20] Following background subtraction, the ion signal is normalized to account for any fluctuation in the photon light source. To reduce the 3-D image to 2-D images, either energy or time is set as a fixed variable and then the 2-D image is "sliced" into one-dimensional images at specific m/z ratios.[21] From the 2-D image with a fixed photon energy, kinetic time traces are produced, which show relative ion signal versus time. Whereas, PI spectra are produced from a 2-D image with a fixed time range and show relative ion signal versus a photon energy. Figure 3.4 illustrates the "slicing" process of a 3-D data set.

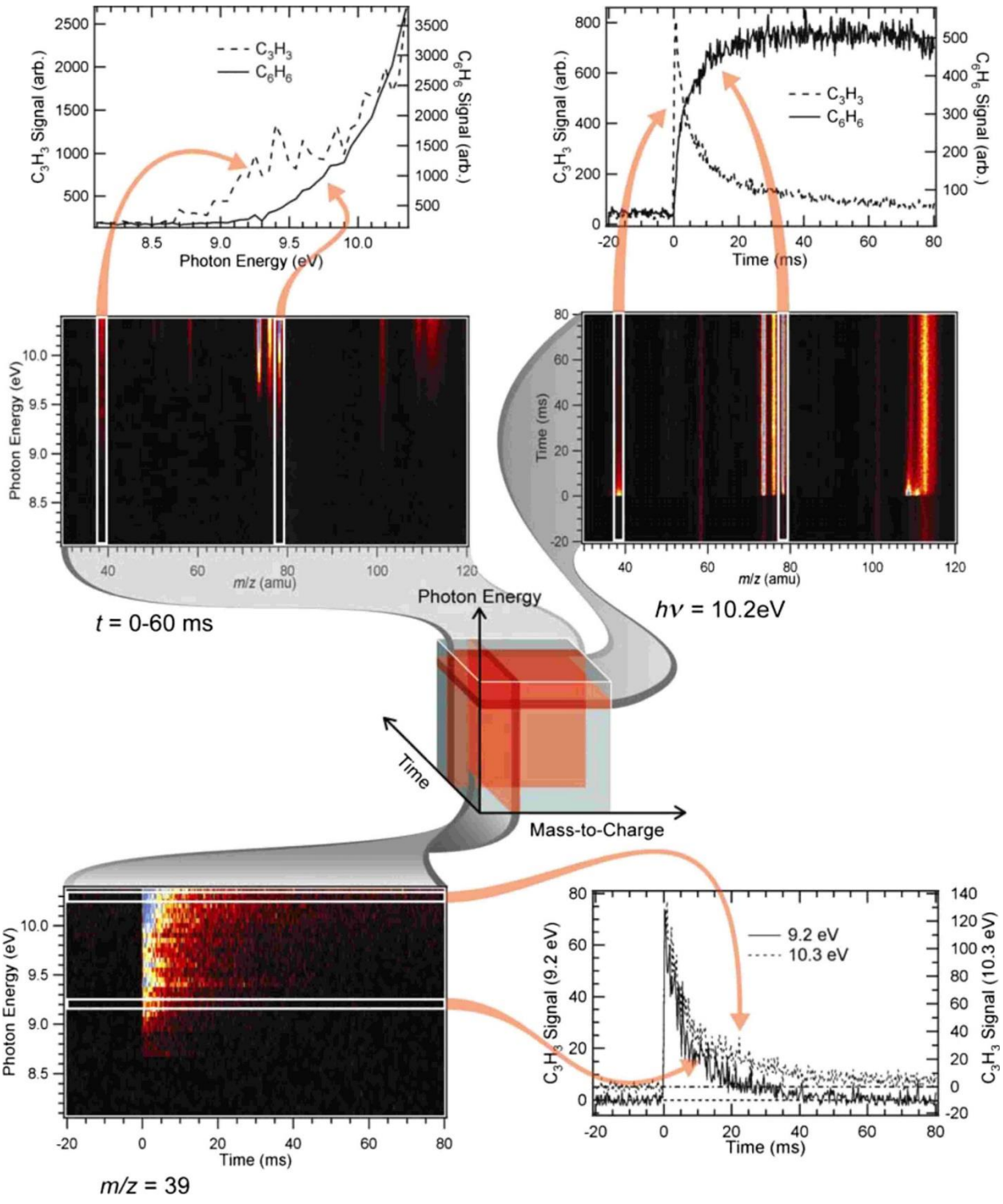

Figure 3.4 Processing of three-dimensional data to one dimensional kinetic time trace and PI spectra.[21]

Using the kinetic time traces of reaction species, primary products can be identified. This research only investigates primary products and their reaction mechanisms. The kinetic time trace of the parent molecule should show as a negative ion signal, or a depletion curve. Opposingly, a product will have a positive ion signal showing a formation curve. A primary product should form at the same rate (or similar rate) that the parent depletes, therefore the inverse of the parent's kinetic time trace should match that of the proposed primary product. Figure 3.5 shows a depletion curve for a parent compound and its inverse superimposed onto a primary product. If the parent's inverse and product kinetic time traces are a match, as shown in Figure 3.4, then the product is considered to be most likely primary (however, we cannot rule out very fast secondary reactions that could occur; in this sense, the computation of the PES can help in explaining and identifying possible primary species). Kinetic time traces can also identify radical species and secondary products. A radical species will have a time trace with a sharp rise and rapid depletion curve showing fast formation and fast consumption. (Figure 3.6) A secondary or tertiary product will have a slow formation onset that does not match the parent's inverse. (Figure 3.6)

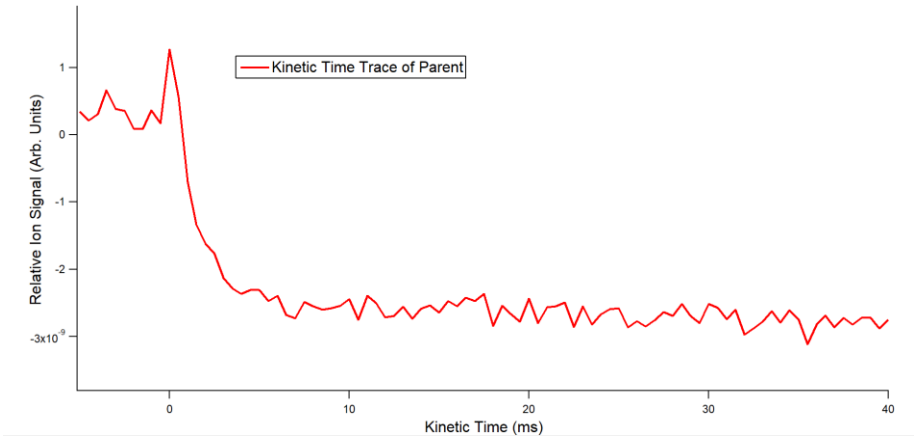

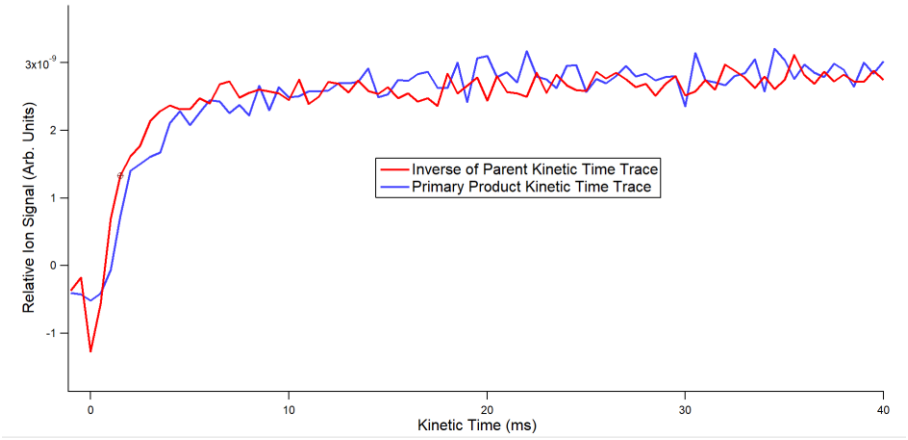

Figure 3.5 Kinetic time trace comparisons of a parent and a primary product

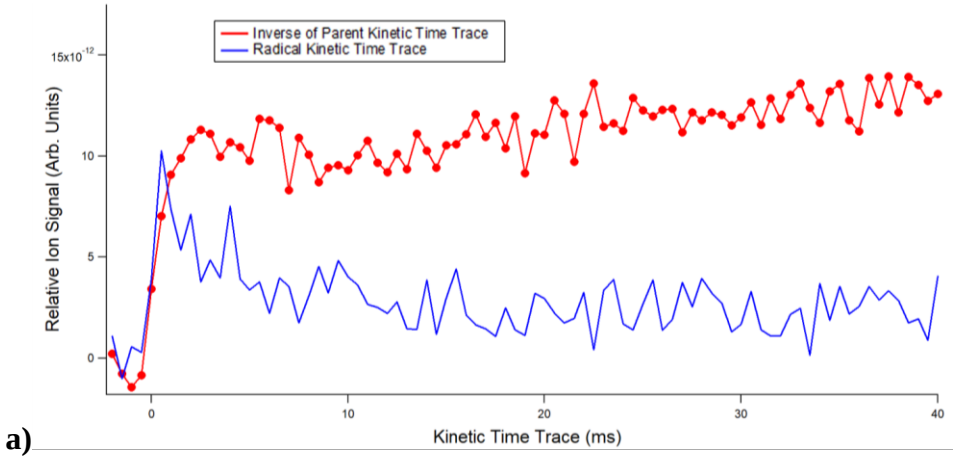

a)

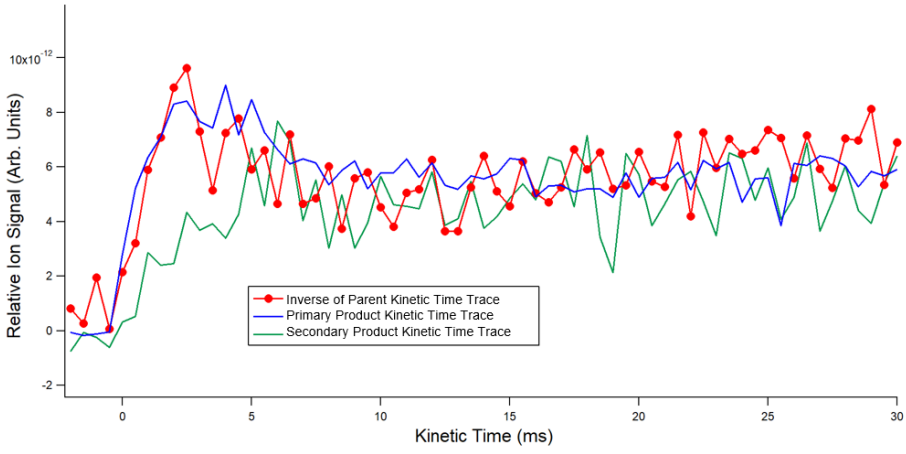

b)

Figure 3.6 a) Kinetic time trace of parent (red) compared to a radical species (blue). b) Kinetic time trace of parent (red) compared to a primary product (blue) and a secondary product (green).

Experimental PI spectra are used to characterize and identify the primary products. To produce clearer PI spectra, time is fixed at a set range rather than the entire length of the

experiment to best minimize secondary and tertiary products based on the kinetic time trace of the parent. As previously mentioned, reference and simulated PI spectra are used to identify unknown species**.** Figure 3.7 shows an experimental PI spectrum at m/z = 52 overlaid with a reference spectrum for vinylacetylene and identified as a successful match. Multiple products at the same m/z ratio are also possible and can be identified in the same manner through a summation curve of the proposed products. From experimental PI spectra, experimental AIE values can also be calculated using linear extrapolation of the curve's onset.[22] The ion signals from the experimental curves are also used to calculate PICS and fractional abundance.

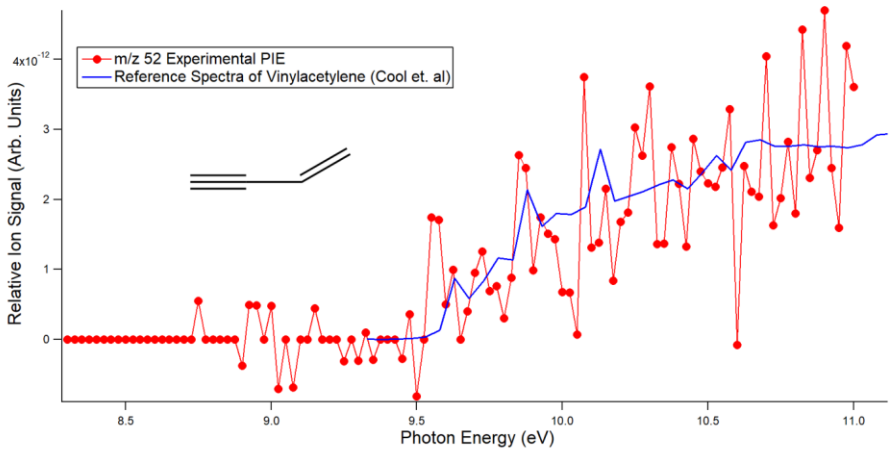

Figure 3.7 Experimental PIE spectra for m/z = 52 (red) compared to reference PI spectra of vinylacetylene (blue).

3.4 Photodissociation and Photoionization Concepts

3.4.1 Dissociation and Thermodynamics

The PEPICO experiments presented in this thesis involve dissociative photoionization by VUV synchrotron radiation. Dissociative photoionization occurs when a molecule is excited with an amount of energy, from the light source, that is more than the AIE needed to ionize. [1, 3, 23] The energy increase causes the molecule to lose an electron and become a cation.[1, 3, 23] The resulting cation will then dissociate and break down into daughter ions and neutral fragments. [1, 3, 23]

Most current and common experiments are unimolecular dissociations. A simplified dissociative photoionization is shown in the equation below[1]:

$$AB + hv \rightarrow A^+ + B + e^- \qquad \text{(Equation 3.9)}$$

Studying these reactions can provide information about ion dissociation rates, translational energy values, and breakdown diagrams.[24] Breakdown diagrams are graphs that show relative abundance as a function of ion internal energy for dissociation reaction species.[24] Further interpretation of experimental data can lead to determining the dissociation mechanism and thermochemistry values for the different channels.

When coupled with mass spectrometry, appearance energies (AE), can be measured for the cation fragments.[24] Dissociation barriers are determined and calculated with potential energy surface scans described previously. When no dissociation barriers are present, or the PES determines that mechanism is "uphill", the bond dissociation energy (BDE) can represent the AE of the cation fragment. This is also called thermochemical limit. BDE is the difference between the energy of the parent and the energy of the fragments.[24] To calculate enthalpy values, experimental AE values are used in the equation below.[24-25]

$$AE \approx \Delta_{rxn}H = \Delta_f H\,(A^+) + \Delta_f H\,(B) - \Delta_f H\,(AB) \qquad \text{(Equation 3.10)}$$

Enthalpy values are taken at 0 K and the heats of formation for known species can be used to solve for any of those that are unknown.

3.4.2 PEPICO Technique

To study the dissociation rates and thermochemistry of ions, production of ions with well-defined energy states is required. However, the photon energy produced by the VUV beamline used in the ionization process contributes to the resulting ion's internal energy (IE) and

the kinetic energy (KE) of the electron. [24] Therefore, the ions produced have a range of internal energies instead of a selected energy.[24] The ionization process is shown in the equation below.[24]

$$AB + hv \rightarrow AB+ (E_{int}) + e^- (KE) - IE \qquad \text{(Equation 3.11)}$$

However, when coupled with the i^{2}PEPICO spectroscopy technique, the VUV light can be used to isolate ions with well-defined energy states[25].

As previously mentioned in Chapter 2, the i^{2}PEPICO apparatus allows for photoelectrons and photoions to be measured and imaged at the same time to determine which ions correspond to a photoionization event. Thus, by selecting a specific energy at which to collect electrons, the energy of ions can also be carefully chosen. [24] Thermochemistry data can be calculated based on the now very well-defined internal energies of the ions.[24] The precision of the internal energy is orders of magnitudes better than that of traditional mass spectrometry. [26] Unfortunately, there is still a very low collection efficiency, which is the reason why a continuous photoionization source is needed. [24]

3.4.3 miniPEPICO Computational Modeling

MiniPEPICO, developed by Sztaray et al.[26], is a computational program that analyzes the dissociation of molecules to produce a theoretical breakdown diagram to compare to experimental data. Using the RRKM theory, thermal energy distribution of the ions is calculated as a function of photon energy with account to dissociation rates.[26] The program can also model parallel and consecutive dissociation mechanisms.

Breakdown diagrams help visualize the dissociation pathways through relative abundance of the reaction species. A fast, parallel dissociation is shown in Figure 3.8 with miniPEPICO modeled dissociation curves overlaid onto experimental data. Like the i^{2}PEPICO experimental technique, which relies on having well-defined internal energies of ions, the miniPEPICO

program also analyzes dissociation of a molecule in terms of internal energy distribution.[26] The ratio of the parent ion to the fragment ion for a fast, single dissociation can be calculated by the equation below:

$$BD(h\nu) = \int_0^{E_0 - IE} P_i(h\nu) dE, \qquad \text{(Equation 3.12)}$$

where P is the normalized internal energy distribution of the parent ion as a function of the internal energy at a specific photon energy. [26] This equation shows how an increase in photon energy shifts energy distribution to favor more dissociation. The reaction begins at the parent molecule's IE, where the parent is a cation at 100% abundance and no fragments are forming. As the photon energy increases, the energy distribution will shift to higher energies and more internal energy distribution (P_i) will rise above the dissociation limit until $h\nu = E_0$ and the ratio is at zero. Fragment daughter ions will begin to form at their relative AE as the parent cation depletes. The theoretical dissociation curves in the modeled breakdown diagram can be fitted to the experimental curves to identify accurate AE of ion fragments. From the AE values, thermochemistry values of the reaction species can be calculated.

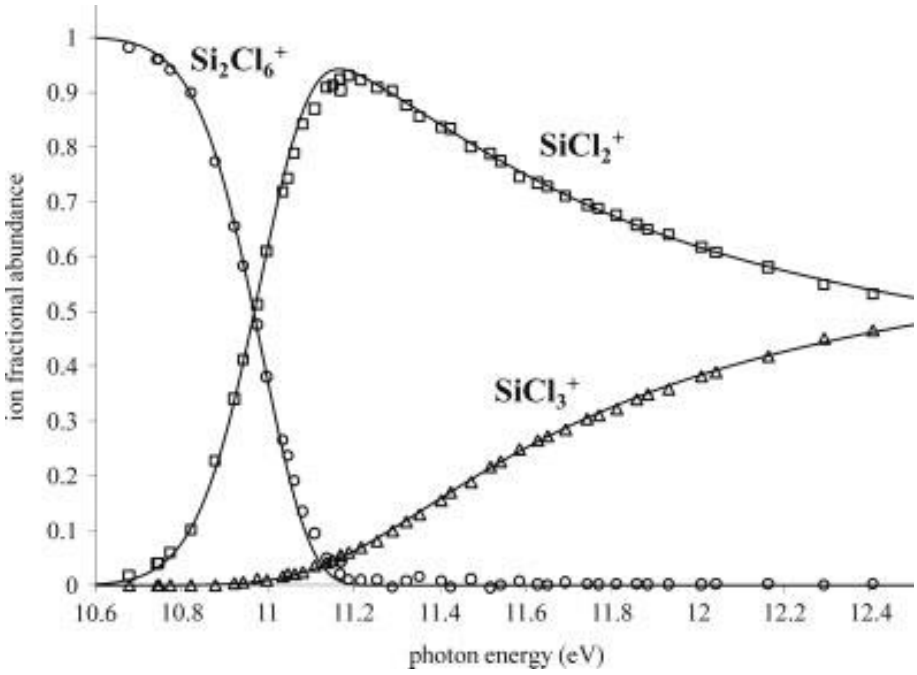

Figure 3.8 Breakdown diagram of Si_2Cl_6. Solid lines are the theoretical dissociation curves and the points are the experimental data.[26]

The RRKM theory assumes that a molecule is made up of linked harmonic oscillators where energy can be distributed within the molecule much quicker than any reaction[27-28]. Therefore, the energy from excitation that a molecule absorbs can be used to trigger a dissociation reaction.[27-28] Using these assumptions, RRKM theory calculates unimolecular dissociation rates based on vibrational and rotational frequencies of reaction species calculated from PES scans and ESC.[26-28] Specifically, those of the parent's neutral and cation form and the transition states to form each fragment. Dissociation rates are obtained using the common transition state theory expression shown in the equation below:

$$k(E) = \frac{\sigma N\ddagger(\mathrm{E}-E_0)}{h\rho(E)}, \quad \text{(Equation 3.13)}$$

where $N\ddagger(E - E_0)$ is the sum of states of the transition state, h is Planck's constant, $\rho(E)$ is the parent ion density of states, and σ is the reaction degeneracy.[26]

Dissociation reactions are characterized into fast and slow dissociations. In a fast dissociation, all of the studied ions have more energy than the dissociation limit and will lead to fragments.[24, 29] Analysis is only dependent on the breakdown diagram and no time-of-flight (TOF) analysis is necessary for further confirmation of the pathways.[24-25, 29] The experiments presented in this research are considered fast dissociations. The 0 K appearance energy for reaction species can be attained solely from fitting the model of the theoretical breakdown curves. In a slow dissociation, not all ions have enough energy within the experiment's time frame and a kinetic shift will be present in the experimental breakdown diagram.[24, 29] Therefore, it is necessary to also fit TOF distributions with the breakdown diagram and the modeling will provide absolute rate constants.[24, 29]

3.5 References

1. P. Atkins, J. De Paula, *Physical Chemistry*. Oxford, 2010; Vol. 9th.
2. Lang, P. F.; Smith, B. C., Ionization Energies of Atoms and Atomic Ions. *Journal of Chemical Education* **2003,** *80* (8), 938.
3. Technology, N. I. o. S. a. Computational Chemistry Comparison and Benchmark DataBase.
4. A different approach for calculating Franck–Condon factors including anharmonicity. *The Journal of Chemical Physics* **2004,** *120* (2), 813-822.
5. Haynes, P. D. Linear-scaling methods in ab initio quantum-mechanical calculations University of Cambridge, 1998.
6. Ruhoff, P. T., Recursion Relations for Multi-Dimensional Franck-Condon Overlap Integrals. *Chem. Phys.* **1994,** *186* (2), 355-374.
7. Sharp, T. E.; Rosenstock, H. M., Franck—Condon Factors for Polyatomic Molecules. *J. Chem. Phys.* **1964,** *41* (11), 3453-3463.
8. LibreTexts, C. The Franck-Condon Principle.
9. Czekner, J.; Taatjes, C. A.; Osborn, D. L.; Meloni, G., Absolute photoionization cross-sections of selected furanic and lactonic potential biofuels. *International Journal of Mass Spectrometry* **2013,** *348*, 39-46.
10. Welz, O.; Zádor, J.; Savee, J. D.; Ng, M. Y.; Meloni, G.; Fernandes, R. X.; Sheps, L.; Simmons, B. A.; Lee, T. S.; Osborn, D. L.; Taatjes, C. A., Low-temperature combustion chemistry of biofuels: pathways in the initial low-temperature (550 K–750 K) oxidation chemistry of isopentanol. *Physical Chemistry Chemical Physics* **2012,** *14* (9), 3112-3127.
11. Price, C.; Fathi, Y.; Meloni, G., Absolute photoionization cross sections of two cyclic ketones: cyclopentanone and cyclohexanone. *Journal of Mass Spectrometry* **2017,** *52* (5), 259-270.

12. Yang, B.; Wang, J.; Cool, T. A.; Hansen, N.; Skeen, S.; Osborn, D. L., Absolute photoionization cross-sections of some combustion intermediates. *International Journal of Mass Spectrometry* **2012,** *309*, 118-128.
13. Ng, M. Y.; Nelson, J.; Taatjes, C. A.; Osborn, D. L.; Meloni, G., Synchrotron Photoionization Study of Mesitylene Oxidation Initiated by Reaction with Cl(2P) or O(3P) Radicals. *J. Phys. Chem. A* **2014,** *118* (21), 3735-3748.
14. Bobeldijk, M.; van der Zande, W. J.; Kistemaker, P. G., Simple models for the calculation of photoionization and electron impact ionization cross sections of polyatomic molecules. *Chemical Physics* **1994,** *179* (2), 125-130.
15. Frisch, M. J. T., G. W.; Schlegel, H. B.; Scuseria, G. E.; Robb, M. A.; Cheeseman, J. R.; Scalmani, G.; Barone, V.; Petersson, G. A.; Nakatsuji, H. et. al. *Gaussian 09*, Gaussian Inc.: Wallingford CT, 2009.
16. Montgomery, J. A., Jr.; Frisch, M. J.; Ochterski, J. W.; Petersson, G. A., A Complete Basis Set Model Chemistry. VII. Use of the Minimum Population Localization Method. *J. Chem. Phys.* **2000,** *112* (15), 6532-6542.
17. Montgomery, J. A., Jr.; Frisch, M. J.; Ochterski, J. W.; Petersson, G. A., A Complete Basis Set Model Chemistry. VI. Use of Density Functional Geometries and Frequencies. *J. Chem. Phys.* **1999,** *110* (6), 2822-2827.
18. Sirjean, B.; Fournet, R.; Glaude, P.-A.; Ruiz-López, M. F., Extension of the composite CBS-QB3 method to singlet diradical calculations. *Chemical Physics Letters* **2007,** *435* (1), 152-156.
19. Tirado-Rives, J.; Jorgensen, W. L., Performance of B3LYP Density Functional Methods for a Large Set of Organic Molecules. *J. Chem. Theory Comput.* **2008,** *4* (2), 297-306.
20. Wavemetrics, I. *Igor Pro*, Portland, OR, 2013.
21. Osborn, D. L.; Zou, P.; Johnsen, H.; Hayden, C. C.; Taatjes, C. A.; Knyazev, V. D.; North, S. W.; Peterka, D. S.; Ahmed, M.; Leone, S. R., The Multiplexed Chemical Kinetic Photoionization Mass Spectrometer: A New Approach to Isomer-Resolved Chemical Kinetics. *Rev. Sci. Instrum.* **2008,** *79* (10, Pt. 1), 104103/1-104103/10.
22. Chupka, W. A.; Berkowitz, J., Photoionization of Ethane, Propane, and n-Butane with Mass Analysis. *J. Chem. Phys.* **1967,** *47* (8), 2921-2933.
23. Bellili, A.; Schwell, M.; Bénilan, Y.; Fray, N.; Gazeau, M.-C.; Al-Mogren, M. M.; Guillemin, J.-C.; Poisson, L.; Hochlaf, M., VUV photoionization and dissociative photoionization of the prebiotic molecule acetyl cyanide: Theory and experiment. *The Journal of Chemical Physics* **2014,** *141* (13), 134311.
24. Baer, T., Ion dissociation dynamics and thermochemistry by photoelectron photoion coincidence (PEPICO) spectroscopy. *International Journal of Mass Spectrometry* **2000,** *200* (1), 443-457.
25. Baer, T.; Sztáray, B.; Kercher, J. P.; Lago, A. F.; Bödi, A.; Skull, C.; Palathinkal, D., Threshold photoelectron photoion coincidence studies of parallel and sequential dissociation reactions. *Physical Chemistry Chemical Physics* **2005,** *7* (7), 1507-1513.
26. Sztáray, B.; Bodi, A.; Baer, T., Modeling unimolecular reactions in photoelectron photoion coincidence experiments. *Journal of Mass Spectrometry* **2010,** *45* (11), 1233-1245.
27. Di Giacomo, F., A Short Account of RRKM Theory of Unimolecular Reactions and of Marcus Theory of Electron Transfer in a Historical Perspective. *Journal of Chemical Education* **2015,** *92* (3), 476-481.

28. Unimolecular Dissociations and Free Radical Recombination Reactions. *The Journal of Chemical Physics* **1952,** *20* (3), 359-364.
29. Mazyar, O. A.; Mayer, P. M.; Baer, T., Isomerization and dissociation in competition: the two-component dissociation rates of methyl acetate ions. *International Journal of Mass Spectrometry and Ion Processes* **1997,** *167-168*, 389-402.

Chapter 4 Synchrotron Photoionization Study of Furan and 2-Methylfuran Reactions with Methylidyne Radical (CH) at 298 K ‡

‡As published in the Journal of Physical Chemistry A, *122* (1), pg. 280-291 (2018)

Erica Carrasco, Kenneth J. Smith, and Giovanni Meloni*

*Department of Chemistry, University of San Francisco, San Francisco, California 94117, USA

4.1 Abstract

The reactions of furan and 2-methylfuran with methylidyne CH ($X^2\Pi$) radical were investigated at 298 K using synchrotron radiation produced at the Advanced Light Source (ALS) of the Lawrence Berkeley National Laboratory. Reaction products were observed by multiplexed photoionization mass spectrometry and characterized based on their photoionization spectra and kinetic time traces. Primary products observed in furan + CH are 2,4-cyclopentadien-1-one (m/z = 80), 2-penten-4-ynal (m/z = 80), and vinylacetylene (m/z = 52). From 2-methylfuran + CH, 2-4-cyclopentadien-1-carbaldehyde (m/z = 94), 2,3,4-hexatrienal (m/z = 94), 1,3 cyclopentadiene (m/z = 66), 3-penten-1-yne (Z) (m/z = 66), and vinylacetylene (m/z = 52) are the primary products observed. Using potential energy surface scans, thermodynamically favorable reaction pathways are proposed. CH addition to the л-bonds in furan and 2-methylfuran rings was found to be the entrance channel that led to formation of all identified primary products. Both reactions follow patterns of H-loss and CHO-loss, as well as formation of cyclic and acyclic isomers.

*Corresponding author: gmeloni@usfca.edu

4.2 Introduction

The increasing greenhouse gas effect has been linked to ambient temperature increases, natural ozone layer destruction, and ecosystem disruptions, which could ultimately lead to a negative effect on human health and quality of life.[1,2] Carbon dioxide is the greatest contributor to greenhouse gases and is mainly released into the atmosphere through fossil fuel burning.[1,2] An important portion of fossil fuel consumption is their use as fuels.[1,2] Fossil fuel resources are diminishing, and incentives for bioenergy research are becoming more persuasive.[1–3] The desire for viable alternative fuels is vast, and reasons range from economic independence to remediation of the environment.[3] Recently, there has been more focus on immediate alternatives, such as carbon-based fuels, since they would allow for automotive infrastructure to remain in place.[3] An ideal fuel replacement would not only reduce greenhouse gas emissions but also be producible on a large scale through a photosynthetic process, which would serve as a sink for atmospheric CO2.[3] This model process has already been proven possible for ethanol and strengthens the interest in researching more and potentially better biofuels.[3,4]

Furan derivatives have become popular contenders to become an ideal gasoline replacement for spark-ignition engines.[5] Several studies have shown that furan derivatives have higher energy density, lower aromatic content, lower carbon dioxide and hydrocarbon emissions, and better knock resistance compared to current additives, without negatively effecting gasoline products.[5,6] Additionally, 2-methylfuran is less water-soluble than ethanol and has such a low potential for extraction into the water layer that the risk of water contamination is considered negligible.[5,7] Compared to current RON 95 gasoline, 2-methyl furan also has lower NOx and particulate matter emissions and better resistance to autoignition.[5,7] The Clean Air Act states that new fuels and fuel additives need to be fully compatible with commonly used vehicle fuel

systems and distribution equipment.[7] Engine studies of furan, dimethylfuran, and 2-methlyfuran have shown the compounds to have sufficiently similar combustion and emissions patterns as gasoline, meaning no major modifications to current automotive systems would be required.[5] Beyond requirements, furan derivatives have been successfully obtained through photosynthetic production from sugars and lignocellusoic biomass.[7] The process is better than that for ethanol because the fermentation step, which forms ethanol from glucose and emits carbon dioxide, would be avoided.[3] The omission would allow for all available carbon from cellulose to be utilized.[3] Due to its production, the combustion of biomass-derived fuels would be a carbon neutral process and could greatly improve current emissions trends.[3,4] Methylidene radical (CH) is one of the most important radicals involved in hydrocarbon combustion processes in the atmosphere.[8] Not only has the radical been found in combustion flames, it also greatly affects the energetics of gas-phase environments.[4,9] The CH radical is the most reactive carbon-containing neutral radical because it has one singly filled and one empty nonbonding molecular orbital localized on the carbon atom.[10,11] Therefore, reactions of CH radicals with unsaturated hydrocarbons are generally fast and barrierless.[10]

Reactions of carbon radicals with organic molecules and any resulting intermediates are important to know for biofuel combustion modeling.[10] By studying CH reactivity, reactions between more complex hydrocarbon radicals and potential biofuel compounds that would occur in combustion environments can be better predicted.[4] Previous studies with CH radical have been conducted to investigate general mechanisms with small organic compounds. These studies provide great insight into CH radical entrance channels and reaction products. In 2009, Goulay et al.[11] investigated the reactions of CH with several small unsaturated hydrocarbons at room temperature using tunable vacuum ultraviolet (VUV) photoionization. They found that the

primary entrance channel for all the compounds was cycloaddition to the π-bond systems followed by H- or H_2-loss.[11] Products were linear, and cyclic isomers and any intermediates rapidly dissociated.[11] Trevitt et al.[9] continued the study in 2013 with similar compounds, most notably propene, and confirmed the dominant entrance channel, as well as establishing the following pattern: $CH + C_xH_y \rightarrow C_{x+1}H_y + H$. Several similar studies of CH radical reactions, including simple aldehydes and ketones, have come to the same conclusion of an initial cyclic intermediate by addition to the π-bond system followed by H-loss.[4,10] The presented research is focused on the reactions of furan and 2-methylfuran with ground state methylidyne radical at 298 K and 4 Torr to provide further valuable information about fundamental biofuel combustion mechanisms. Reaction products are observed by multiplexed photoionization mass spectrometry using synchrotron radiation and identified using their photoionization spectra. Additionally, electronic structure calculations of the potential energy surface (PES) scans are used to investigate primary product species formation.

4.3 Experimental Section

Experiments were conducted at the Advanced Light Source (ALS) of Lawrence Berkeley National Laboratory at the Chemical Dynamics beamline. Multiplexed time- and energy-resolved mass spectrometry coupled with tunable synchrotron radiation was used to identify reaction species and products. The instrument has been previously described in detail elsewhere[12-15] and, therefore, only a succinct description will be provided here.

Furan (purity ≥99%, Sigma-Aldrich) and 2-methylfuran (purity > 98%, Sigma-Aldrich) vapors were individually purified via freeze-pump-thaw technique and diluted to 1% with helium gas.[13] Each compound reacted with CH ($X^2\Pi$) radicals in a 62 cm long heated slow-flow quartz reactor tube with an inner diameter of 1.05 cm. CH ($X^2\Pi$) radicals were generated by photolysis

of 1% bromoform and helium gas mixture with an unfocused 4 Hz-pulsed 248 nm excimer laser. Reactant gases flow into the reactor tube via calibrated mass flow controllers. Pressure was maintained by a Roots pump connected to the reaction cell by feedback controlled throttle valve. Along with the main reactants, an excess of helium gas and a small amount of nitrogen gas were added. Adding nitrogen (9.1×10^{15} molecules cm^{-3}) quenched any vibrationally excited CH ($X^2\Pi$) radicals formed when bromoform is photolyzed that may have been faster than the reaction.[10] In this work, a concentration of 3.9×10^{15} molecules cm^{-3} of furan and 2-methylfuran were each flowed to react with a concentration of 1.3×10^{16} molecules cm^{-3} of bromoform for two separate reactions at 298 K and 4 Torr. Previous studies by Goulay et al.[10] have used a formula developed by Romanzin et al.[16] to estimate the CH number density produced from bromoform. Romanzin et al[16] quantifies CH radicals produced by cavity ring-down spectroscopy, which has significantly lower laser fluences that impact the multiphoton dissociation necessary for CH radical production. Additionally, the formula only considers CH radicals formed from the main secondary photodissociation pathway of bromoform.[16]

Reaction species travelled through a 650 μm wide pinhole into a differentially vacuumed ionization region to be photoionized by tunable synchrotron radiation. The cations formed were accelerated, collimated, focused, and detected by a 50 kHz-pulsed orthogonal acceleration time-of-flight mass spectrometer. The current experimental conditions resulted in a mass resolution of approximately 1,600. Reaction time, mass-to-charge ratio, and ion intensity were collected simultaneously for a specific photon energy over a range of 8 to 11 eV at 0.025 eV increments. Also, the ALS photocurrent measured by a calibrated photodiode was used to background subtract and normalize the ion signal at each photon energy increment.

Experimental data was collected as a three-dimensional data block that was "sliced" into two-dimensional data (m/z vs. photon energy and m/z vs. reaction time) that are ultimately reduced to yield photoionization (PI) spectra and kinetic time plots.[17] PI spectra express ion intensity as a function of photon energy and are created by integrating the ion signal of a selected m/z over a specific time range. A range of 0-30 ms for furan and 0-20 ms for 2-methylfuran was chosen for the reactions studied here because it best reduced the presence of any possible signal due to secondary reactions. Reaction species were identified by a comparison of the experimental PI spectra to literature, calculated, or measured PI spectra. Adiabatic ionization energy (AIE) is obtained by linear extrapolation of the initial onset of PI spectra.[18] Due to photon energy step size, energy resolution, and possible hot bands, experimental AIE have an estimated uncertainty of 0.05 eV for species identified with an onset. By integrating ion intensity over the entire photon energy range, kinetic plots of the reactions were visualized. These plots show the relative amount of the reactant depleting and products forming over a certain time range. Primary products were identified by comparing the depletion of the reactant to the formation of the product. As shown in Figure 1, the time trace of the reactant is inversed and overlaid onto a time trace of a reaction species. Species with matching initial slopes are identified as primary products and those with differing slower slopes are categorized as secondary chemistry products.

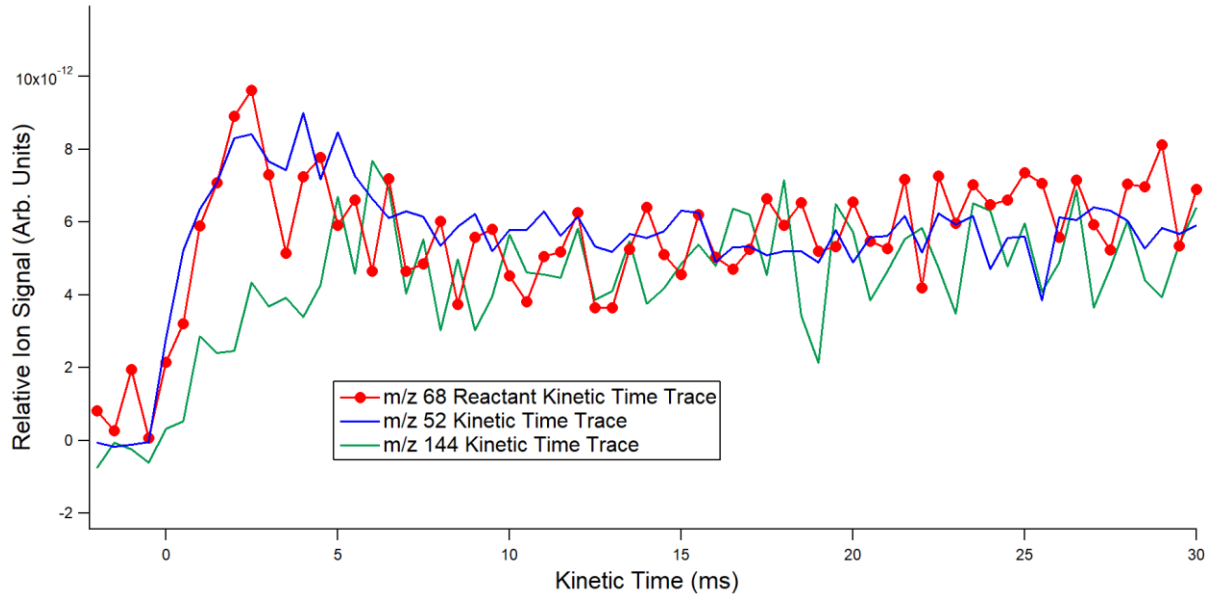

Figure 1. Kinetic time traces of a primary product at m/z 52 (blue line) and a secondary chemistry product at m/z 144 (green line) overlaid onto the kinetic time trace of the reactant furan (red line) at 298 K. The reactant time trace has been multiplied by −1 for comparison purposes.

Producing CH radicals has been problematic in previous combustion studies and similar issues were found here.[9-11] A bromoform ($CHBr_3$) photodissociation study at 248 nm using VUV ionization and photofragment translation spectroscopy found that C-Br bond fission is the primary dominant dissociation channel in the UV region.[19] The bond fission leads to $CHBr_2$ and Br radical formation.[19] CH radicals can only be produced through multiphoton dissociation using $CHBr_2$ and CHBr radicals as intermediates.[19] $CHBr_2$ can dissociate to form the desired CH radicals and Br_2.[19] However, there is a competing and prominent secondary photodissociation of $CHBr_2$ into CHBr and Br radicals.[19] In a possible tertiary dissociation, CHBr radicals formed from $CHBr_2$ radicals or directly from bromoform can break down into CH and Br radicals.[19]

All three photodissociation products are found in significant quantities in previous combustion studies and react with competitive kinetics, which could be problematic when calculating branching ratios.[9-11]

4.4 Computational Methods

Electronic structure calculations were carried out to help further identify and confirm products. All calculations in this study were performed with Gaussian 09 software program using the CBS-QB3 composite model, which has a mean absolute deviation of 4-5 kJ/mol or 0.05 eV.[12, 20-22] This composite model has high accurate energetics and can provide useful optimized molecular structural parameters.[21-22] AIE were calculated for all reactions species based on the difference between the corrected zero-point vibrational electronic energies of the ground state of the neutral and cation compounds. From the calculated total electronic energies of the neutral species, reaction enthalpy changes for the proposed mechanisms were derived to determine if the pathways were thermodynamically feasible.

Photoelectron (PE) spectra were simulated if reference spectra were unavailable using Franck-Condon (FC) and Franck-Condon-Herzberg-Teller (FCHT) methods in Gaussian 09.[23-25] The methods approximate FC factors of a molecule for the vibronic transition from the neutral to cationic state. Using a recursive formula developed by Ruhoff [26], the FC overlap integrals were also calculated. The resulting PE spectra were then integrated and expressed as calculated PI spectra to compare against experimental spectra for product identification.

Following product identification, proposed reaction pathway mechanisms were confirmed using relaxed potential energy surface (PES) scans. PES scans were carried out using B3LYP/6-31G(d) level of theory to determine transition states and minima.[27] The energies of these points were then calculated using the CBS-QB3 composite method followed by intrinsic reaction coordinate (IRC) calculations. IRC calculations are used to verify the forward and reverse reaction mechanisms based on the proposed transition states.

4.5 Results

As seen in previous studies, the dominant entrance channel found here in the two reactions is CH addition to the pi bond system of the furan and 2-methylfuran compounds.[4, 9-11] The initial formation of a bicyclic intermediate radical then yielded cyclic and acyclic products along with a loss of hydrogen or aldehyde (CHO) group. Heats of reactions were calculated and reported at 0 K.

In the studied photon energy range no dissociative ionization fragments from the absolute photoionization spectra of furan or 2-methylfuran were found, therefore, their dissociation did not interfere with the analysis. However, due to previously discussed issues regarding bromoform dissociation, a relatively large number of brominated species were observed. Brominated species are identifiable by comparison of the kinetic time traces of suspected species and $^{79}Br/^{81}Br$ isotopic ratio. The relative ion signal of the two suspected species should be matching when superimposed on each other at a ratio of ~ 1 to 1. Species observed in both reactions at m/z = 146/144, 142/140, 132/130, 106/104, 88/86, and 81/79 were determined to be brominated and are not further investigated in this work. Additionally, only in furan + CH ($X^2\Pi$) reaction species at m/z = 129/127 and 116/114 were also identified as brominated species.

4.5.1 Furan + CH ($X^2\Pi$) Product Identification

The kinetic time plot of a primary product must match the negative plot of the reactant, meaning the formation of product aligns with the depletion of the reactant over time. Primary products for furan + CH were found at m/z = 80 and 52. The time trace comparisons of the identified primary products with furan are shown in Figure 2.

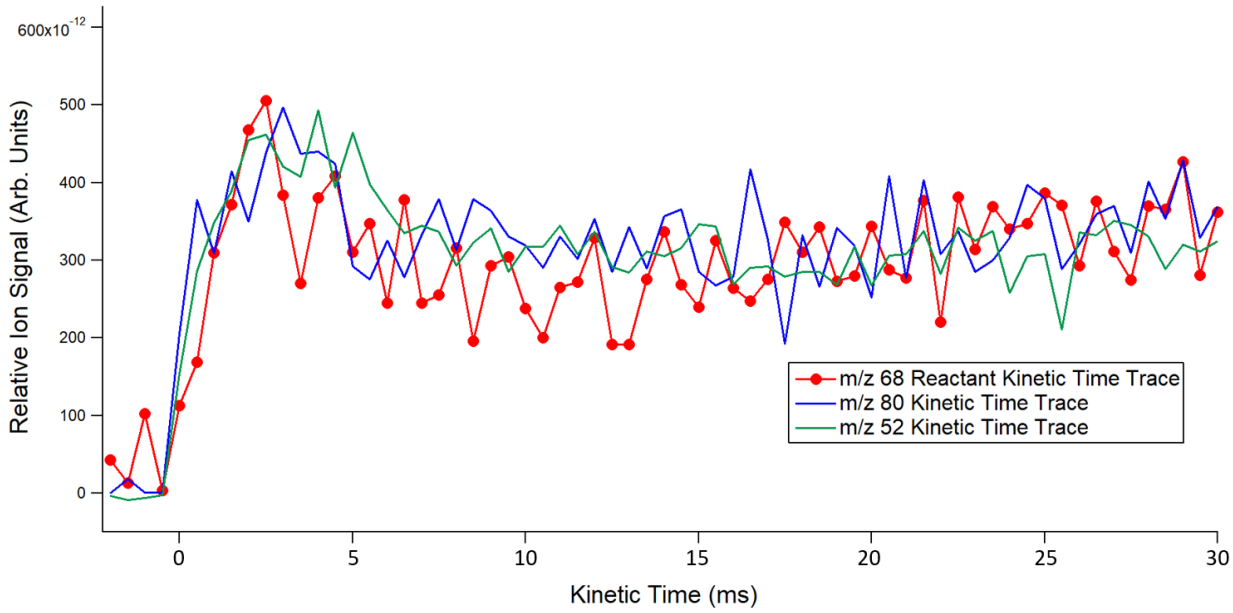

Figure 2. Kinetic time traces of primary products m/z 80 (blue line) and m/z 52 (green lines) overlaid onto the kinetic time trace of the reactant furan (red line) at 298 K. The reactant time trace has been multiplied by −1 for comparison purposes.

The primary products detected at m/z = 80 are shown in Figure 3 and supports the CH + C_xH_y → $C_{x+1}H_y$ + H pattern observed by Trevitt *et al.*[9] The experimental PI spectrum is in very good agreement with the summation of two C_5H_4O isomers. The literature PI spectra of 2,4-cyclopentadien-1-one, which is a cyclic compound, matches the onset and first part of the experimental curve with an AIE of 9.37 ± 0.05 eV.[28] To provide further confirmation, the CBS-QB3 AIE of 2,4-cyclopentadien-1-one was calculated to be 9.41 eV. The literature vertical IE for this species is 9.49 eV, which is higher than the calculated and experimental AIE, provides additional support for the characterization.[29] The second part of the experimental curve fits with the FC simulated PI spectrum of 2-penten-4-ynal, which has a calculated AIE of 9.95 eV and is a acyclic compound. At m/z = 80, the presence of these two compounds supports the trend of CH addition followed by H-loss as well as yielding both cyclic and acyclic isomers established by previous studies.[4, 9-11]

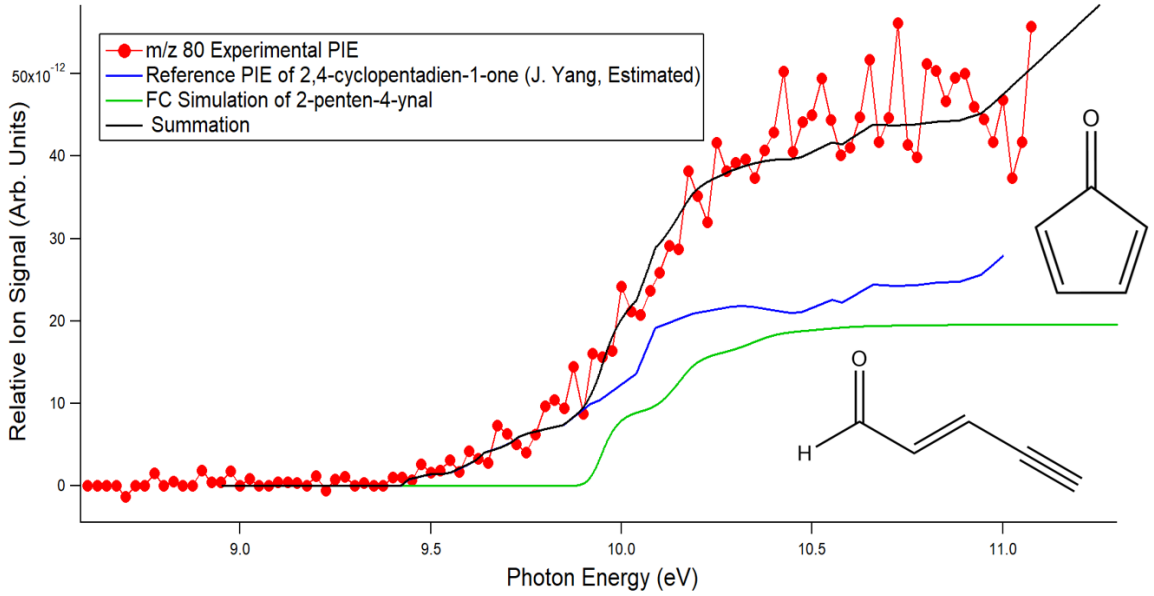

Figure 3. Summation (black line) of simulated PI spectrum of 2-penten-4-ynal (green line) and literature spectrum (blue line) of 2,4-cyclopentadien-1-one superimposed onto experimental data at m/z 80 (red line) for the reaction of furan + CH radical at 298 K.

Another primary product was observed at m/z = 52. The experimental PI curve shown in Figure 4 has an experimental onset of 9.53 ± 0.05 eV. A literature PI curve for vinylacetylene taken by T.A. Cool and coworkers[30] is found to be in very good agreement with the onset and first part of the experimental spectrum. The CBS-QB3 calculated AIE for vinylacetylene was calculated to be 9.58 eV and is within the experimental uncertainty. Vinylacetylene is an acyclic product and results from CH addition to furan followed by CHO-loss. The latter section of the experimental curve is believed to result from a fragment of a primary product at m/z = 80 resulting from decarboxylation. The thermochemical limits (no barrier for dissociation) for the appearance energies were calculated for neutral CO plus the possible cyclic and acyclic m/z = 52 fragment cations. From 2,4-cyclopentadien-1-one, cyclobutadiene cation + CO limit was calculated to be 10.75 eV. This value is a little too high to explain the signal of the m/z = 52 spectrum and, therefore, this fragment is not the one presumably causing the high energy signal.

The possible acyclic fragment from 2-penten-4-ynal used was 1-buten-3-yne cation and the thermochemical limit was calculated to be 9.62 eV, which could explain the increase in the ion signal for the latter section of the experimental m/z = 52 spectrum.

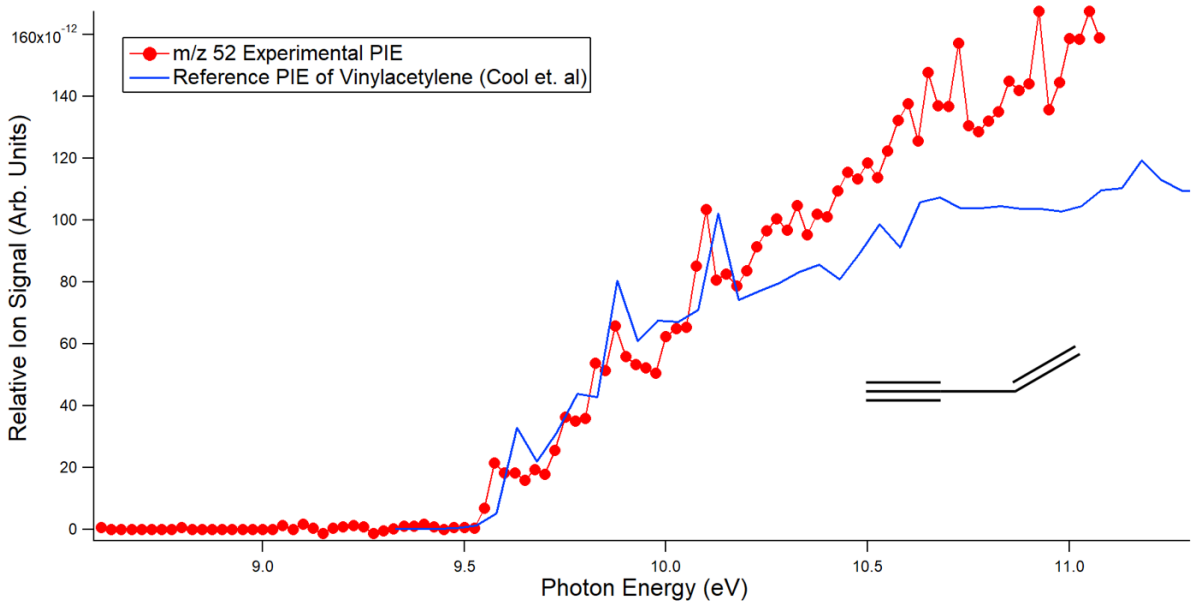

Figure 4. Literature PI spectrum of vinylacetylene (blue line) superimposed onto the experimental data at m/z 52 (red line) for the reaction of furan + CH radical at 298 K.

All intermediates, including the initial bicyclic radical, would be observed at m/z = 81 for the reaction of furan + CH. They will be described with the mechanism pathways later in this work. To account for signal resulting from bromine, the experimental curve at m/z = 79 was subtracted from the curve at m/z = 81 with respect to the $^{79}Br/^{81}Br$ isotopic ratio. The signal at m/z = 80 with respect to $^{12}C/^{13}C$ ratio was also subtracted from the experimental curve at m/z = 81. The remaining signal has a very low signal-to-noise ratio and is attributed to a combination of intermediates B, B3, and D2 (Scheme 1). These are the only intermediates with bound cations and ionization energies within the photon energy range.

4.5.2 2-Methylfuran + CH ($X^2\Pi$) Product Identification

At 298 K, the reaction between 2-methylfuran and CH yielded three primary m/z peaks. The time traces for the products and the 2-methylfuran reactant are compared in Figure 5. Comparison of the experimental PI spectrum at m/z = 94 and the summation curve of 2,4-cyclopentadien-1-carbaldehyde and 2,3,4-hexatrienal is shown in Figure 6. The two curves were found to be in very good agreement. No literature values were found for either compound, therefore, FC simulation spectra were computed along with CBS-QB3 calculated AIE. The simulated curve of 2,4-cyclopentadien-1-carbaldehyde with a calculated onset of 8.92 eV matches the first part of the experimental curve and onset of 8.93 ± 0.05 eV. The latter part of the curve is assigned to the 2,3,4-hexatrienal with a calculated onset of 9.07 eV. Following the established pattern CH + C_xH_y → $C_{x+1}H_y$ + H, the two compounds found at m/z = 94 are formed from CH addition followed by H-loss to yield cyclic and acyclic isomer products.[9]

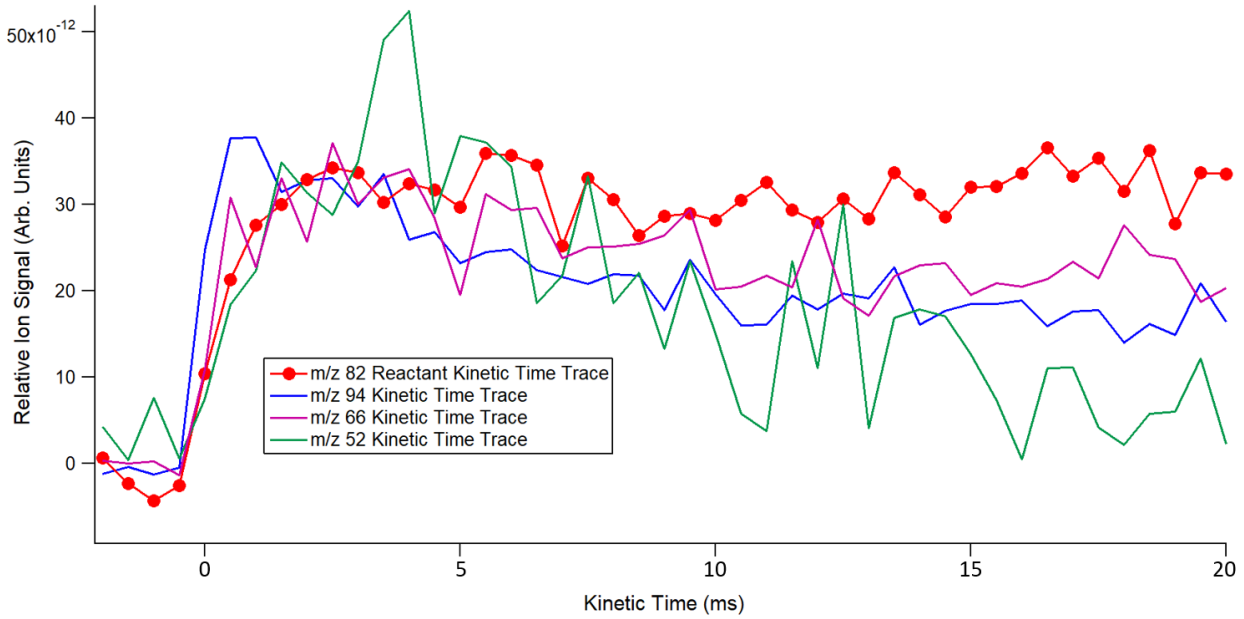

Figure 5. Kinetic time traces of primary products m/z 94 (blue line), m/z 66 (purple line), and m/z 52 (green line) overlaid onto the kinetic time trace of the reactant 2-methylfuran (red line) at 298 K. The reactant time trace has been multiplied by −1 for comparison purposes.

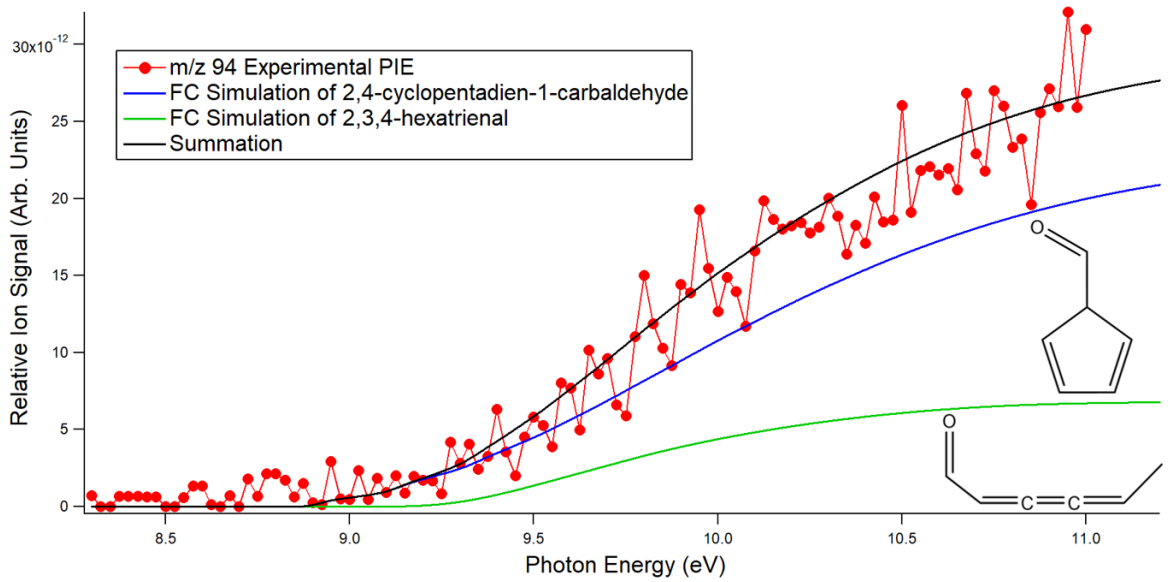

Figure 6. Summation (black line) of FC simulated PI spectra of 2,4-cyclopentadien-1-carbaldehyde (blue line) and 2,3,4-hextrienal (green line) superimposed onto the experimental data at m/z 94 (red line) for the reaction of 2-methlyfuran + CH radical at 298 K.

Signal observed at m/z = 66 was identified as a summation of 1,3-cyclopentadiene and 3-penten-1-yne (Z). In Figure 7, the onset of the experimental curve was observed at 8.52 ± 0.05 eV that matches the calculated value of 8.56 eV. A literature spectra of 1,3-cyclopentadiene (Hansen et al.[31]) is in very good agreement with both values. Since no literature PI or PE spectrum were found for 3-pent-1-yne (Z). a FC simulation spectrum was computed. The simulated curve is in very good agreement with the middle section of the experimental spectra. Similar to what is explained to occur at m/z = 52 for the furan + CH reaction, the latter part of this experimental curve is believed to result from a fragment of a primary product at m/z = 94 after a loss of CO. The thermochemical limit was calculated to be 8.61 eV for 1,3-cyclopentadiene cation + CO, which would dissociate from 2,4-cyclopentadiene-1-carbaldehyde. From 2,3,4-hexatrienal, 1,2,3-pentatriene cation + CO limit was calculated to be 8.78 eV. Both the calculated limits are below the observed increase of ion signal in the experimental m/z = 66

spectrum and are, therefore, consistent with the possibility that fragments are formed through decarboxylation of m/z = 94 products.

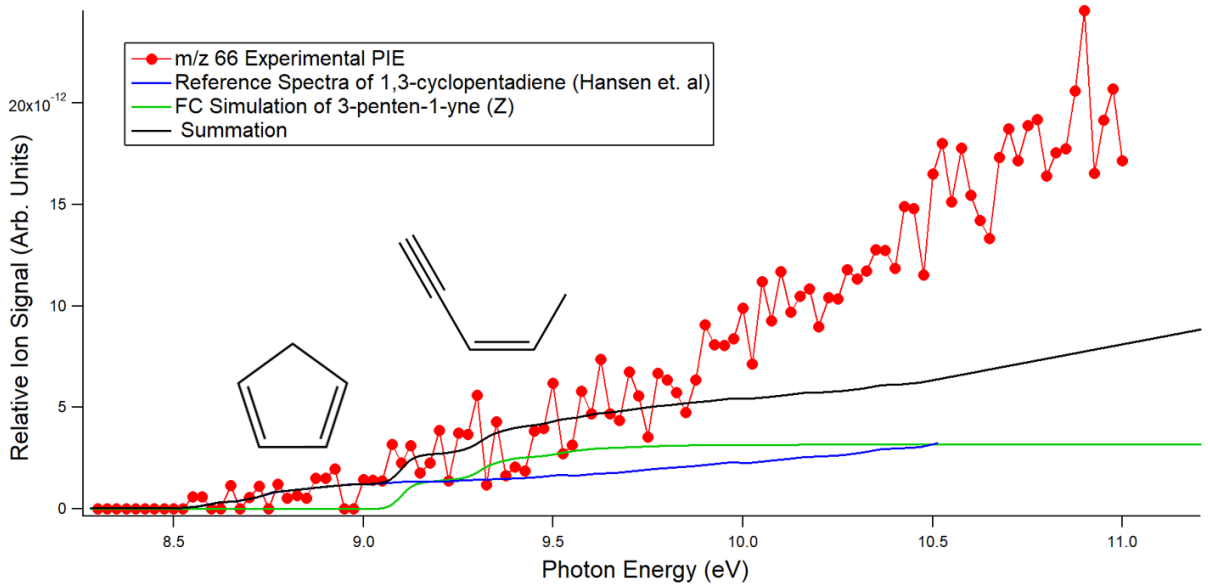

Figure 7. Summation (black line) of FC simulated PI spectrum of 3-penten-1-yne (Z) (green line) and literature PI spectrum of 1,3-cyclopentadiene (blue line) superimposed onto the experimental curve at m/z 66 (red line) for the reaction of 2-methlyfuran + CH radical at 298 K.

Similar to the furan + CH ($X^2\Pi$) reaction, a primary product is observed at m/z = 52. The literature PI curve of vinylacetylene was superimposed onto the experimental spectrum and they match very well (Figure 8).[30] The experimental PI spectrum has an onset of 9.53 ± 0.05 eV, in good agreement with the calculated AIE of 9.58 eV. The addition of CH followed by a loss of C_2H_3O resulted in vinylacetylene formation. The experimental PI spectrum at m/z = 43, which would represent the C_2H_3O fragment, has a low signal-to-noise ratio (Figure 9). The CBS-QB3 calculated AIE of 10.26 eV and FC simulation for CH_2CHO radical agreed with the experimental spectra. However, due to the low signal-to-noise ratio confident identification cannot be reached.

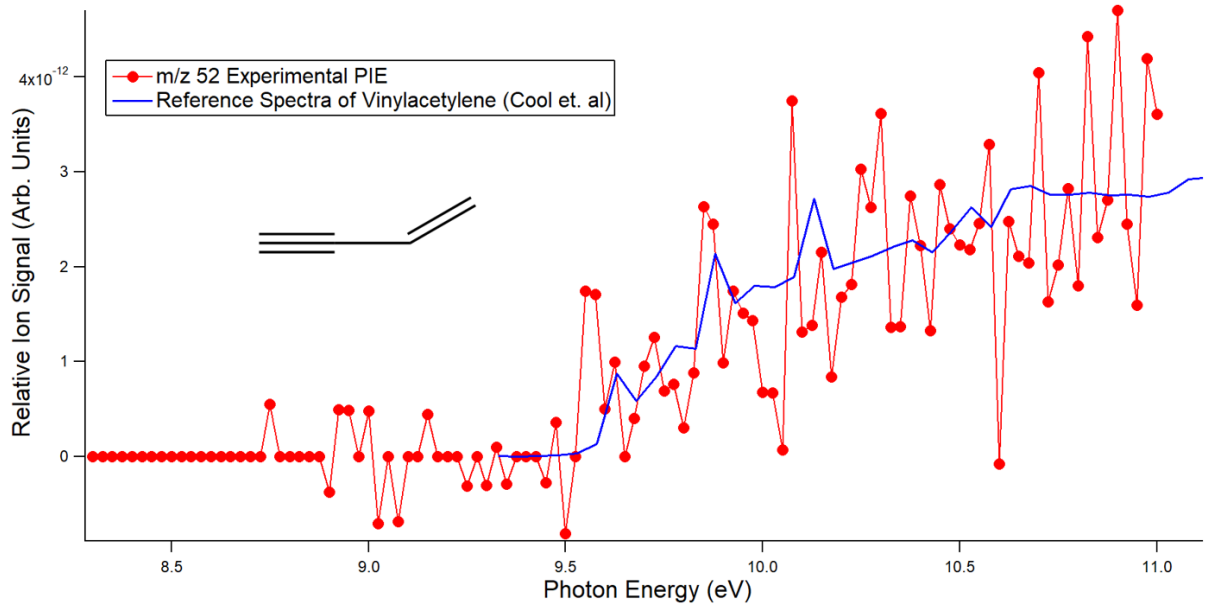

Figure 8. Comparison of experimental PIE at m/z 52 (red line) and literature PI spectra of vinylacetylene (blue line) for the reaction of 2-methylfuran + CH radical at 298 K.

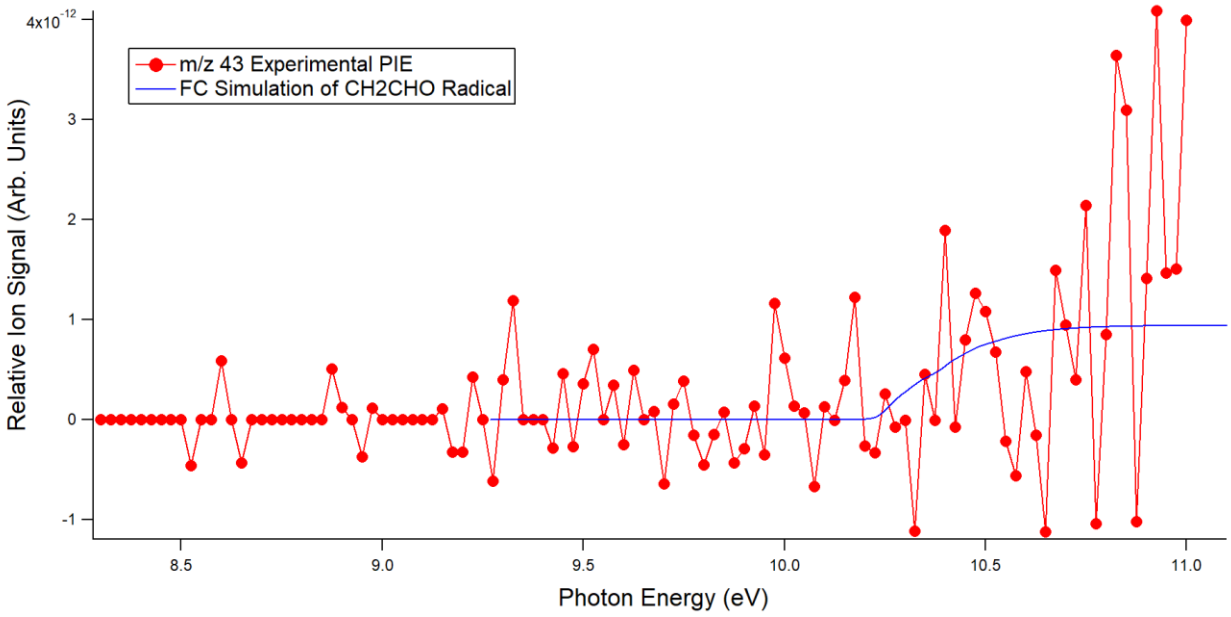

Figure 9. Comparison of experimental PIE at m/z 43 (red line) and FC simulated spectra of CH_2CHO radical (blue line) for the reaction of 2-methylfuran + CH radical at 298 K.

From mechanisms described later in this work, intermediates leading to all primary products for the 2-methylfuran + CH reaction would result in signal at m/z = 95, which is observed experimentally (Figure 10). Its corresponding kinetic time trace (Figure 11) identify these species deriving from primary chemistry with a decay proper of a radical species. After subtraction of the signal at m/z = 94 with respect to $^{12}C/^{13}C$ ratio, the remaining signal is attributed to a summation of the intermediates E and G from Scheme 1 and A1, C2, and C3 from Figures 14 and 15. Due to the large number of possible intermediates, the experimental curve cannot be confidently identified further to distinguish between intermediates.

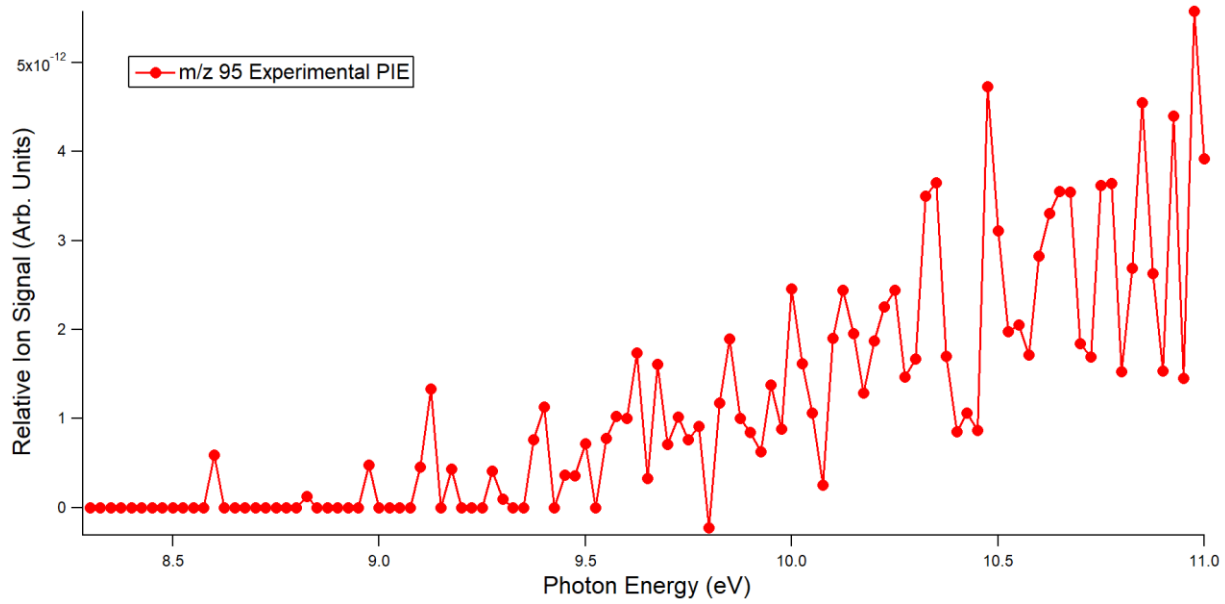

Figure 10. Experimental m/z 95 PI spectrum of the C_6H_7O intermediate isomers for the reaction of 2-methylfuran + CH radical at 298 K.

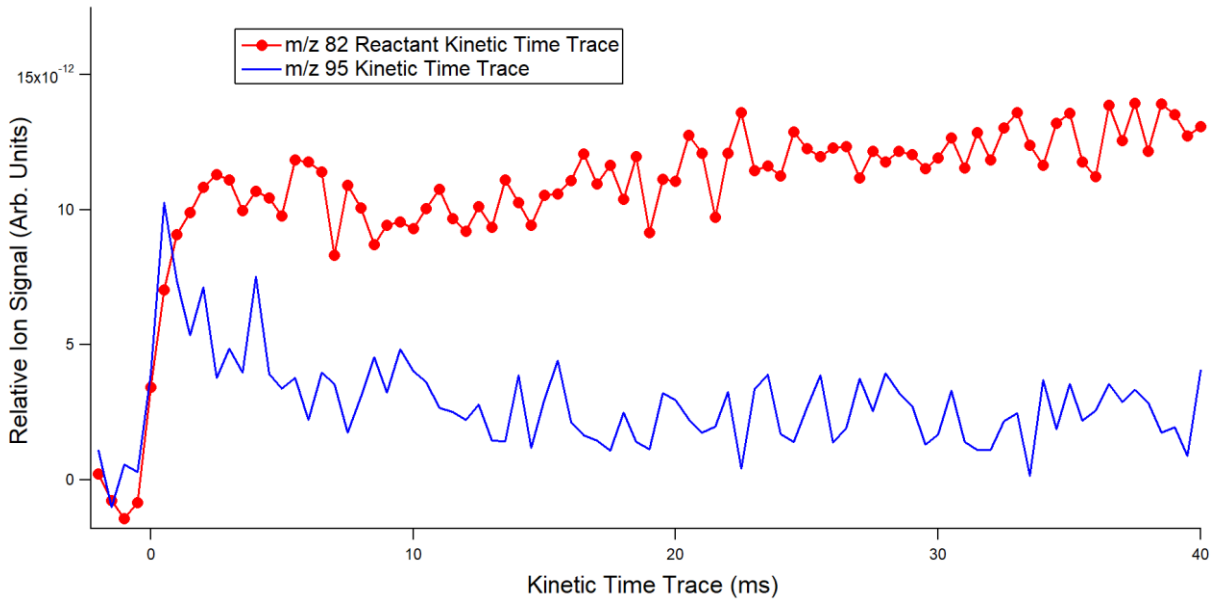

Figure 11. Kinetic time traces of intermediate species at m/z 95 (blue line) overlaid onto the kinetic time trace of the reactant 2-methylfuran (red line) at 298 K. The reactant time trace has been multiplied by −1 for comparison purposes.

4.5.3 Mechanism Pathways

There are two possible entrance channels for the CH ($X^2\Pi$) radical when reacting with furan or 2-methylfuran: CH insertion and addition. In this work, all primary products resulted from CH addition to the л-bond system in the furan and 2-methlyfuran rings. This pathway has a very low energy barrier and is exothermic. As previously mentioned, similar studies have observed the same dominant entrance channel. The energy calculated from the initial reactants optimized structures, furan + CH, is used as the zero reference point for the energetic calculations of the identified primary products and is shown in the energy diagrams at 0 kJ mol^{-1} by a red line. If reaction species or activation barriers are above the set reference point, they are considered thermodynamically and kinetically unfavorable. The same process is used to analyze 2-methylfuran + CH primary species.

The initial bicyclic intermediate radical (A and D) and resulting intermediates (B, C, E, F, and G) are presented in Scheme 1.

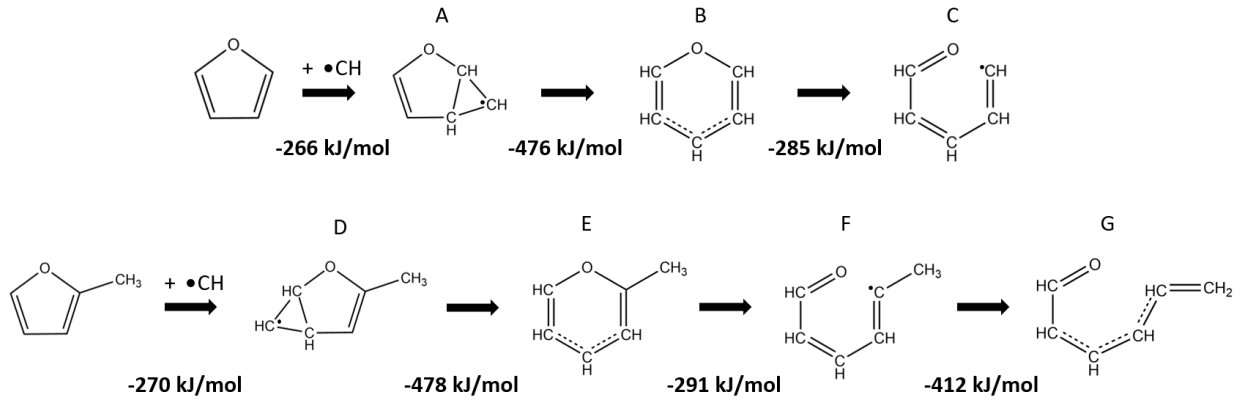

Scheme 1. Initial bicyclic intermediate (A and D) for CH addition to the л-bond systems in furan and 2-methylfuran reactions along with the following shared intermediates (B, C, E, F, and G) leading to final products.

The formation of the bicyclic intermediate radical (A) from furan + CH has a relatively small calculated activation barrier of 3 kJ/mol and a calculated enthalpy change of -266 kJ/mol. From the cleavage of C-C bond of the original л-bond, a six-membered ring (B) forms overcoming a transition state barrier of 13 kJ/mol with an exothermicity of 476 kJ/mol. With an activation barrier of 205 kJ/mol, ring opening with the breaking of the C and O bond results in an acyclic radical (C) with a reaction enthalpy of -285 kJ/mol. Similarly, for 2-methlyfuran + CH, the bicyclic intermediate radical (D) forms with an enthalpy change of -270 kJ/mol and overcomes a small calculated activation barrier of 3 kJ/mol. With a transition state barrier of 14 kJ/mol, the original C-C л-bond is cleaved forming a 6 membered-ring intermediate (E) that lies 478 kJ/mol below the reactants. The bond between the oxygen and α-carbon is cleaved causing the ring to open and form an acyclic intermediate radical (F). This formation overcomes an activation barrier of 200 kJ/mol and has a calculated heat of reaction of -291 kJ/mol. A hydrogen transfer from the ε-carbon to the δ-carbon in the acyclic intermediate F occurs to form the

intermediate G with a reaction enthalpy of -412 kJ/mol and activation barrier of 69 kJ/mol. Molecules C and G are the common intermediates from which the mechanism pathways diverge to form the primary products for the respective reactions observed in this investigation.

4.5.4 Furan + CH ($X^2\Pi$) Mechanisms

From intermediate radical (C), the three identified primary products for furan + CH reaction were formed from two pathways: H-loss and CHO-loss. Following two dihedral rotations and a hydrogen loss, 2-penten-4-ynal is exothermically formed. The dihedral rotations of intermediate radical (C) have activation barriers of 8 and 229 kJ/mol with reaction enthalpies of -304 kJ/mol and -307 kJ/mol, respectively. The rotated radical intermediates are shown in the energy diagram for furan + CH as A1 and A2 (Figure 12). A hydrogen was lost from intermediate A2 and 2-penten-4-ynal was formed by overcoming a transition state barrier of 165 kJ/mol. The H-loss and product formation is overall exothermic and the final calculated energy lies 164 kJ/mol below the zero reference point. A second isomer at m/z = 80 was also formed through a dihedral rotation, ring reformation, and H-loss shown in Figure 12. Intermediate radical (C) overcame a 10 kJ/mol activation barrier to rotate and formed intermediate B1 with a calculated energy 296 kJ/mol below the reactants. The aldehydic hydrogen was then transferred to the δ-carbon in the acyclic chain to form intermediate B2. The reaction enthalpy of the hydrogen transfer is -428 kJ/mol and has an activation barrier of 13 kJ/mol. The ring was reformed into a 5-membered ring intermediate (B3) by the bonding of the carbons involved in the hydrogen transfer, which lies 517 kJ/mol below the zero reference point. The activation barrier to create the bond is 28 kJ/mol. The ε-carbon loses one of its two bonded hydrogens to form the cyclic compound 2,4-cyclopentadien-1-one. Formation of the primary product is exothermic, lying below the zero reference point by 284 kJ/mol of energy, and has an activation

barrier of 233 kJ/mol. Overall, the formation of the two isomers from the H-loss channel are thermodynamically favorable and exothermic.

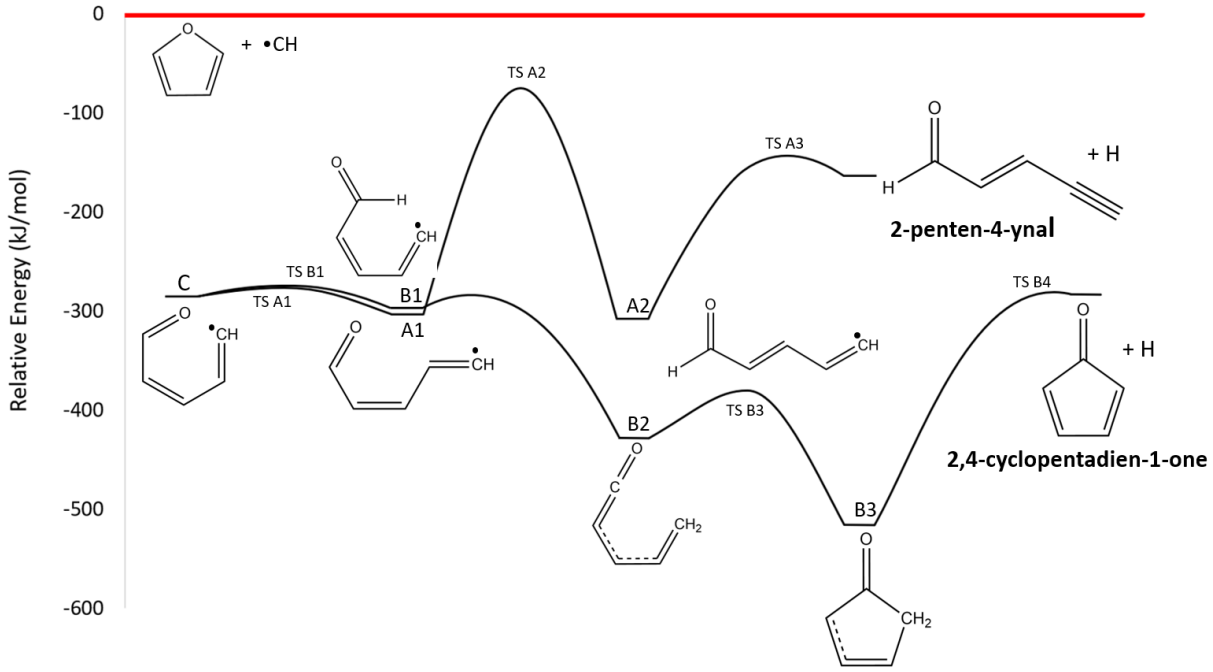

Figure 12. Potential energy surface diagram showing the formation of the primary products observed in the Furan + CH ($X^2\Pi$) reaction at m/z = 80. Reference zero point is shown by the red line.

Vinylacetylene is also formed from a radical intermediate (C) through two hydrogen transfers and a loss of an aldehyde group (CHO). The energy diagram (Figure 13) shows the energetics of the mechanism pathway. The γ-hydrogen in the acyclic chain of intermediate radical (C) is transferred to the δ-carbon to form Intermediate D1. The hydrogen transfer has a reaction enthalpy of -370 kJ/mol and a transition state barrier of 150 kJ/mol. A second hydrogen transfer of β-hydrogen to the γ-carbon formed intermediate D2 after overcoming an activation barrier of 226 kJ/mol. The transfer is overall exothermic with intermediate D2 at 349 kJ/mol of energy below the reactants. After a loss of the aldehyde group, vinylacetylene was formed with a heat of reaction of -227 kJ/mol and an activation barrier of 137 kJ/mol. The aldehyde group was not experimentally observed and may have immediately reacted with other radicals formed from

bromoform dissociation to form high mass species. All barriers and intermediates are below the reference point energy and therefore, kinetically and thermodynamically feasible.

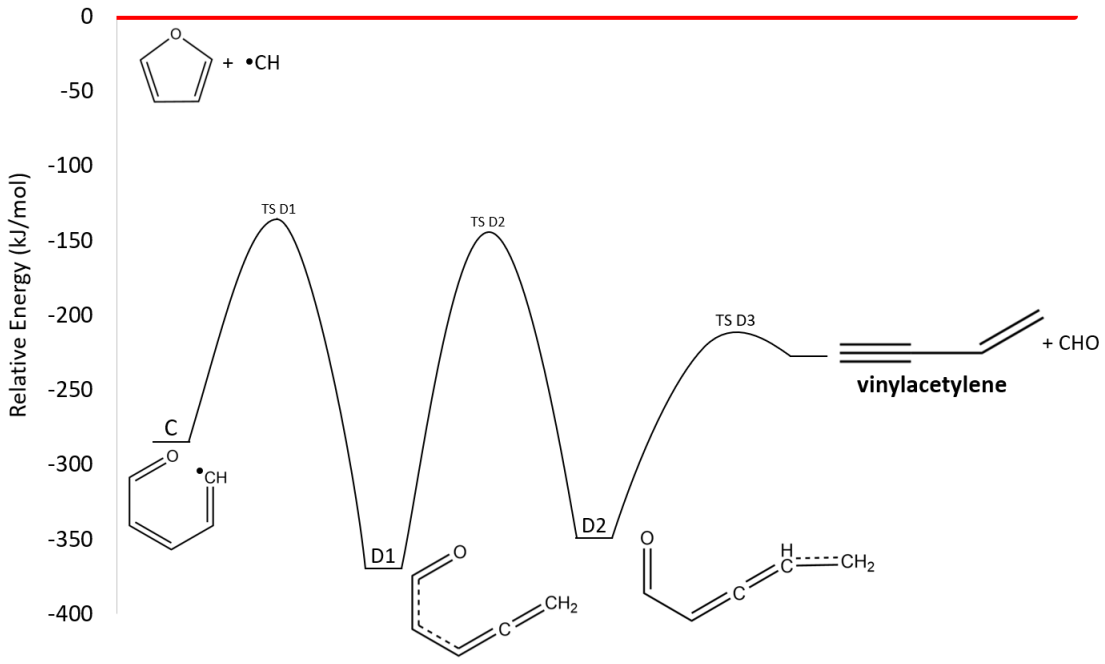

Figure 13. Potential energy surface diagram showing the formation of the primary products observed in the Furan + CH ($X^2\Pi$) reaction at m/z = 52. Reference zero point is shown by the red line.

4.5.5 2-Methylfuran + CH ($X^2\Pi$) Mechanisms

Four of the primary products identified from the 2-methylfuran + CH ($X^2\Pi$) reaction are formed from the same two mechanism pathways described above: H-loss and CHO-loss. All products, intermediates, and activation barriers are shown in the energy diagrams for the reaction (Figure 14 and 15). Energy calculations were all found to be below the reference point and thermodynamically and kinetically plausible. Products 2,4-cyclopentadiene-1-carbaldehyde and 1,3-cyclopentadiene are formed along the same pathway and diverge in the final step by having lost a hydrogen and an aldehyde group, respectively. Starting from intermediate G, ring reformation occurs by overcoming a barrier of 108 kJ/mol to bond the α-carbon and the ε-carbon in the chain. The formation of the five-membered ring intermediate (A1) was overall exothermic

and has a calculated energy that lies 444 kJ/mol below the reactants. With the loss of hydrogen from the δ-carbon in the ring, 2,4-cyclopentadien-1-carbaldehyde is formed. The calculated heat of reaction is -275 kJ/mol with a transition state barrier of 187 kJ/mol. Alternatively, intermediate A1 was also observed to lose the aldehyde functional group (CHO) to form 1,3-cyclopentadiene. The CBS-QB3 calculated reaction enthalpy for this formation is -333 kJ/mol and the activation barrier is 118 kJ/mol. These two cyclic products are each one of two isomers for their respective m/z ratios.

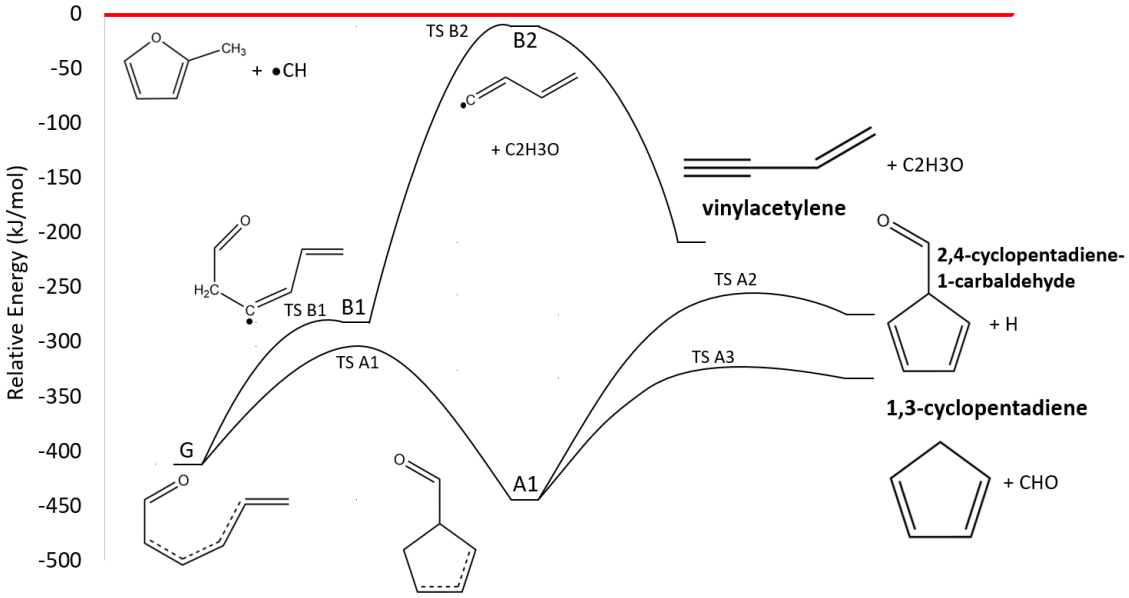

Figure 14. Potential energy surface diagram showing the formation of the primary products observed in the 2-methylfuran + CH ($X^2\Pi$) reaction for 1,3-cyclopentadiene, 2,4-cyclopentadiene-1-carbaldhyde, and vinylacetylene. Reference zero point is shown by the red line.

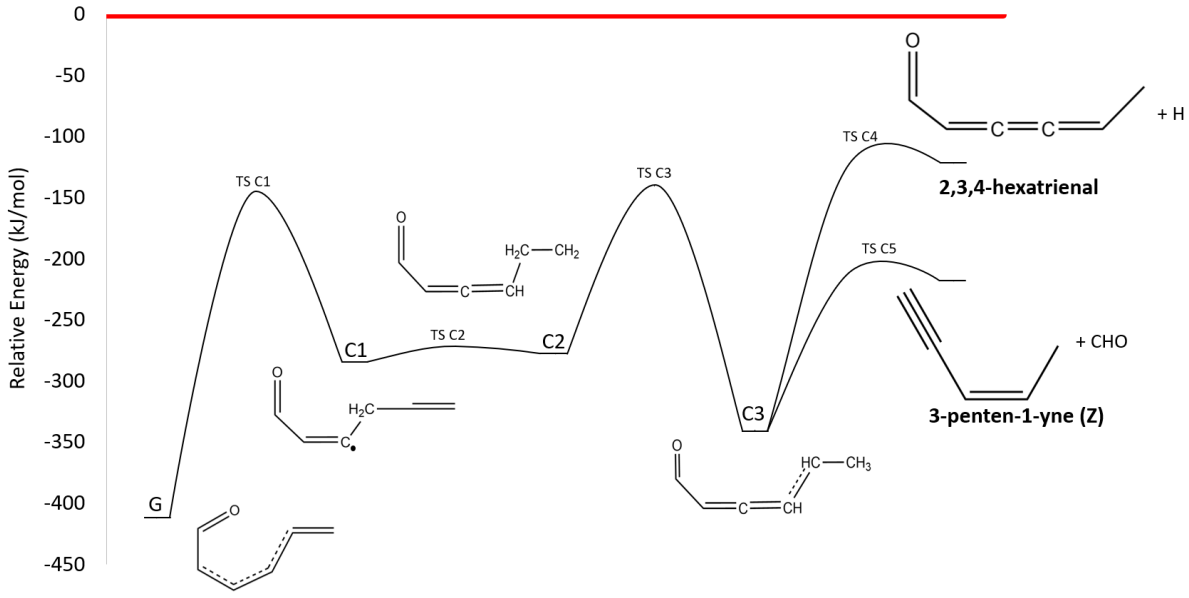

Figure 15. Potential energy surface diagram showing the formation of the primary products observed in the 2-methylfuran + CH ($X^2\Pi$) reaction for 2,3,4-hexatrienal and 3-penten-1-yne (Z). Reference zero point is shown by the red line.

Similarly, two acyclic products were also formed from a shared pathway that diverged by a loss of hydrogen or aldehyde group. The products are isomers with the cyclic products described above. Three sequential hydrogen transfers occurred before product formation with activation barriers of 284, 13, and 137 kJ/mol, respectively. The first hydrogen transfer occurred when the β-hydrogen on intermediate G moved to the γ-carbon to form intermediate C1, which lies 277 kJ/mol of energy below the zero reference point. Next, the γ-hydrogen was transferred to the δ-carbon in the acyclic chain forming intermediate C2. Intermediate C3 is formed from the final hydrogen transfer of the δ-hydrogen moving to the ε-carbon. The calculated enthalpy changes for the second and third hydrogen transfers are -340 and -121 kJ/mol, respectively. From intermediate C3, 2,3,4-hexatrienal and 3-penten-1-yne (Z) are formed. With a barrier of 234 kJ/mol, hydrogen was lost from the γ-carbon to form 2,3,4-hexatrienal, which has a heat of reaction of -121 kJ/mol. Instead of losing hydrogen, intermediate C3 is observed to also lose an

aldehyde group to form 3-penten-1-yne (Z). The calculated reaction enthalpy is -218 kJ/mol and the activation barrier is 136 kJ/mol.

The final primary product observed was vinylacetylene, which was also identified in the furan + CH reaction. However, the mechanism differs from the one that was previously described. From intermediate G, the β-hydrogen is transferred to the γ-carbon after overcoming an activation barrier of 268 kJ/mol. The hydrogen transfers to form intermediate B1 with a calculated energy at 284 kJ/mol below the reactants. Cleavage of the bond between the α-carbon and β-carbon in intermediate B1 occurred to form an intermediate radical (B2), along with the loss of C_2H_3O. The calculated enthalpy change for the bond cleavage is −12 kJ/mol, and the activation barrier is 270 kJ/mol. Vinylacetylene is formed from intermediate B2 in a barrierless, exothermic hydrogen transfer. The final calculated energy is below the zero reference point by 209 kJ/mol of energy. Radicals F and G2 formed from ring opening contain radicals within the acyclic chain due to the placement of the methyl group on 2-methylfuran. All radicals seen in furan + CH reaction intermediates contain radicals on the terminal carbon, which could explain why this mechanism pathway is not also observed in both reactions.

4.6 Conclusion

In this study, synchrotron radiation coupled with a multiplexed photoionization mass spectrometer at the Lawrence Berkeley National Laboratory was employed to study two reactions at 298 K: furan + CH ($X^2\Pi$) and 2-methylfuran + CH ($X^2\Pi$). Primary products were identified based on their kinetic time traces and photoionization spectra. The entrance channel observed was CH addition to the π-bonds in furan and 2- methylfuran rings, which yielded initial bicyclic intermediates. Both reactions have H-loss and CHO-loss pathways, along with formation of cyclic and acyclic isomers. The patterns and pathways seen in this study are in good

agreement with previous studies of CH ($X^2\Pi$) with unsaturated hydrocarbons. From furan + CH, 2,4-cyclopentadien-1-one, 2-penten-4-ynal, and vinylacetylene are observed through H-loss or CHO-loss pathways. Following H-loss and CHO-loss pathways, 2,4- cyclopentadiene-1-carbaldehyde, 2,3,4-hexatrienal, 1,3-cyclopentadiene, and 3-penten-1-yne (Z) were observed from 2- methylfuran + CH reaction. Vinylacetylene is also observed in the 2-methylfuran reaction as a primary product. Theoretical energetic calculations were performed at the CBS-QB3 level of theory to find the reaction mechanism pathways. All primary product pathways discussed were found to be thermodynamically and kinetically plausible.

4.7 Acknowledgements

This work is supported by the American Chemical Society – Petroleum Research Fund Grant # 56067-UR6 and the University of San Francisco via the Faculty Development Fund. The authors would also like to acknowledge Drs. Taatjes and Osborn from Sandia National Laboratories for the use of the experimental apparatus. The Advanced Light Source is supported by the Director, Office of Science, Office of Basic Energy Sciences, of the U.S. Department of Energy under Contract No. DE-AC02-05CH11231.

4.8 References

1. Klass, D. L., Chapter 1 - Energy Consumption, Reserves, Depletion, and Environmental Issues. In *Biomass for Renewable Energy, Fuels, and Chemicals*, Academic Press: San Diego, 1998; pp 1-27.

2. *Climate Change: Basic Information*; United States Environmental Protection Agency: Washington, DC, 2016.

3. Mascal, M.; Nikitin, E. B., Direct, high-yield conversion of cellulose into biofuel. *Angew. Chem., Int. Ed.* **2008,** *47* (41), 7924-7926.

4. Goulay, F.; Derakhshan, A.; Maher, E.; Trevitt, A. J.; Savee, J. D.; Scheer, A. M.; Osborn, D. L.; Taatjes, C. A., Formation of dimethylketene and methacrolein by reaction of the CH radical with acetone. *Phys. Chem. Chem. Phys.* **2013,** *15* (11), 4049-4058.

5. Eldeeb, M. A.; Akih-Kumgeh, B., Reactivity Trends in Furan and Alkyl Furan Combustion. *Energy Fuels* **2014,** *28* (10), 6618-6626.
6. Gouli, S.; Lois, E.; Stournas, S., Effects of Some Oxygenated Substitutes on Gasoline Properties, Spark Ignition Engine Performance, and Emissions. *Energy Fuels* **1998,** *12* (5), 918-924.
7. Christensen, E.; Yanowitz, J.; Ratcliff, M.; McCormick, R. L., Renewable Oxygenate Blending Effects on Gasoline Properties. *Energy Fuels* **2011,** *25* (10), 4723-4733.
8. Becker, K. H.; Engelhardt, B.; Wiesen, P.; Bayes, K. D., Rate constants for methylidyne (X2Π) reactions at low total pressures. *Chem. Phys. Lett.* **1989,** *154* (4), 342-8.
9. Trevitt, A. J.; Prendergast, M. B.; Goulay, F.; Savee, J. D.; Osborn, D. L.; Taatjes, C. A.; Leone, S. R., Product Branching Fractions of the CH + Propene Reaction from Synchrotron Photoionization Mass Spectrometry. *J. Phys. Chem. A* **2013,** *117* (30), 6450-6457.
10. Goulay, F.; Trevitt, A. J.; Savee, J. D.; Bouwman, J.; Osborn, D. L.; Taatjes, C. A.; Wilson, K. R.; Leone, S. R., Product detection of the CH radical reaction with acetaldehyde. *J Phys Chem A* **2012,** *116* (24), 6091-106.
11. Goulay, F.; Trevitt, A. J.; Meloni, G.; Selby, T. M.; Osborn, D. L.; Taatjes, C. A.; Vereecken, L.; Leone, S. R., Cyclic Versus Linear Isomers Produced by Reaction of the Methylidyne Radical (CH) with Small Unsaturated Hydrocarbons. *J. Am. Chem. Soc.* **2009,** *131* (3), 993-1005.
12. Winfough, M.; Yao, R.; Ng, M.; Catani, K.; Meloni, G., Synchrotron Photoionization Investigation of the Oxidation of Ethyl tert-Butyl Ether. *J. Phys. Chem. A* **2017,** *121* (7), 1460-1469.
13. Ng, M. Y.; Bryan, B. M.; Nelson, J.; Meloni, G., Study of tert-Amyl Methyl Ether Low Temperature Oxidation Using Synchrotron Photoionization Mass Spectrometry. *The Journal of Physical Chemistry A* **2015,** *119* (32), 8667-8682.
14. Ng, M. Y.; Nelson, J.; Taatjes, C. A.; Osborn, D. L.; Meloni, G., Synchrotron Photoionization Study of Mesitylene Oxidation Initiated by Reaction with Cl(2P) or O(3P) Radicals. *The Journal of Physical Chemistry A* **2014,** *118* (21), 3735-3748.
15. Ray, A. W.; Taatjes, C. A.; Welz, O.; Osborn, D. L.; Meloni, G., Synchrotron Photoionization Measurements of OH-Initiated Cyclohexene Oxidation: Ring-Preserving

Products in OH + Cyclohexene and Hydroxycyclohexyl + O2 Reactions. *J. Phys. Chem. A* **2012,** *116* (25), 6720-6730.
16. Romanzin, C.; Boye-Peronne, S.; Gauyacq, D.; Benilan, Y.; Gazeau, M. C.; Douin, S., CH radical production from 248 nm photolysis or discharge-jet dissociation of CHBr3 probed by cavity ring-down absorption spectroscopy. *J. Chem. Phys.* **2006,** *125* (11), 114312/1-114312/9.
17. Osborn, D. L.; Zou, P.; Johnsen, H.; Hayden, C. C.; Taatjes, C. A.; Knyazev, V. D.; North, S. W.; Peterka, D. S.; Ahmed, M.; Leone, S. R., The multiplexed chemical kinetic photoionization mass spectrometer: A new approach to isomer-resolved chemical kinetics. *Rev. Sci. Instrum.* **2008,** *79* (10, Pt. 1), 104103/1-104103/10.
18. Chupka, W. A.; Berkowitz, J., Photoionization of Ethane, Propane, and n-Butane with Mass Analysis. *The Journal of Chemical Physics* **1967,** *47* (8), 2921-2933.
19. Zou, P.; Shu, J.; Sears, T. J.; Hall, G. E.; North, S. W., Photodissociation of Bromoform at 248 nm: Single and Multiphoton Processes. *J. Phys. Chem. A* **2004,** *108* (9), 1482-1488.
20. M. J. Frisch, G. W. T., H. B. Schlegel, G. E. Scuseria, M. A. Robb, J. R. Cheeseman, G. Scalmani, V. Barone, G. A. Petersson, H. Nakatsuji, X. Li, M. Caricato, A. Marenich, J. Bloino, B. G. Janesko, R. Gomperts, B. Mennucci, H. P. Hratchian, J. V. Ortiz, A. F. Izmaylov, J. L. Sonnenberg, D. Williams-Young, F. Ding, F. Lipparini, F. Egidi, J. Goings, B. Peng, A. Petrone, T. Henderson, D. Ranasinghe, V. G. Zakrzewski, J. Gao, N. Rega, G. Zheng, W. Liang, M. Hada, M. Ehara, K. Toyota, R. Fukuda, J. Hasegawa, M. Ishida, T. Nakajima, Y. Honda, O. Kitao, H. Nakai, T. Vreven, K. Throssell, J. A. Montgomery, Jr., J. E. Peralta, F. Ogliaro, M. Bearpark, J. J. Heyd, E. Brothers, K. N. Kudin, V. N. Staroverov, T. Keith, R. Kobayashi, J. Normand, K. Raghavachari, A. Rendell, J. C. Burant, S. S. Iyengar, J. Tomasi, M. Cossi, J. M. Millam, M. Klene, C. Adamo, R. Cammi, J. W. Ochterski, R. L. Martin, K. Morokuma, O. Farkas, J. B. Foresman, and D. J. Fox *Gaussian 09*, Gaussian Inc.: Wallingford CT, 2009.
21. Montgomery, J. A., Jr.; Frisch, M. J.; Ochterski, J. W.; Petersson, G. A., A complete basis set model chemistry. VII. Use of the minimum population localization method. *J. Chem. Phys.* **2000,** *112* (15), 6532-6542.
22. Montgomery, J. A., Jr.; Frisch, M. J.; Ochterski, J. W.; Petersson, G. A., A complete basis set model chemistry. VI. Use of density functional geometries and frequencies. *J. Chem. Phys.* **1999,** *110* (6), 2822-2827.

23. Cool, T. A.; McIlroy, A.; Qi, F.; Westmoreland, P. R.; Poisson, L.; Peterka, D. S.; Ahmed, M., Photoionization mass spectrometer for studies of flame chemistry with a synchrotron light source. *Rev. Sci. Instrum.* **2005,** *76* (9), 094102/1-094102/7.
24. Sharp, T. E.; Rosenstock, H. M., Franck—Condon Factors for Polyatomic Molecules. *The Journal of Chemical Physics* **1964,** *41* (11), 3453-3463.
25. Santoro, F.; Lami, A.; Improta, R.; Barone, V., Effective method to compute vibrationally resolved optical spectra of large molecules at finite temperature in the gas phase and in solution. *J. Chem. Phys.* **2007,** *126* (18), 184102/1-184102/11.
26. Ruhoff, P. T., Recursion relations for multi-dimensional Franck-Condon overlap integrals. *Chemical Physics* **1994,** *186* (2), 355-374.
27. Tirado-Rives, J.; Jorgensen, W. L., Performance of B3LYP Density Functional Methods for a Large Set of Organic Molecules. *J. Chem. Theory Comput.* **2008,** *4* (2), 297-306.
28. Yang, J., 2,4-cyclopentadiene-1-one. 2011 ed.; Center for Advanced Combustion & Energy (CACE): 2011. http://flame.nsrl.ustc.edu.cn
29. Koenig, T.; Smith, M.; Snell, W., The helium(I) photoelectron spectrum of cyclopentadienone. *Journal of the American Chemical Society* **1977,** *99* (20), 6663-6667.
30. Cool, T. A.; Wang, J.; Nakajima, K.; Taatjes, C. A.; McLlroy, A., Photoionization cross sections for reaction intermediates in hydrocarbon combustion. *International Journal of Mass Spectrometry* **2005,** *247* (1), 18-27.
31. Hansen, N.; Klippenstein, S. J.; Miller, J. A.; Wang, J.; Cool, T. A.; Law, M. E.; Westmoreland, P. R.; Kasper, T.; Kohse-Höinghaus, K., Identification of C5Hx Isomers in Fuel-Rich Flames by Photoionization Mass Spectrometry and Electronic Structure Calculations. *The Journal of Physical Chemistry A* **2006,** *110* (13), 4376-4388.

Chapter 5: Study of Methylidyne Radical (CH and CD) Reaction with 2,5-Dimethylfuran Using Multiplexed Synchrotron Photoionization Mass Spectrometry‡

‡As published in the Journal of Physical Chemistry A, *122* (29), pg. 6118-6133 (2018)

Erica Carrasco[1] and Giovanni Meloni[2]*

[1]Department of Chemistry, University of San Francisco, San Francisco, CA USA

[2]Department of Physical and Chemical Sciences, Università degli Studi de L'Aquila, L'Aquila, Italy

5.1 Abstract

At 298 K the reactions of 2,5-dimethlyfuran + CH ($X^2\Pi$) and + CD radicals were investigated using synchrotron radiation coupled with multiplexed photoionization mass spectrometer at the Lawrence Berkeley National Laboratory. Reaction products were characterized based on their photoionization spectra and kinetic time traces. CBS-QB3 level of theory was used for all energy calculations and potential energy surface scans were used to determine thermodynamically favorable reaction mechanisms. The two entrance pathways observed in the reactions are CH insertion within the C-O bond and CH addition to the л-bond system. Both yield initial 6-membered ring radical intermediates. Primary products from the CH addition pathway were observed at m/z = 108, 66, and 42. The two C_7H_8O isomers at m/z = 108 formed are 1,2,4-heptatrien-6-one and 3-hepten-5-yne-2-one. At m/z = 66, the three C_5H_6 isomers observed are 1,3-cyclopentadiene, 3-penten-1-yne (E), and 1-pent-4-yne. Ketene (m/z = 42) is also observed. From CH insertion entrance channel, the three C_6H_8 isomers produced are 1,2,4-hexatriene (Z), 2-hexen-4-yne (E), and 1,3,4-hexatriene. Patterns of H-loss, CHO-loss, and CO-loss observed were also in agreement with trends observed in other similar studies. H-assisted isomerization pathways have been considered as well for the formation of m/z = 66, 80, and 108 isomers.

*Corresponding author: giovanni.meloni@univaq.it

5.2 Introduction

As fossil fuel sources continue to diminish, the need for a sustainable source of energy and fuel is rapidly increasing.[1] Carbon based fuels are promising as immediate alternatives, since they would allow for combustion engines in place to still be utilized.[2-3] More specifically, second generation biofuels are currently the most attractive option.[4] Unlike first generation biofuels, production of second generation biofuels would use sugars that cannot be consumed by humans as feed stock.[4-5] Therefore, fuels would not compete with food production.[4-5] In several studies, 2,5-dimethylfuran (DMF), along with other furanic compounds, has been proven to have a high yield, low cost synthesis process using several unconsumable sugars.[6-8] Roman-Leshkoy et al.[7] were able to selectively remove five oxygens from fructose to produce DMF with 5-hydroxymethylfuran (HMF) as an intermediate. Shortly after, Zhao et al.[8] produced a high yield of the HMF intermediate without the use of acid catalysts, which reduced production costs and allowed for glucose to serve as a feedstock as well. In 2008, cellulose was also successfully converted in to several furanic compounds, including DMF.[3]

Due to several chemical properties, many consider DMF a better contender for a future biofuel than ethanol.[1] When comparing mass production potential, DMF is advantageous over ethanol because it can avoid the fermentation step seen in ethanol synthesis, which emits carbon dioxide.[3] DMF is nearly 40% higher in energy density, meaning it has better fuel mileage for the same size fuel tank.[1, 6] Additionally, DMF is insoluble in water, which not only makes water contamination risk negligible, but it also allows for easier storage.[1, 9] The heat of vaporization for DMF is very similar to gasoline and is therefore able to overcome the cold start engine issues that arise when using ethanol.[6, 10] With a high boiling point and low volatility, DMF would be

easily transported and stored as a liquid.[1, 9] Currently, DMF and other furan derivatives are used as antiknock and octane improvers for gasoline.[1, 11] Ignition studies show that DMF has similar spray patterns and flame propagation as gasoline, which make it compatible with modern spark-ignition engines without any major modifications.[1, 6, 9-10] The U.S. Environmental Protection Agency and Clean Air Act require new fuels to submit data on the possible health impacts, as well as demonstrate compatibility with current vehicle and distribution systems.[2] DMF combustion studies have already proven fulfilment of the compatibility requirements, but further investigation of its combustion reactivity will be essential for its viability as a biofuel.[1] The known disadvantages associated with DMF combustion are toxic emissions of NOx, CO, harmful intermediates, and particulate matter.[1, 6] However, these values are very comparable, if not less, than those measured from gasoline and ethanol combustion.[1, 6] Therefore, DMF is still perceived as a very promising fuel alternative and the advantages are enough to drive further research into its reactivity by many scientists.[1]

Studying methylidene radical (CH) initiated combustion reactions is an essential starting point to understanding and predicting the reactivity of more complex hydrocarbons for biofuel combustion modeling in the future.[12-14] CH radical reactions are generally very fast and barrier-less due to the carbon atom having one singly filled and one empty nonbonding molecular orbital.[13, 15] Present in combustion flames, CH radical significantly affects the energetics of gas-phase environments.[12, 16] Several studies have come to agreeing conclusions about the primary entrance channel of the CH radical and pathway patterns.[12-13, 15-16] Reactions with simple alkenes have all determined CH radical addition to the π-bond as the dominant entrance channel with the formation of an initial cyclic intermediate.[12-13, 15-16] In 2009, Goulay et al.[13] studied the reaction of CH with several small alkenes and found a pattern of linear and cyclic isomers formed via H-

loss pathways. Trevitt et al.[16] investigated reactions of CH and CD radicals and several small hydrocarbons with similar experimental methods and was able to establish the pattern: CH+ $C_xH_y \rightarrow C_{x+1}H_y$ + H. Furthermore, studies focused on CH radical reactions with acetones and acetaldehyde have also followed these patterns.[12-13, 15]

Our previous investigation studied the reactions of furan and 2-methylfuran with CH radicals and also found CH addition entrance channel to be dominant along with patterns of H-loss and linear and cyclic isomer products.[17] The research presented in this work seeks to continue to provide valuable information about the reactivity of furanic biofuels and hydrocarbon radicals. Specifically, the reactions of 2,5-dimethylfuran with ground state CH and CD radicals at 298 K and 4 Torr are presented and discussed. Multiplexed photoionization mass spectrometry using synchrotron radiation is utilized to detect reaction species, which are identified and characterized by photoionization (PI) spectra and kinetic time plots. By studying the same reaction with CD radicals, further details about the formation mechanism for primary products can be confirmed based on the observed isotopologues. Primary product mechanisms are proposed using electronic structure calculations and potential energy surface (PES) scans.

5.3 Experimental Methods

Experiments were carried out using the Chemical Dynamics beamline at the Advanced Light Source (ALS) of Lawrence Berkeley National Laboratory. Reaction species were characterized using multiplexed time- and energy-resolved mass spectrometry coupled with tunable synchrotron radiation. Details of the instrumentation has been described in depth elsewhere.[18-21]

After purification through freeze-pump-thaw technique, resulting 2,5-dimethylfuran (purity ≥99%, Sigma-Aldrich) vapor was diluted to 1% with helium gas.[19] To produce

bromoform vapors, helium gas was flowed into a glass vessel containing liquid bromoform at 8℃ and 725 torr and bubbled through the liquid. From the bromoform vapors, CH ($X^2\prod$) radicals were generated by photolysis using an unfocused 4 Hz-pulsed 248 nm XeF excimer laser of a 1% bromoform/helium gas mixture. The same technique was used to generate CD radicals with a bromoform-d_1. Due to bromoform's multiple photodissociation products and pathways, quantifying CH radical production and calculating branching ratios is not feasible.[12, 17, 22-23] Our previous investigation has explained the problematic nature of bromoform dissociation in more detail.[17]

DMF and CH/CD ($X^2\prod$) radicals were flowed into a 62 cm long heated slow-flow quartz reactor with an inner diameter of 1.05 cm by calibrated mass flow controllers. A Roots pump maintains a desired pressure and is connected by a feedback controlled throttle valve to the reaction cell. Excess helium gas was also added to the reaction cell. A concentration of 3.9 x 10^{13} molecules cm^{-3} of DMF was reacted with a concentration of 2.3 × 10^{13} molecules cm^{-3} of bromoform. The same experimental methods were used to react DMF (3.9 x 10^{13} molecules cm^{-3}) with CD radicals using bromoform-d_1 at a concentration of 6.8 × 10^{13} molecules cm^{-3}. Nitrogen with a concentration of 9.1 x 10^{15} molecules cm^{-3} was also added to the reaction with CD radicals. Nitrogen is present to quench any vibrationally excited CH/CD ($X^2\prod$) radicals that were formed when bromoform was photolyzed and may have been faster than the reaction.[13] However, a study done by Trevitt et al.[16] found no experimental difference between PI spectra for reactions with and without N_2 addition. The purpose of the additional reaction with CD radicals is to provide further clarity on the reaction mechanisms. The deuterium from the CD radicals can be used to trace the movement of the original hydrogen from the CH radical reactant in the reaction with CH radicals. If the reactions have matching experimental PI spectra at the

same m/z ratios, then it can be concluded that the initial hydrogen added with the CH radical reactant is lost. However, if the spectra are not in agreement, then the original hydrogen is still present in the final product and a hydrogen from the 2,5-dimethylfuran reactant was lost instead. After each reaction occurred, the reaction species flowed from the reaction cell to a differentially vacuumed ionization region through a 650 μm wide pinhole. Reaction species were then photoionized by tunable synchrotron radiation and the resulting cations were accelerated through a 50 kHz-pulsed orthogonal acceleration time-of-flight mass spectrometer for detection. A mass resolution of approximately 1,600 was used in this study. A calibrated photodiode was also employed to measure the photocurrent of the ALS to be used for background subtraction and normalization of the ion signal.

Reaction time, ion intensity, and mass-to-charge ratio were recorded simultaneously over the photon range of 8 to 11 eV at 0.025 eV increments. The resulting three-dimensional data block was "sliced" and reduced to two two-dimensional data images to represent m/z ratio vs. photon energy and m/z ratio vs. reaction time.[24] At specific m/z ratios, the ion intensity from the m/z ratio vs. reaction time image is integrated over the entire photon range and results in kinetic time plots. Varyingly, integration of ion intensity over a specific time range for the m/z ratio vs. photon energy image yields a PI spectrum. To reduce any possible signal from secondary reactions, a time range of 0-30 ms was used in this study. Using time plots and PI spectra, reaction species at specific mass-to-charge ratios can be characterized and identified. Kinetic time plots show the progress of the reaction species depleting or forming over the selected reaction time. To characterize a reaction species as a primary product the kinetic time plot of the reactant is inversed and overlaid onto the kinetic time plot of the proposed species. If curves have initial onsets that are in good agreement, the reaction species is considered a primary

product, since it will be forming at the rate that the reactant initially depletes. PI spectra curves are unique to individual compounds due to differing Frank-Condon (FC) factors, which allows spectra to be distinguishable between multiple isomers. Reactions species can therefore be confidently identified by comparing experimental PI spectra to literature or calculated photoionization plots. Adiabatic ionization energy (AIE) derived from PI spectra through linear extrapolation can also aid in product identification.[25] For experimental AIE, an estimated uncertainty of 0.05 eV is present for reaction species identified with an onset due to photon energy step size, energy resolution, and possible hot bands.

5.4 Computational Methods

The goal of this study is to identify all primary products and propose thermodynamically feasible mechanisms for their formation. Electronic structure calculations are used to compute AIE, simulate PI spectra, and perform potential energy scans to investigate the reaction mechanisms. Using Gaussian 09 software program with CBS-QB3 composite model, all electronic structure calculations were performed.[18, 26-28] The composite model has highly accurate energetics with an absolute deviation of 4-5 kJ/mol.[26-27] It also provides reliable optimized molecular structural parameters such as bond angles, bond lengths, and vibrational frequencies.[20] If the AIE of a species is not available in the literature, it can be calculated using the formula below:

$$AIE = E_{0,\,cation} - E_{0,\,neutral}$$

where E_0 represents the zero-point energy corrected total electronic energy. Heat of reactions are also determined using the corrected total electronic energies of the neutral states of the proposed products and starting reactants to confirm that product formation is thermodynamically feasible.

Reference spectra were always used if available for product identification. However, if no reference spectra were found, photoelectron (PE) spectra were simulated using Gaussian 09 for the proposed reaction species. Franck-Condon (FC) and Franck-Condon-Herzberg-Teller methods are used to approximate FC factors based on the vibronic transition from the neutral to the cationic state.[29-31] FC overlap integrals are also calculated using a recursive formula developed by Ruhoff.[32] Following integration, PE spectra are expressed as calculated PI spectra for comparison to experimental spectra.

After all products were identified based on agreeing PI spectra and AIE, reaction mechanisms for each primary product were determined. Proposed mechanism pathways were confirmed with relaxed PES scans using B3LYP/6-31G(d) level of theory.[33] The energies of all transition states and minima determined in the PES scans were recalculated using the CBS-QB3 composite method and verified for thermodynamic feasibility. Intrinsic reaction coordinate (IRC) calculations were also completed to further confirm the forward and reverse pathways, local minima, and saddle points based on the proposed transition state.

5.5 Results

The two entrance channels for the CH ($X^2\Pi$) radical found here were CH addition to the π bond system and CH insertion into the C-O bond within the ring in the 2,5-dimethylfuran compound. As seen in previous studies, the dominant entrance channel is the prior and yields a majority of the identified primary products.[12-13, 16-17] All reaction enthalpies calculated and reported in this work are at 0 K.

The dissociation of bromoform produced a significant number of brominated species, which were identified and found to not interfere with product analysis. Based on the $^{79}Br/^{81}Br$ isotopic ratio, suspected brominated species were characterized by overlaying their

photoionization spectra and kinetic time traces. If the relative ion signals of the plots are in good agreement at a ~1 to 1 ratio, then the species were considered brominated. In both reactions, species observed at m/z = 144/146, 130/132, 116/118, 104/106, and 79/81 were identified as brominated and, therefore, no longer investigated in this study.

5.5.1 Product Identification

The primary products for the reaction of 2,5-dimethylfuran + CH and + CD at 298 K were observed at m/z = 108, 80, 66, and 42. The formation of a product must match the depletion of the reactant over time to be considered as primary, meaning the product's kinetic time trace is in good agreement with the negative plot of the reactant. Figure 1 and 2 show the kinetic plot comparisons for DMF + CH and + CD, respectively, for the four primary products. A species at m/z = 52 is also observed and forming as fast as DMF is depleting but based on our computation of the potential energy surface this species cannot be a primary product because the energetics are not favorable (see Mechanism Pathways section). Products found at m/z = 108, 66, and 42 are believed to result from a CH addition entrance channel, while the products identified at m/z = 80 are proposed to result from a CH insertion pathway.

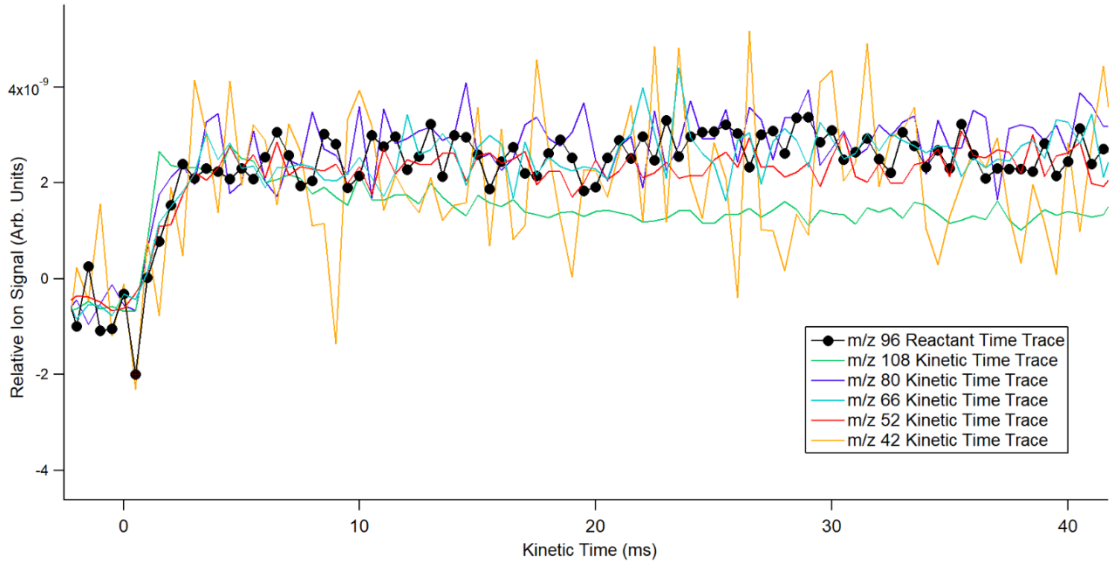

Figure 1. Kinetic time traces of primary products of 2,5-DMF + CH radical at 298 K. Time traces of m/z = 108 (green line), m/z = 80 (blue line), m/z = 66 (teal line), m/z = 52 (red line) and m/z = 42 (orange line) overlaid onto the kinetic time trace of the reactant 2,5-dimethylfuran (black line). The reactant time trace has been multiplied by −1 for comparison purposes.

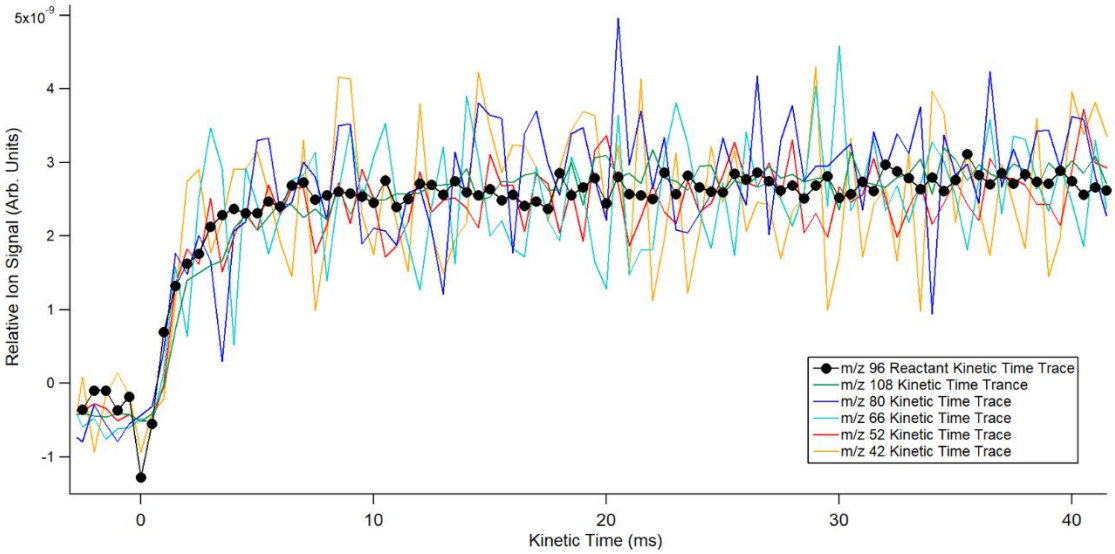

Figure 2. Kinetic time traces of primary products of 2,5-DMF + CD radical at 298 K. Time traces of m/z = 108 (green line), m/z = 80 (blue line), m/z = 66 (teal line), m/z = 52 (red line) and m/z = 42 (orange line) overlaid onto the kinetic time trace of the reactant 2,5-dimethylfuran (black line). The reactant time trace has been multiplied by −1 for comparison purposes.

Experimental PI spectrum observed at m/z = 108 was found in very good agreement with a summation of two acyclic C_7H_8O isomers (Figure 3). Due to the absence of literature values,

FC simulated curves for the products were calculated. The onset of the experimental curve was observed at 8.78 ± 0.05 eV and matches with the FC simulated spectra of 3,5,6-heptatrien-2-one. The CBS-QB3 calculated AIE for this isomer is 8.81 eV, which provides further product confirmation. The latter section of the experimental curve was found in a very good agreement with the simulated curve for 3-hepten-5-yne-2-one, which has a calculated AIE of 9.34 eV. The formation of C_7H_8O isomers indicates a H-loss mechanism and follows the $CH + C_xH_y \rightarrow C_{x+1}H_y + H$ pattern first discussed by Trevitt et al.[16]

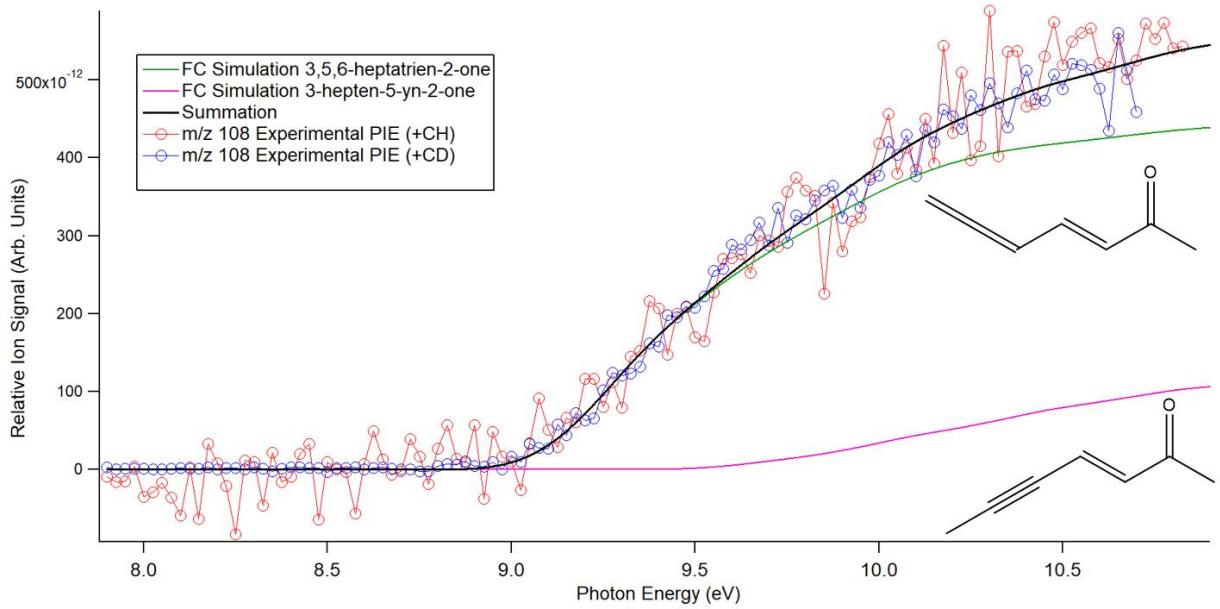

Figure 3. Summation (black line) of FC simulated spectra of 3,5,6-heptatrien-2-one (green line) and 3-hepten-5-yne-2-one (pink line) overlaid onto the experimental data for DMF + CH radical (red line) and DMF + CD radical (blue line) at m/z = 108 taken at 298 K.

At m/z = 66, the signal observed was determined to be a summation of three C_5H_6 isomers. The products yielded were cyclic and acyclic isomers, which was a trend also seen in similar studies with CH radicals and unsaturated hydrocarbons.[15-16] The experimental PI curve shown in Figure 4 has an onset of 8.55 ± 0.05 eV and is in good agreement with the literature PI curve for 1,3-cyclopentadiene measured by Taatjes et al.[34] Additionally, the literature AIE of 8.57 ± 0.05 eV is within the experimental uncertainty and supported by the CBS-QB3 calculated

AIE of 8.56 eV.[34] The middle section of the experimental spectra matches a literature PI spectrum of 3-penten-1-yne (E), which has an AIE of 9.05 eV.[35] The calculated AIE for 3-penten-1-yne is 9.10 eV. The third C_5H_6 isomer, which matches the final section of the experimental curve, was identified as 1-pent-4-yne using a literature curve taken by Hansen et al. and the reported AIE was 9.92 eV ± 0.05 eV.[35] To provide further confirmation, the AIE was calculated and found to be 9.93 eV. The proposed mechanism to form these products will be discussed later in this work and is believed to form congruently with the primary product observed m/z = 42.

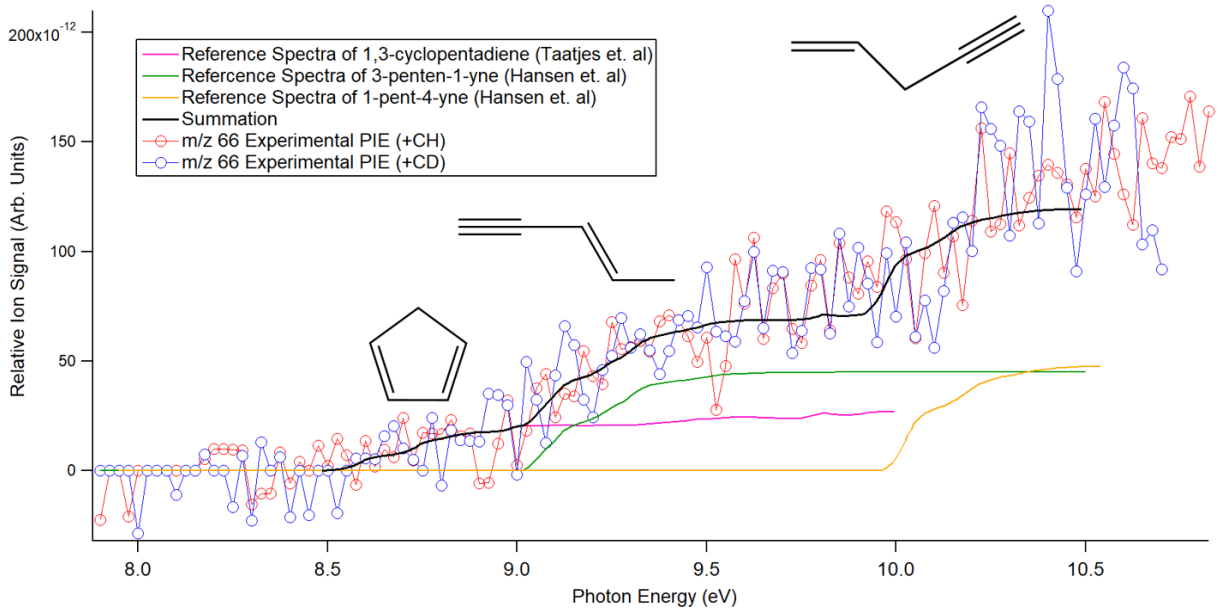

Figure 4. Summation (black line) of literature PI spectra for 1,3-cyclopentadiene (pink line), 3-penten-1-yne (green line), and 1-pent-4-yne (orange line) overlaid onto the experimental data for DMF + CH radical (red line) and DMF + CD radical (blue line) at m/z = 66. Experimental spectra were measured at 298 K.

A literature spectrum of ketene taken by Yang and coworkers[36] was overlaid onto the experimental curves at m/z = 42 and determined to be in very good agreement (Figure 5). The literature AIE of 9.62 eV, with an overall uncertainty of 20%, is within the uncertainty of the experimental AIE measured at 9.59 ± 0.05 eV.[36] Furthermore, the CBS-QB3 calculated AIE is

9.62 eV and matches very well both values. Ketene is an acyclic alkene product that is believed to form along the same mechanism pathway as the three C_5H_6 isomers describe above.

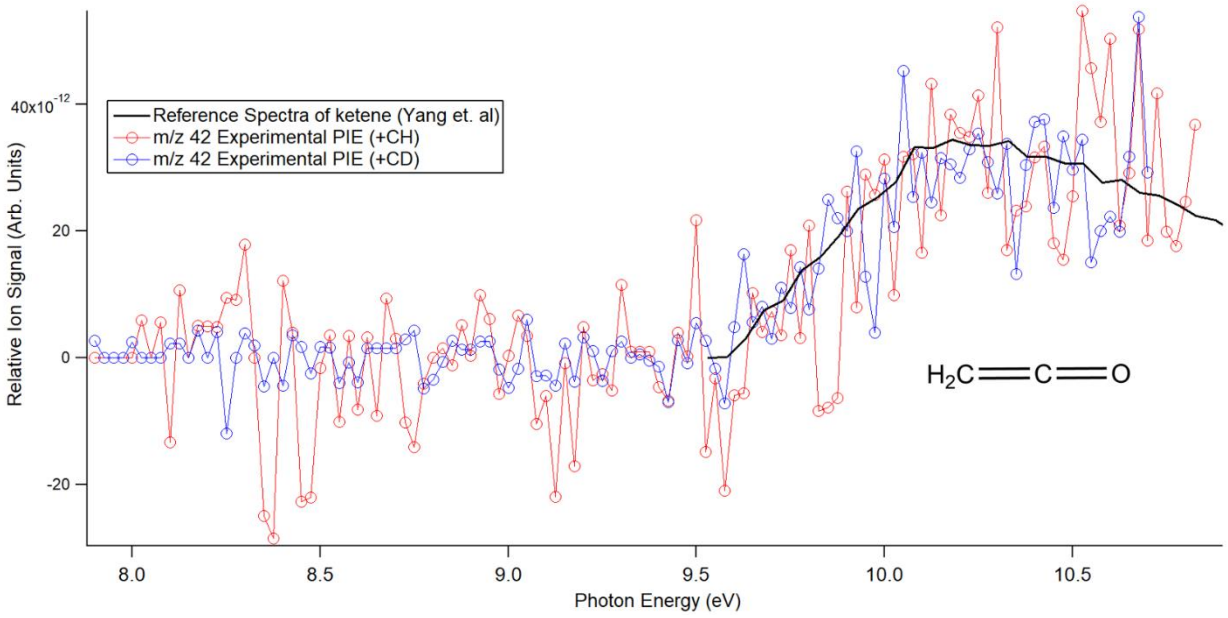

Figure 5. Literature PI spectrum of ketene (black line) overlaid onto the experimental data at m/z = 42 for DMF + CH radical (red line) and DMF + CD radical (blue line) measured at 298 K.

Signal observed at m/z = 52 is in very good agreement with the literature PI curve for vinylacetylene.[37] The AIE of the experimental spectrum shown in Figure 6 is 9.53 ± 0.05 eV matching the literature AIE of 9.58 eV ± 0.05 eV. Providing further validation, the calculated AIE is 9.58 eV as well. Vinylacetylene is formed from CH addition to the π bond system and would yield a C_3H_4O fragment that optimizes to cyclopropanone as well. However, the cation of cyclopropanone is unbound and, therefore, no signal is observed at m/z = 56. Due to the high transition barrier (see Mechanism Pathways section) necessary for explaining its formation, this species is regarded as a secondary product.

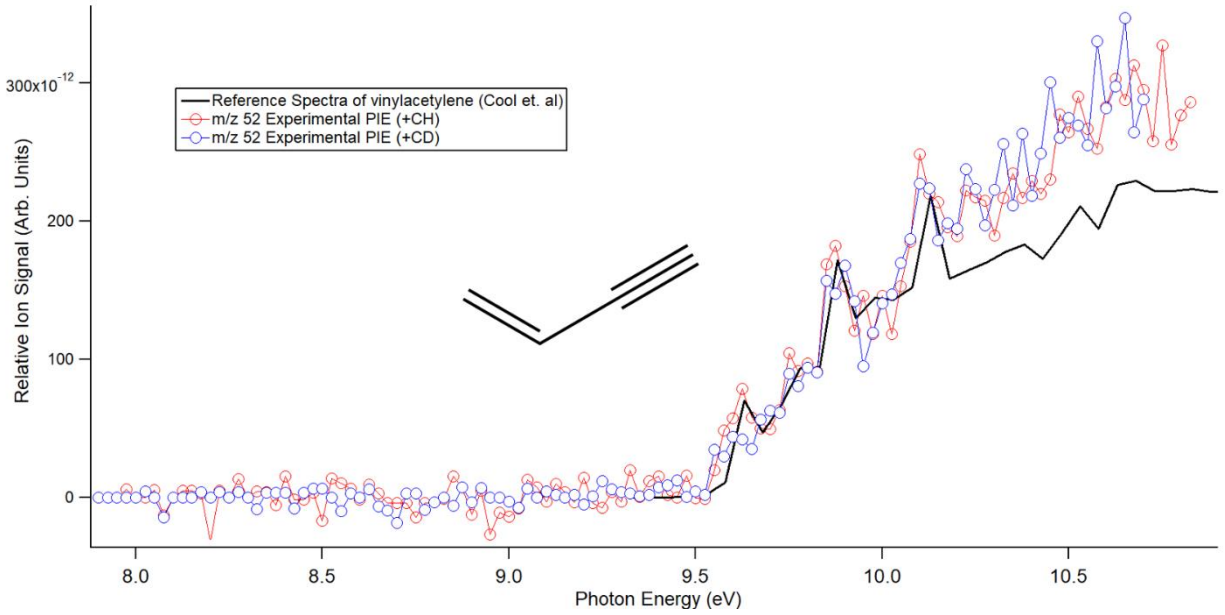

Figure 6. Literature PI spectrum of vinylacetylene (black line) superimposed onto the experimental curves at m/z = 52 for DMF + CH radical (red line) and DMF + CD radical (blue line) measured at 298 K.

The primary products identified at m/z = 80 are proposed to result from the insertion of CH radical into the C-O bond within the 2,5-dimethlyfuran ring followed by loss of a CHO fragment. Unlike the previously described experimental spectra, the spectra at the same m/z ratio shown in Figure 7 and 8 for the two reactions do not match. For the reaction of DMF + CH, the experimental spectrum shown in Figure 7 is in good agreement with a summation of three C_6H_8 isomers and has an onset of 8.35 ± 0.05 eV. Due to the absence of literature PI or PE spectra, FC simulation calculations were completed for the three proposed products. The onset of the experimental curve is in good agreement with the simulated spectra for 1,2,4-hexatriene (Z). The calculated AIE is 8.37 eV and within the experimental uncertainties. The middle of the curve is in good agreement with the simulated spectra for 1,3,4-hexatriene, which has a calculated AIE of 8.54 eV. The latter part of the curve match with the simulated spectra of 2-hexen-4-yne (E), which has a calculated AIE of 8.55 eV. Opposingly, the experimental PIE at m/z = 80 for the

reaction of DMF + CD agrees with the summation of only 2-hexen-4-yne (E) and 1,2,4-hexatriene (Z) (Figure 8). The onset of the experimental curve is 8.40 ± 0.05 eV and matches the FC simulation for 1,2,4-hexatriene (Z). The latter part of the curves is in good agreement with the FC simulation of 2-hexen-4-yne (E). In Figure 9, the experimental curve at m/z = 81 for the reaction of DMF + CD has been modified by subtracting out the signal at m/z = 79 with respect to the $^{79}Br/^{81}Br$ isotopic ratio and the signal at m/z 80 with respect to the $^{12}C/^{13}C$ ratio. The remaining signal is found in good agreement with the FC simulation of 1,3,4-hexatriene meaning the product is d_5-1,3,4-hexatriene, which contains deuterium and, therefore, appears at m/z = 81 instead of m/z = 80. Despite all three products resulting from a loss of CHO, there are two separate pathways described in the next section, which are distinguished by the specific hydrogen that is lost.

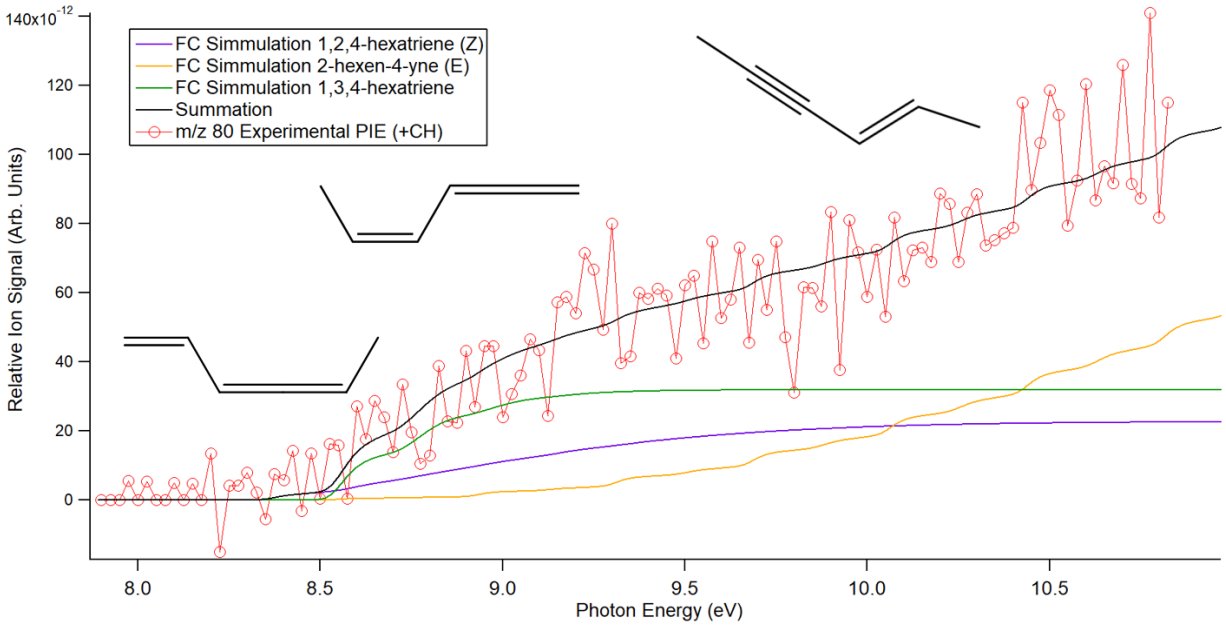

Figure 7. Summation (black line) of FC simulated PI spectra for 1,3,4-hexatriene (green line), 2-hexen-4-yne (E) (orange line) and 1,2,4-hexatriene (Z) (purple line) is overlaid and in good agreement with experimental curve for DMF + CH radical (red line) at m/z = 80 measured at 298 K.

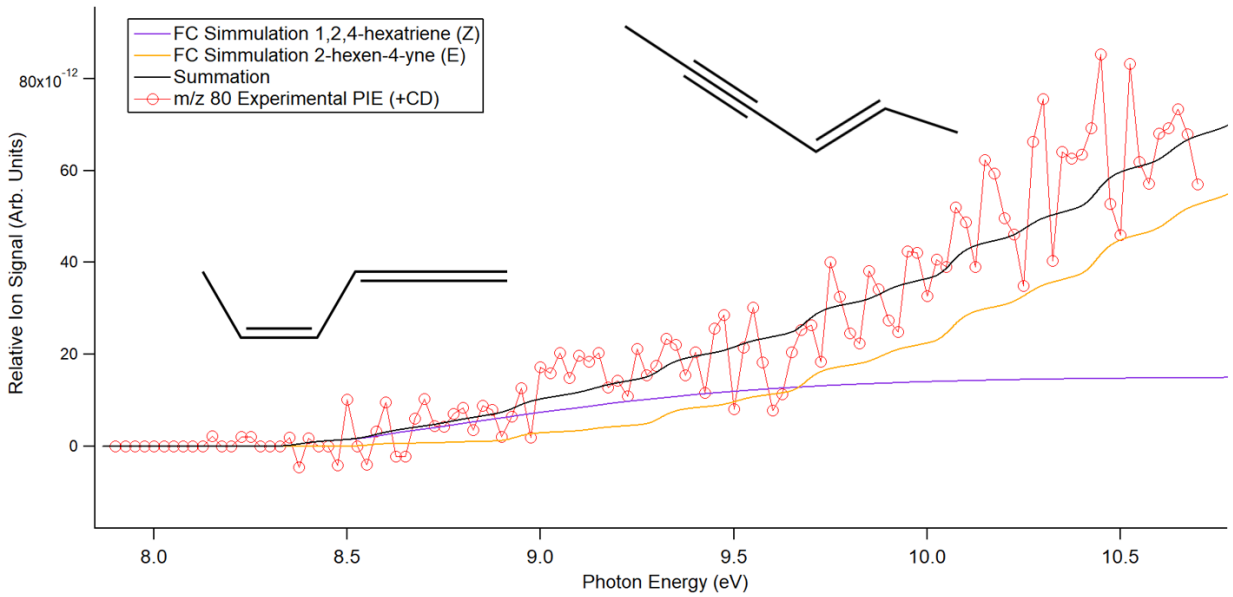

Figure 8. Summation (black line) of FC simulated PI spectra for 2-hexen-4-yne (E) (orange line) and 1,2,4-hexatriene (Z) (purple line) is overlaid and in good agreement with experimental curve for DMF + CD radical (red line) at m/z = 80 measured at 298 K.

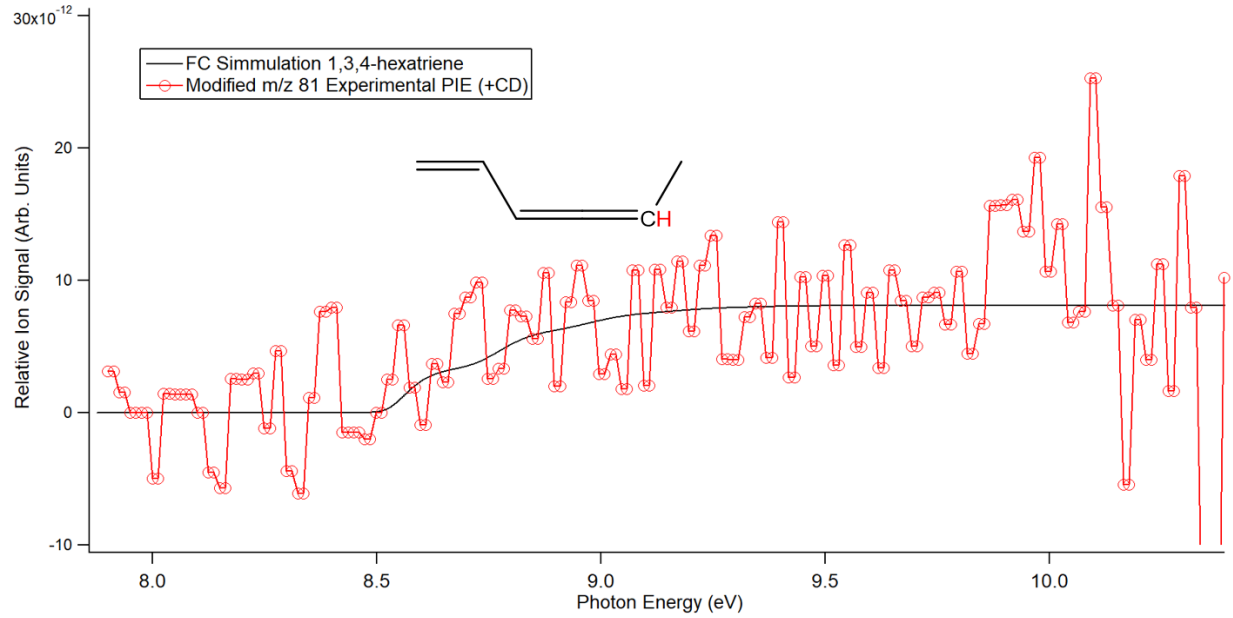

Figure 9. FC Simulation of 1,3,4-hexatriene (black line) overlaid and in good agreement with the modified experimental curve for DMF + CD radical (red line) at m/z = 81 measured at 298 K. The signal at m/z = 81 was modified by subtracting the signal at m/z = 79 with respect to the $^{79}Br/^{81}Br$ isotopic ratio and the signal at m/z 80 with respect to the $^{12}C/^{13}C$ ratio. The red H in the compound represents the deuterium.

Intermediates, if detected, would be observed at m/z = 109, 67, and 53. All intermediates to yield products at m/z = 108 would have signals shown at m/z = 109. Similarly, the intermediates leading to products detected at m/z = 66 and 52 would be observed at m/z = 67 and 53. The mechanisms will be described in detail in the next section. To verify the identity of the signals observed at m/z = 109 and 67, the isotopic portion for ^{13}C from the detected m/z = 108 and 66 signals were subtracted, respectively. The remaining signal at m/z = 109 is attributed to the summation of intermediates C1 and C2 from Figure 12 and B2 and B3 from Figure 11. Similarly, the summation of intermediates F4 from Figure 14 and C3, C4, and E1 from Figure 13 is determined to match the resulting signal at m/z = 67. These intermediates are the only compounds with bound cation and ionization energies within the relative experimental photon energy ranges. However, the experimental PI curves of both remaining signals cannot be confidently identified due to the large number of possible intermediates and low signal-to-noise ratios. Intermediate D1 in Figure 12, which leads to vinylacetylene, would be observed at m/z = 53. However, no signal is observed at m/z = 53 and the cation of the intermediate was found to be unbound.

5.5.2 Mechanism Pathways

By comparing the reaction of DMF with CH ($X^2\Pi$) with the reaction using CD radicals, a mechanism can be confidently proposed by tracing the movement of the deuterium. There are two entrance channels observed in this study, CH addition and CH insertion. As previously mentioned, 4 of the 5 primary signals result from CH addition to the л-bond system in the DMF ring, while only 1 primary signal results from CH insertion within the C-O bond. Both pathways have relatively low initial energy barriers and are overall exothermic. In the energy diagrams, a red line at 0 kJ/mol represents the zero reference point used for all energetic calculations of the

products. The zero reference point is based on the energy calculated from the sum of the 2,5-dimethylfuran and CH ($X^2\Pi$) radical optimized structures. Any reaction species or activation barriers found to be above the zero reference point are considered thermodynamically and kinetically unfavorable.

The two initial entrance channels are shown below in Scheme 1. Both pathways were verified by three-dimensional PES scans and in line with pathways seen in previous studies of CH radicals with small unsaturated alkenes.[12-13, 15-17] Intermediate radical A results from CH ($X^2\Pi$) addition to the л-bond to form a bicyclic ring intermediate, which optimized to the 6-membered ring compound. The calculated activation barrier is 18 kJ/mol and the addition releases 480 kJ/mol of energy. Overcoming a barrier of 185 kJ/mol, intermediates B and C result from the cleavage of one of the specific C-O bonds and have an enthalpy change of -298 kJ/mol. From acyclic intermediates B and C, mechanism pathways diverge to produce primary products at m/z = 108, 66, 52, and 42. The second entrance channel observed in this investigation is CH ($X^2\Pi$) insertion within the C-O bond. Possible interactions of CH radical with only the oxygen atom were also explored. However, no intermediates that could lead to the identified primary products were produced. Intermediate radical D is formed with a reaction enthalpy of -469 kJ/mol and an activation barrier of 24 kJ/mol. The bond between the oxygen and the carbon with the methyl group in the 6-membered ring (D) is then cleaved yielding the acyclic radical intermediate E. The calculated energy of intermediate E falls 278 kJ/mol below the reference point and forms after overcoming a barrier of 209 kJ/mol. Primary products at m/z = 80 form from diverging mechanism pathways starting with the shared intermediate E.

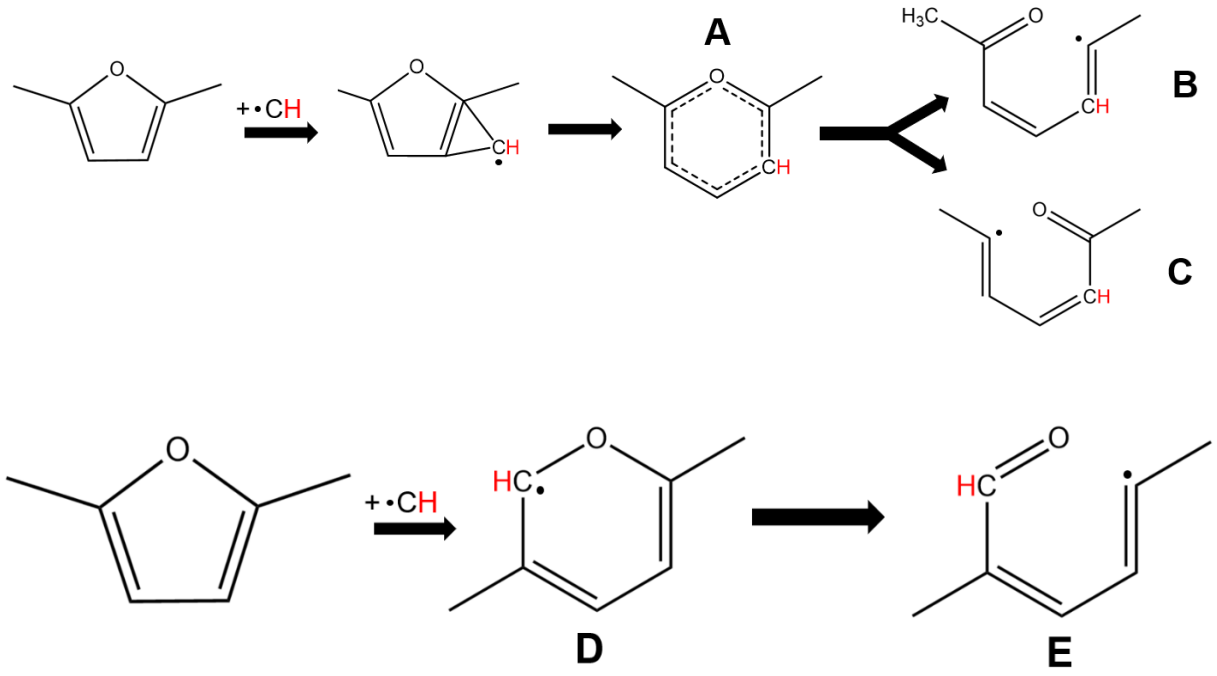

Scheme 1. Initial 6-membered radical ring intermediate (A and D) for CH addition and CH insertion in 2,5-dimethylfuran reactions. Shared intermediates (B, C, and E) are also shown and lead to all final products through diverging pathways.

5.5.3 CH Addition

The two C_7H_8O isomers, 3-hepten-5-yn-2-one and 3,5,6-heptatrien-2-one, are formed from intermediate B through H-loss pathways. After two dihedral rotations of intermediate B, a hydrogen is lost yielding 3-hepten-5-yn-2-one. In the energy diagram shown in Figure 10, the two rotated intermediates are represented by A1 and A2 with calculated energies falling below the zero-point reference by 317 and 321 kJ/mol, respectively. The corresponding activation barriers to form A1 and A2 are relatively very small at 10 and 4 kJ/mol. Overcoming a barrier of 164 kJ/mol, a hydrogen is lost from intermediate A2 forming the final product 3-hepten-5-yn-2-one. The calculated reaction enthalpy for the H-loss is -174 kJ/mol and overall exothermic for product formation. A second isomer is observed at m/z = 108, 3,5,6-heptatrien-2-one, and produced after two hydrogen transfers and a dihedral rotation detailed in Figure 11. A hydrogen

from the terminal carbon is transferred to the 6th carbon in the chain, where the radical is located, and releases 415 kJ/mol of energy to form intermediate B1. The transition state barrier for the transfer is 72 kJ/mol. Intermediate B1 then undergoes a dihedral rotation with a barrier of 295 kJ/mol and an enthalpy change of -267 kJ/mol forming a rotated intermediate represented by B2. Overcoming a barrier of 120 kJ/mol, a second hydrogen transfer occurs moving the hydrogen bonded to the 6th carbon to the 5th carbon in the chain producing intermediate B3. The heat of reaction for the transfer is calculated to be -295 kJ/mol. Intermediate B3 then loses a hydrogen and undergoes a final dihedral rotation producing 1,2,4-heptatrien-6-one as the final primary product with a calculated energy falling 168 kJ/mol below the reference point. The activation barriers for the H-loss and rotation are 148 kJ/mol and 18 kJ/mol, respectively. The formation of the final intermediate B4 has a calculated reaction enthalpy of -159 kJ/mol. The pathways forming both C_7H_8O isomers are overall exothermic and thermodynamically favorable. Figure 3 shows matching experimental curves at m/z = 108 for both reactions, which indicates that deuterium is not present in the final products and H in the entering CH radical is the specific hydrogen that is lost in the H-loss pathways described here.

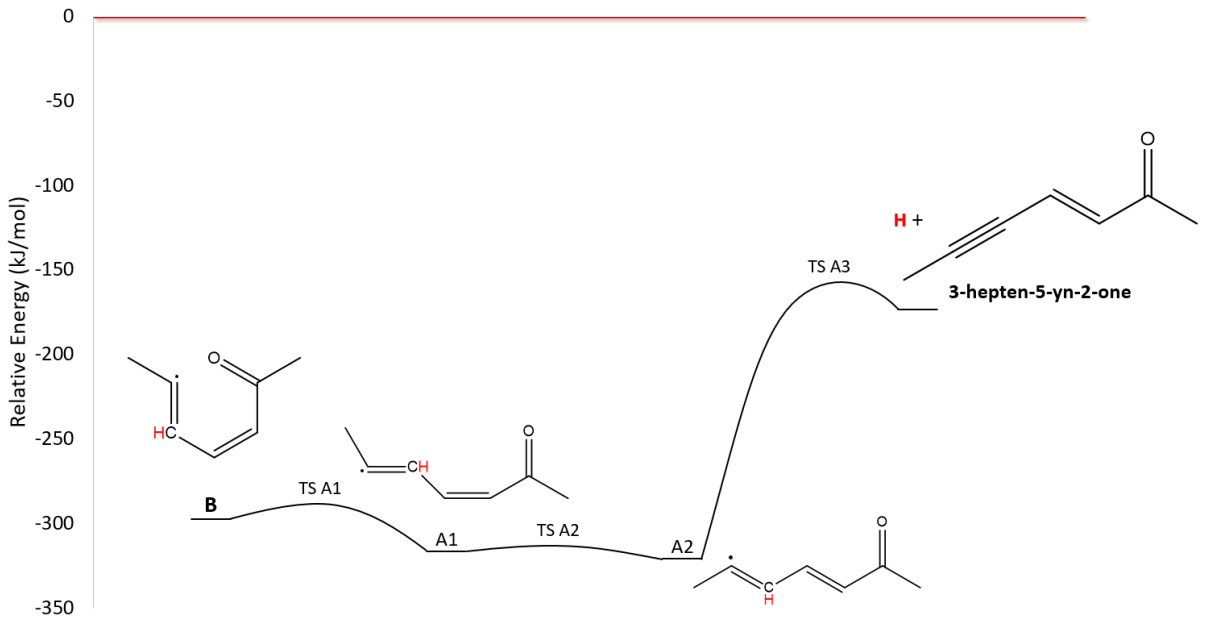

Figure 10. Potential energy surface diagram detailing the formation of 3-hepten-5-yn-2-one observed at m/z = 108 for the reactions of 2,5-dimethylfuran + CH ($X^2\Pi$) and CD radicals. The red line represents the reference zero point and the red H represents deuterium for the reaction with CD radicals.

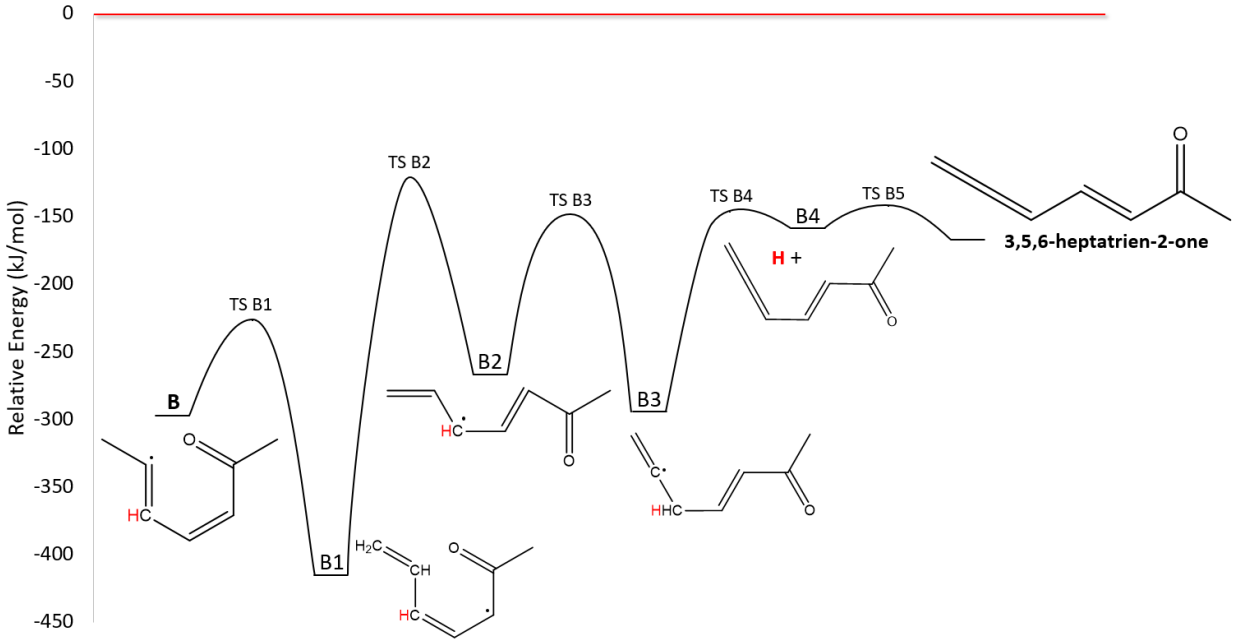

Figure 11. Potential energy surface diagram detailing the formation of 3,5,6-heptatrien-2-one observed at m/z = 108 for the reactions of 2,5-dimethylfuran + CH ($X^2\Pi$) and CD radicals. The red line represents the reference zero point and the red H represents deuterium for the reaction with CD radicals.

From intermediate C, four primary products are produced from two main diverging pathways. The energy diagrams represented in Figure 12 and 13 detail the pathways yielding two C_5H_6 isomers, and ketene. Vinylacetylene formation pathway shows that this species cannot be regarded as primary product. The formation of 1-penten-4-yne and 1,3-cyclopentadiene begin with two hydrogen transfers followed by the loss of ketene and a resulting radical fragment at m/z = 67. A hydrogen from the terminal carbon is transferred to the 6^{th} carbon and overcomes an activation barrier of 72 kJ/mol to form intermediate C1 (Figure 12). The corresponding enthalpy change is -347 kJ/mol. Then, the α-hydrogen is transferred to the γ-carbon with a barrier of 240 kJ/mol and causes a slight rotation. The resulting intermediate is represented by C2 and has a calculated energy that falls 347 kJ/mol below the reference point. From intermediate C2, the bond between the β-carbon and γ-carbon is cleaved yielding ketene and a radical C_5H_7 fragment (C3). The cleavage has an energy barrier of 98 kJ/mol and an overall enthalpy change of -309 kJ/mol. The resulting C_5H_7 fragment then loses a hydrogen forming two C_5H_6 isomer products via distinct pathways detailed in the energy diagram shown in Figure 13. The β-hydrogen is transferred to the γ-carbon after overcoming a barrier of 143 kJ/mol forming intermediate E1. The calculated enthalpy change for the transfer is -178 kJ/mol. The final product 1-pent-4-yne is formed from the loss of hydrogen from intermediate E1 and has a calculated energy that falls 27 kJ/mol below the reference point. The corresponding energy barrier for the H-loss is 151 kJ/mol. Alternatively, intermediate C3 is also observed to undergo a dihedral rotation causing a ring formation, which ultimately yields 1,3-cyclopentadiene after a hydrogen loss. The dihedral rotation has a relatively small barrier of 38 kJ/mol of energy and a calculated reaction enthalpy of -296 kJ/mol. The rotated intermediate represented by C4 then forms a ring intermediate (C5) with a small energy barrier of 24 kJ/mol and an enthalpy change of -346 kJ/mol. Intermediate C5

then overcomes an activation barrier of 181 kJ/mol and loses a hydrogen forming the final product 1,3-cyclopentadiene. The calculated reaction enthalpy is -165 kJ/mol for the H-loss and overall exothermic for product formation.

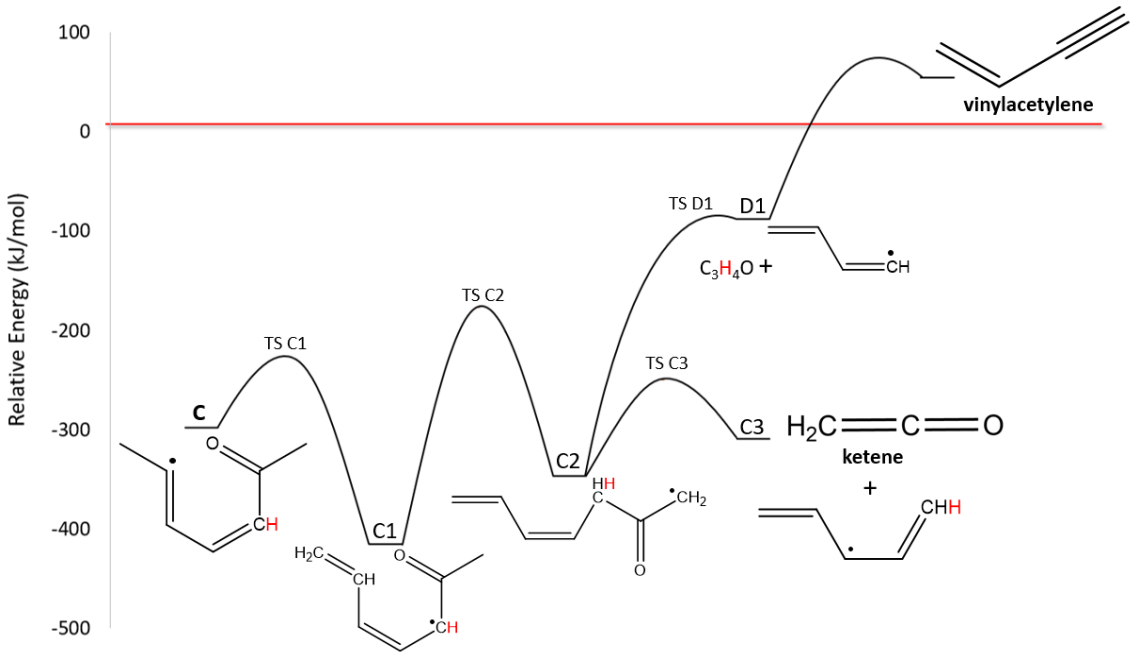

Figure 12. Potential energy surface diagram detailing the formation of vinylacetylene, ketene, and a C_5H_7 fragment for the reactions of 2,5-dimethylfuran + CH ($X^2\Pi$) and CD radicals. The red line represents the reference zero point and the red H represents deuterium for the reaction with CD radicals.

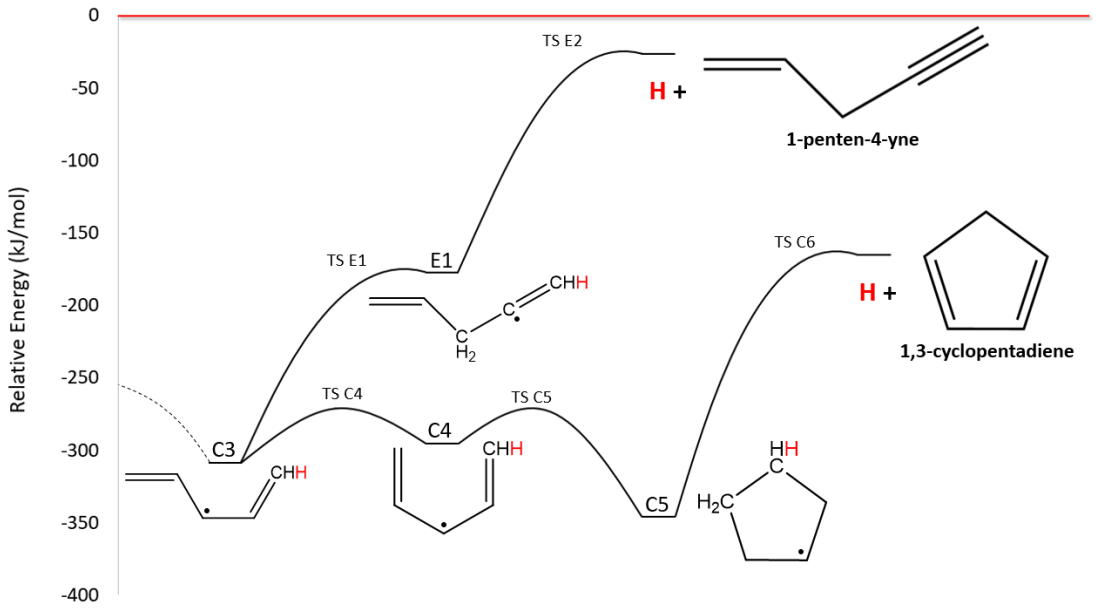

Figure 13. Continued potential energy surface diagram detailing the formation of 1,3-cyclopentadiene and 1-penten-4-yne from the C_5H_7 fragment for the reactions of 2,5-dimethylfuran + CH ($X^2\Pi$) and CD radicals. The red line represents the reference zero point and the red H represents deuterium for the reaction with CD radicals.

Another pathway yielding the third C_5H_6 isomer observed and ketene begins with intermediate C followed by a dihedral rotation, two hydrogen transfers, and a final H-loss. The mechanism is detailed in the energy diagram shown in Figure 14. The dihedral rotation of intermediate C has an activation barrier of 6 kJ/mol and releases 293 kJ/mol of energy to yield an intermediate represented by F1. Then, the α-hydrogen moves to the 6th carbon in the chain producing intermediate F2. The transfer has an energy barrier of 26 kJ/mol and a reaction enthalpy of -352 kJ/mol. The bond between the β-carbon and γ-carbon in F2 is cleaved after overcoming a barrier of 192 kJ/mol of energy forming ketene and a C_5H_7 radical fragment (F3). The calculated enthalpy change for the cleavage falls 180 kJ/mol below the reference point. In the C_5H_7 fragment, the β-hydrogen is transferred to the alpha carbon resulting in intermediate F4. The activation barrier for the transfer is 189 kJ/mol and the calculated heat of reaction is -237 kJ/mol. A hydrogen is lost from intermediate F4 forming the final product 2-pent-4-yne after overcoming an activation barrier of 187 kJ/mol. The enthalpy change is calculated to be -49

kJ/mol and overall production formation is exothermic. In Figure 4 and 5, experimental curves of m/z = 66 and 42 for the two investigated reactions are shown to be matching and, therefore, the specific hydrogen lost from the C_5H_7 fragment must be the deuterium. This provides additional support for the proposed mechanisms.

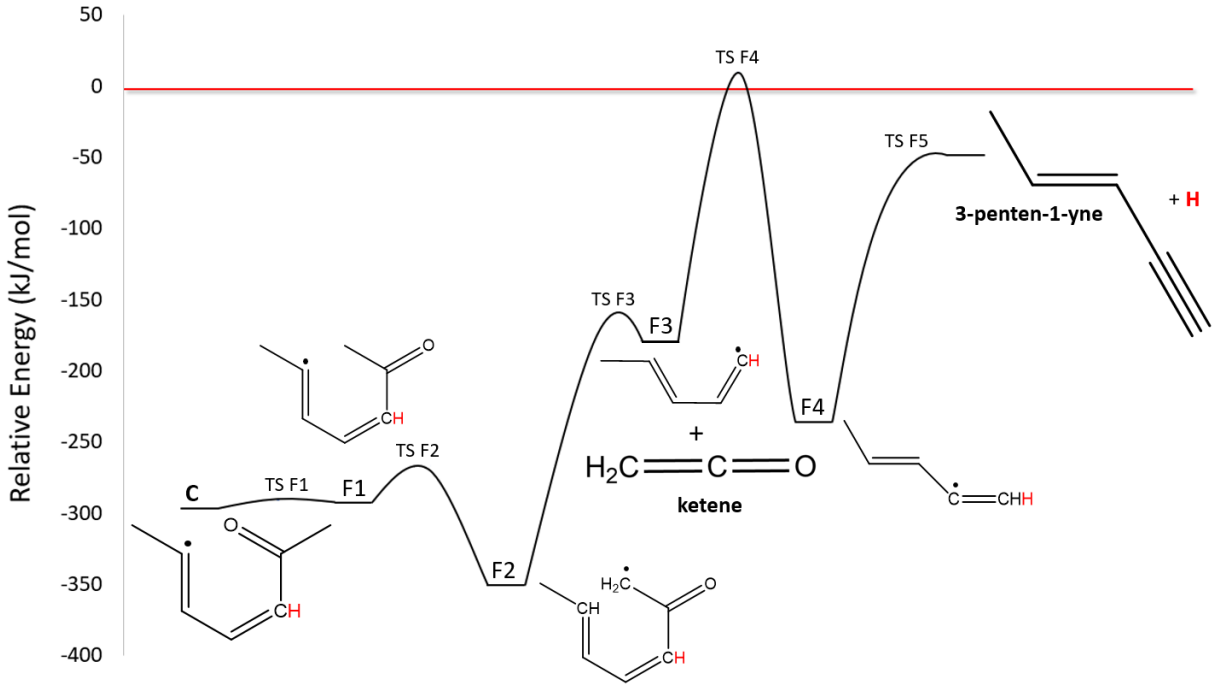

Figure 14. Potential energy surface diagram detailing the formation of ketene and 3-penten-1-yne for the reactions of 2,5-dimethylfuran + CH ($X^2\Pi$) and CD radicals. The red line represents the reference zero point and the red H represents deuterium for the reaction with CD radicals.

Vinylacetylene is produced from an alternate pathway of intermediate C2 shown in the energy diagram detailed in Figure 12. Instead of the cleavage of the β-carbon and γ-carbon bond, the bond between the δ-carbon and ε-carbon is cleaved forming two fragments: C_3H_4O and C_4H_5. The corresponding activation barrier and heat of reaction were calculated to be 259 kJ/mol and -88 kJ/mol, respectively. The C_4H_5 fragment would be detected at m/z = 56, however, no signal is observed in this investigation. The C_3H_4O fragment loses a hydrogen from the β-carbon to form vinylacetylene after overcoming a barrier of 73 kJ/mol. The calculated energy change for

vinylacetylene formation lies above the reference point by 52 kJ/mol and for this reason it is regarded as a secondary product, because the computed pathway cannot explain its formation both kinetically and thermodynamically. The experimental PI curves for m/z = 52 shown in Figure 6 are in very good agreement.

For all products formed via CH addition, both reactions share the same primary products and have matching experimental PI spectra. By comparing the two reactions, it is deduced that deuterium must have been lost in the reaction with CD radicals. Therefore, the it is also the hydrogen that is introduced with the initial CH radical reactant that is lost in the reaction with CH radicals.

5.5.4 CH Insertion

The three primary products observed at m/z = 80 are formed from CH insertion pathways with a shared intermediate E (Scheme 1) and detailed in the energy diagram shown in Figure 15, 16, and 17. All products are C_6H_8 isomers, exothermic, and thermodynamically favorable. As previously mentioned, the two experimental PI curves for m/z = 80 do not match, meaning the initial H added with the CH radical is present in one of the three final products. The two shared isomers are 2-hexen-4-yne and 1,2,4-hexatriene. From intermediate E, 2-hexen-4-yne is produced from a dihedral rotation, hydrogen transfer, and a loss of the aldehyde group. The rotated intermediate is represented by intermediate A1 and forms after overcoming a relatively small barrier of 8 kJ/mol (Figure 15). The calculated enthalpy change of the rotation is -297 kJ/mol. A hydrogen transfer occurs in intermediate A1 moving the γ-hydrogen to the ε-carbon releasing 301 kJ/mol of energy forming intermediate A2. The corresponding activation barrier for the transfer is 179 kJ/mol. Finally, 2-hexen-4-yne is formed with the loss of the aldehyde group after overcoming a barrier of 99 kJ/mol. The heat of reaction is -214 kJ/mol and product

formation is overall exothermic. Opposingly, intermediate E also undergoes a series of four hydrogen transfers and the loss of the aldehyde group to form 1,2,4-hexatriene as shown in Figure 16. The first hydrogen transfer has an activation barrier of 17 kJ/mol and transfers the hydrogen on the terminal carbon in the chain to the ε-carbon. The resulting intermediate is represented by B1 and has a calculated energy that falls 399 kJ/mol below the reference point. The second and third hydrogen transfer moves the δ-hydrogen to the carbon with the aldehyde group and the γ-hydrogen to the δ-carbon forming intermediate B2 then B3. The calculated reaction enthalpies for the transfers are -398 and -309 kJ/mol with activation barriers of 1 and 92 kJ/mol, respectively. The final hydrogen results in intermediate B4 after the β-hydrogen moves to the γ-carbon. The calculated activation barrier is 7 kJ/mol and the heat of reaction is -314 kJ/mol for the transfer. With a calculated energy that falls 196 kJ/mol below the reference point, 1,2,4-hexatriene is formed by the loss of the aldehyde group from intermediate B4. The corresponding activation barrier is 122 kJ/mol.

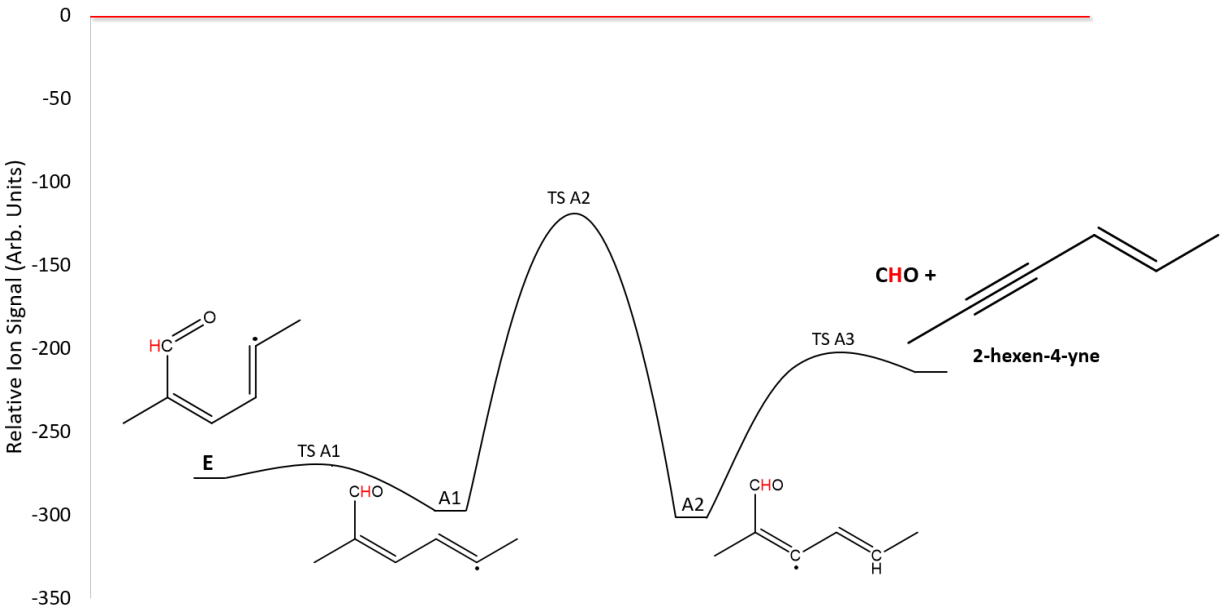

Figure 15. Potential energy surface diagram detailing the formation of 2-hexen-4-yne (E) for the reactions of 2,5-dimethylfuran + CH ($X^2\Pi$) and CD radicals. The red line represents the reference zero point and the red H represents deuterium for the reaction with CD radicals.

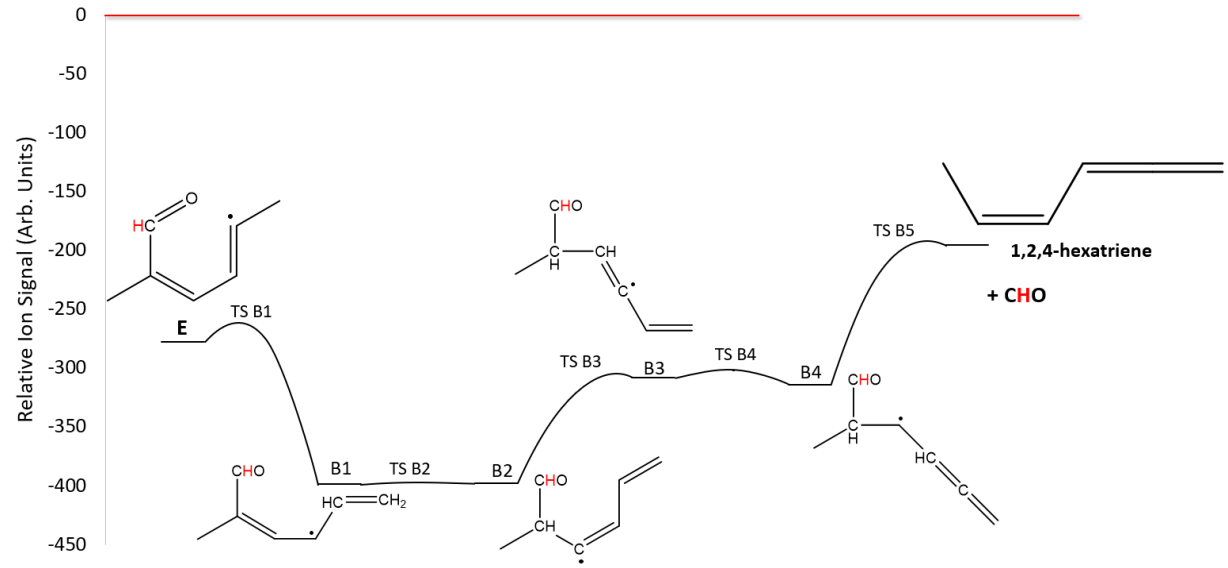

Figure 16. Potential energy surface diagram detailing the formation of 1,2,4-hexatriene (Z) for the reactions of 2,5-dimethylfuran + CH ($X^2\Pi$) and CD radicals. The red line represents the reference zero point and the red H represents deuterium for the reaction with CD radicals.

The third C_6H_8 isomer observed is 1,3,4-hexatriene. In the reaction with CD radicals, the product is observed as d_5-1,3,4-hexatriene at m/z = 81. From intermediate E, 1,3,4-hexatriene is formed after a dihedral rotation, two hydrogen transfers, and the loss of a carbonyl group and hydrogen detailed in energy diagram shown in Figure 17. C1 represents the rotated intermediate and has a calculated energy that falls 295 kJ/mol below the reference point. The corresponding activation energy is relatively small at 5 kJ/mol. Overcoming a barrier of 16 kJ/mol, a hydrogen from the aldehyde group is transferred to the ε-carbon with a calculated enthalpy change of -371 kJ/mol. The resulting intermediate (C2) loses a carbonyl group to form intermediate C3. The activation barrier and heat of reaction for the loss is 94 and -288 kJ/mol, respectively. Next, the α-hydrogen is transferred to the β-carbon with an energy barrier of 174 kJ/mol yielding intermediate C4. The calculated reaction enthalpy for the transfer is -405 kJ/mol. Finally, the δ-hydrogen from intermediate C4 is lost forming the primary product 1,3,4-hexatriene that has an energy that falls 42 kJ/mol below the reference point. The final activation barrier is 284 kJ/mol and product formation is overall exothermic. Mechanism pathways based on the presence or absence of deuterium further support product identification.

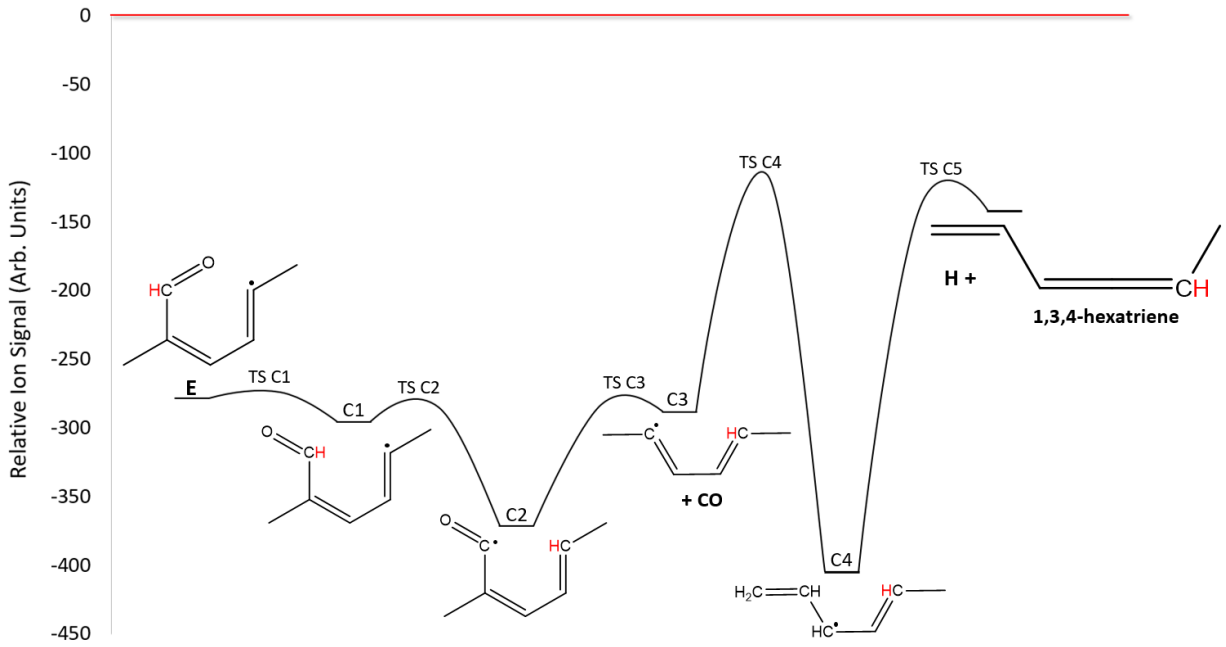

Figure 17. Potential energy surface diagram detailing the formation of 1,3,4-hexatriene for the reactions of 2,5-dimethylfuran + CH ($X^2\Pi$) and CD radicals. The red line represents the reference zero point and the red H represents deuterium for the reaction with CD radicals.

Unlike all the other primary products, 1,3,4-hexatriene is observed at different m/z ratios for the two reactions. This indicates that the hydrogen from the CH radical reactant is present in the final compound and the mechanism is an H-loss pathway rather than a D-loss pathway. The CO-loss followed by H-loss pathway is the only mechanism that loses the initial carbon and does not lose the initial hydrogen from the CH radical reactant.

5.5.5 H-Assisted Isomerization

From the number densities of the reactants and assuming an average molecular diameter of 0.25 nm for the reacting species, a few thousand collisions are expected at room temperature. Under these conditions the H-assisted isomerization should also be considered as possible reaction pathways to yield the observed products at m/z = 66, 80, and 108.

Two C_7H_8O isomers are formed at m/z = 108 and Figure 18 details the proposed Hassisted isomerization of 3,5,6-heptatriene-2-one into 3-hepten-5-yn-2-one. An H atom adds to

the terminal carbon, with an exothermicity of 151 kJ/mol of energy. The addition results in the loss of the ε-hydrogen to form 3-heptene-5-yn-2-one. The respective barriers for each step are relatively very small at 9 and 10 kJ/mol.

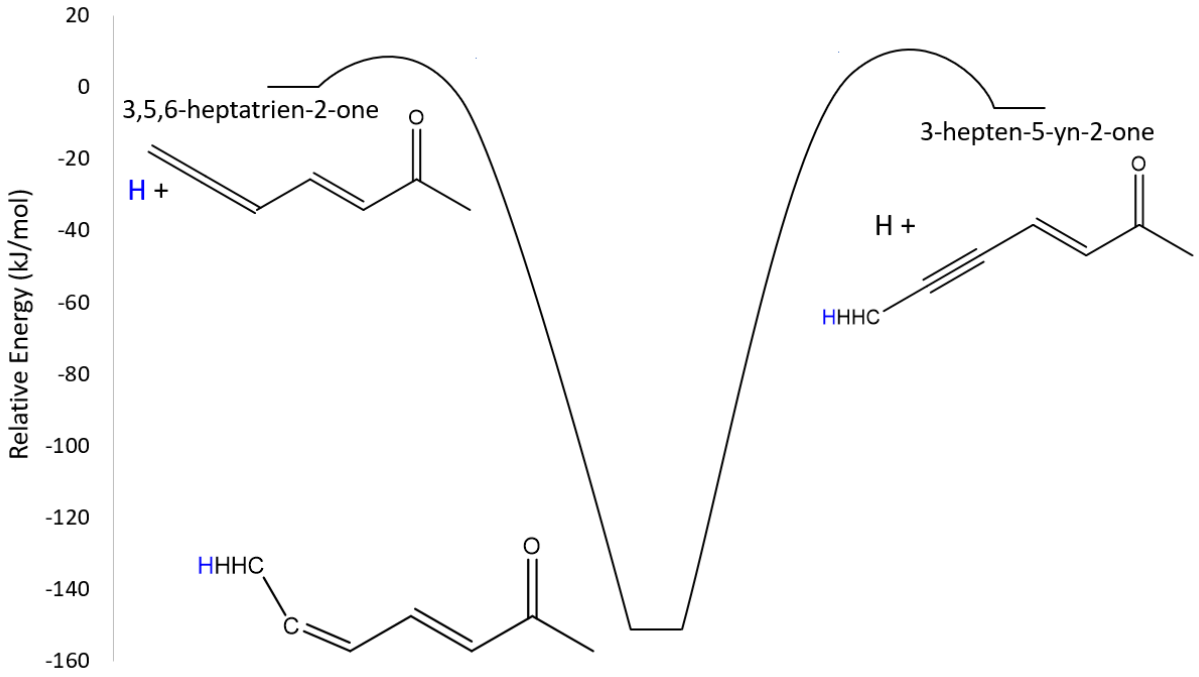

Figure 18. Potential energy surface diagram detailing the formation of 3-hepten-5-yn-2-one from 3,5,6-heptatriene-2-one via H-assisted isomerization. The blue H represents the H atom utilized by the isomerization.

Of the three C5H6 isomers observed at m/z = 66, the only possible H-assisted isomerization is from 3-penten-1-yne to 1-penten-4-yne (Figure 19). An H atom can be added to the γ-carbon of 3-penten-1-yne after overcoming a barrier of 13 kJ/mol and releasing -123 kJ/mol. Then, 1-penten-4-yne forms from the loss of the δ-hydrogen with an activation energy of 26 kJ/mol.

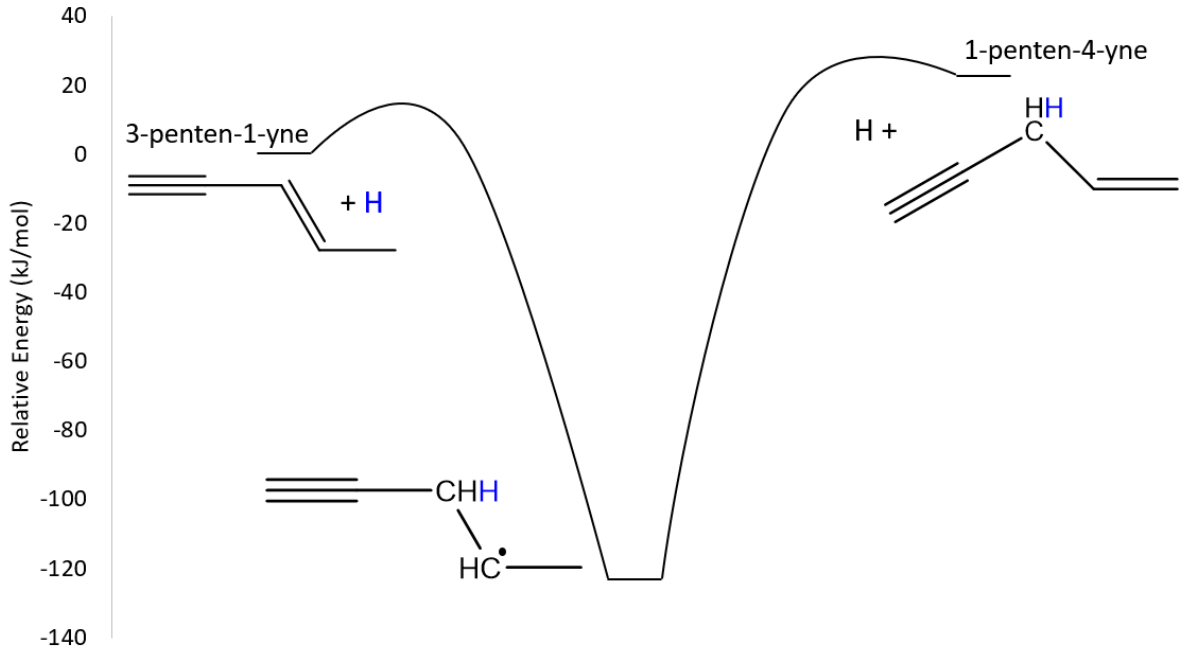

Figure 19. Potential energy surface diagram detailing the formation of 1-penten-4-yne from 3-penten-1-yne via H-assisted isomerization. The blue H represents the H atom utilized by the isomerization.

At m/z = 80, three C6H8 isomers are also observed and two H-assisted isomerizations are possible. Figure 20 shows the proposed mechanism for 1,3,4-hexatriene isomerization to form 2-hexen-4-yne. The addition of an H atom to the α-carbon on the 1,3,4-hexatriene is barrier-less with an exothermicity of 186 kJ/mol of energy. The resulting intermediate then loses the hydrogen on the 5th carbon in the chain, which is also the deuterium in the reaction with CD radicals, to form 2-hexen-4-yne. The corresponding activation barrier for the H/D-loss is 180 kJ/mol. Alternatively, 2-hexen-4-yne can also be formed from 1,2,4-hexatriene as shown in Figure 21. On 1,2,4-hexatriene, a hydrogen atom can add to the α-carbon, which will then cause the loss of hydrogen from γ-carbon to yield 2-hexen-4-yne. The respective energy barrier for the hydrogen loss is 149 kJ/mol, while the hydrogen addition is barrier-less with an exothermicity of 152 kJ/mol of energy.

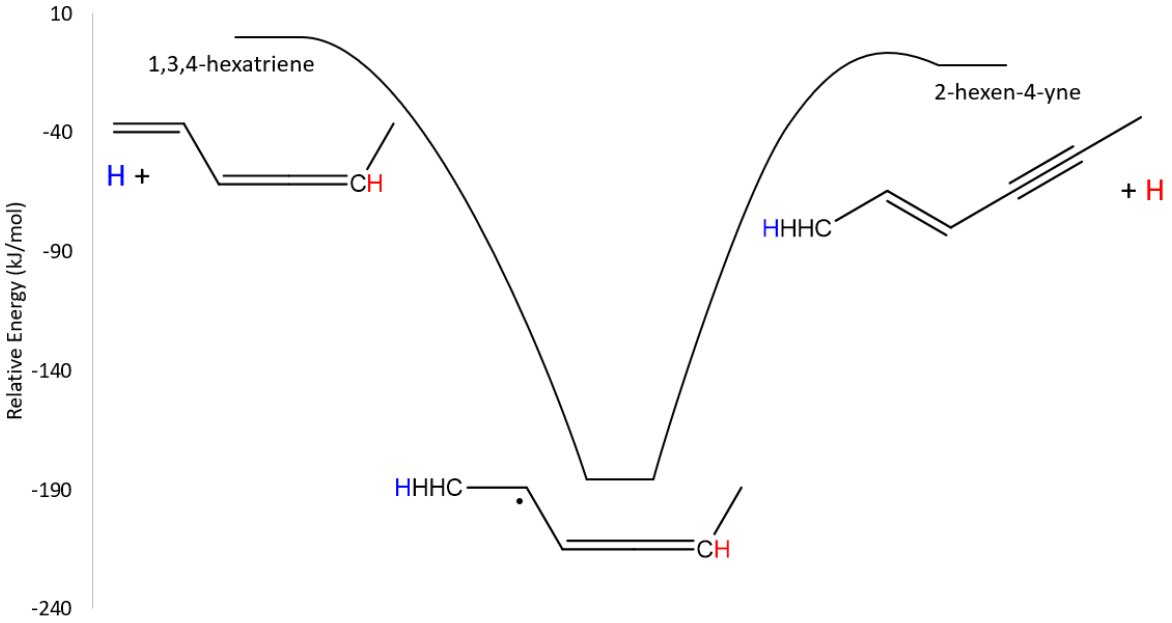

Figure 20. Potential energy surface diagram detailing the formation of 2-hexen-4-yne from 1,3,4-hexatriene via H-assisted isomerization. The blue H represents the H atom utilized by the isomerization whereas the red H represents the deuterium for the reaction with CD radicals.

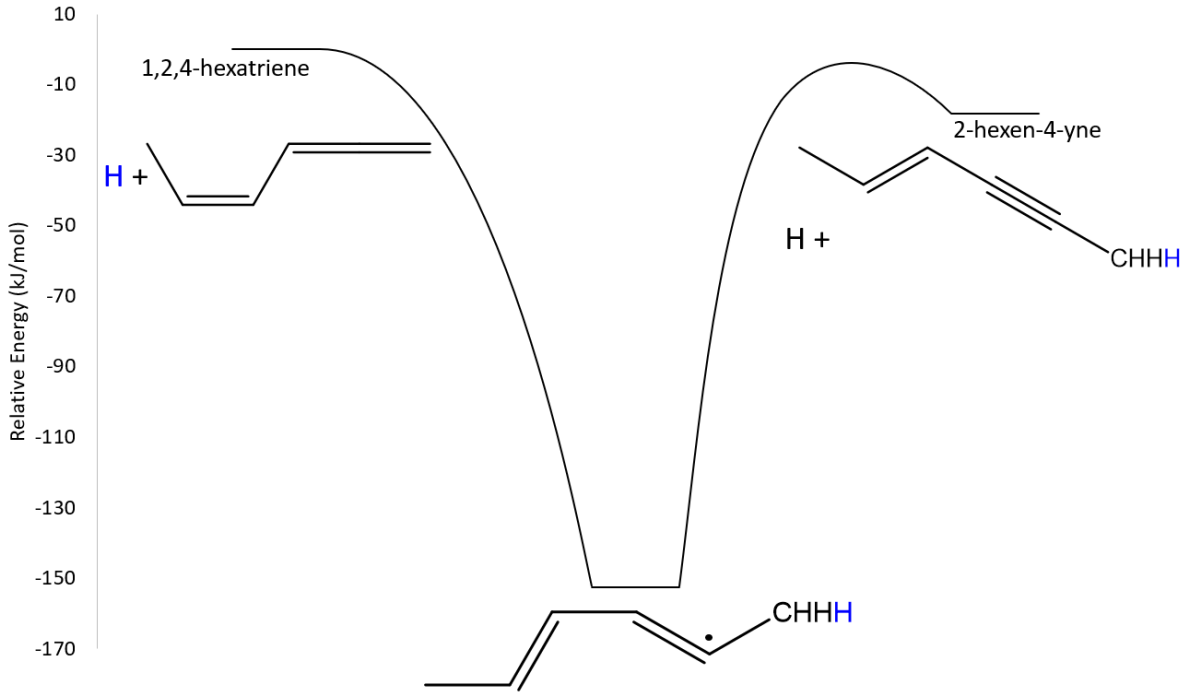

Figure 21. Potential energy surface diagram detailing the formation of 2-hexen-4-yne from 1,2,4-hexatriene via H-assisted isomerization. The blue H represents the H atom utilized by the isomerization.

5.6 Conclusion

The reactions of 2,5-dimethlyfuran + CH ($X^2\Pi$) and + CD radicals at 298 K were studied using synchrotron radiation coupled with multiplexed photoionization mass spectrometry at the Lawrence Berkeley National Laboratory. Based on kinetic time traces and photoionization spectra, primary products were identified. The comparison of the experimental curves at the same m/z ratios for the two reactions allowed for further support of product identification and mechanism pathways based on the presence or absence of deuterium. CBS-QB3 level of theory was used for all energy calculations and to determine reaction mechanisms. The two entrance channels are observed in this work are CH addition to the л-bond system and CH insertion within the C-O bond, yielding initial 6-membered ring radical intermediates. As seen in previous studies, CH addition pathway was more favored and lead to the formation of nearly all primary products observed. Patterns of H-loss, CHO-loss, and CO-loss observed were also in agreement with trends observed in other similar studies. From CH addition pathway, products at m/z = 108, 66, and 42 were observed. At m/z = 108, the two C_7H_8O isomers formed were 1,2,4-heptatrien-6-one and 3-hepten-5-yne-2-one through H-loss mechanisms. Diverging from the shared 6-membered ring intermediate, ketene and three C_5H_6 isomers were formed congruently. The isomers were identified as 1,3-cyclopentadiene, 3-penten-1-yne (E), and 1-pent-4-yne. Vinylacetylene is also observed but based on the computation of the potential energy scan it is not regarded as a primary product. In the CH insertion entrance pathways, CH radical is inserted within the C-O bond to also yield an initial 6-membered ring radical intermediate. Three C_6H_8 isomers are produced via CH insertion. The two isomers shared by both reactions at m/z = 80 are 1,2,4-hexatriene (Z) and 2-hexen-4-yne (E) and result from the loss of the aldehyde group. Through the loss of a carbonyl group then hydrogen, 1,3,4-hexatriene is formed and observed in

the reaction with CH radicals at m/z = 80. In the reaction with CD radicals, the product is observed as d_5-1,3,4-hexatriene at m/z = 81, meaning that deuterium in present. This CO-loss pathway is the only mechanism that keeps the initial hydrogen added with the radical reactant. Finally, H-assisted isomerization has also been considered and the results presented for the m/z = 66, 80, and 108 isomers.

5.7 Acknowledgements

This work is supported by the American Chemical Society – Petroleum Research Fund Grant # 56067-UR6 and the University of San Francisco via the Faculty Development Fund. The authors would also like to acknowledge Drs. Taatjes and Osborn from Sandia National Laboratories for the use of the experimental apparatus. The Advanced Light Source is supported by the Director, Office of Science, Office of Basic Energy Sciences, of the U.S. Department of Energy under Contract No. DE-AC02-05CH11231.

5.8 References

1. Malpani, S. J., E. , 2, 5-Dimethylfuran As A Bio-Fuel. *J. Environ. Sci., Toxicol. Food Tech.* **2015,** *9* (5), 71-72.

2. Christensen, E.; Yanowitz, J.; Ratcliff, M.; McCormick, R. L., Renewable Oxygenate Blending Effects on Gasoline Properties. *Energy Fuels* **2011,** *25* (10), 4723-4733.

3. Mascal, M.; Nikitin, E. B., Direct, High-Yield Conversion of Cellulose into Biofuel. *Angew. Chem., Int. Ed.* **2008,** *47* (41), 7924-7926.

4. Schenk, P. M. T.-H., S.R.; Stephens, E.; Marx, U. C.; Mussgnug, J. H.; Posten, C.; Kruse, O.; Hankamer, B., Second Generation Biofuels: High-Efficiency Microalgae for Biodiesel Production. *Bioenerg. Res.* **2008,** *1* (1), 20-43.

5. Naik, S. N.; Goud, V. V.; Rout, P. K.; Dalai, A. K., Production of first and second generation biofuels: A comprehensive review. *Renewable and Sustainable Energy Reviews* **2010,** *14* (2), 578-597.

6. Tian, G. D., R. ; Xu, H., *A New Biofuel Candidate, Biofuel Production - Recent Developments and Prospects*. InTech: 2011; Vol. Chapter 19.

7. Román-Leshkov, Y.; Barrett, C. J.; Liu, Z. Y.; Dumesic, J. A., Production of dimethylfuran for liquid fuels from biomass-derived carbohydrates. *Nature* **2007,** *447*, 982.

8. Zhao, H.; Holladay, J. E.; Brown, H.; Zhang, Z. C., Metal Chlorides in Ionic Liquid Solvents Convert Sugars to 5-Hydroxymethylfurfural. *Science* **2007,** *316* (5831), 1597.

9. Xu, H.; Wang, C., A Comprehensive Review of 2,5-Dimethylfuran as a Biofuel Candidate. In *Biofuels from Lignocellulosic Biomass*, Wiley-VCH Verlag GmbH & Co. KGaA: 2016; pp 105-129.

10. Eldeeb, M. A.; Akih-Kumgeh, B., Reactivity Trends in Furan and Alkyl Furan Combustion. *Energy Fuels* **2014,** *28* (10), 6618-6626.

11. Gouli, S.; Lois, E.; Stournas, S., Effects of Some Oxygenated Substitutes on Gasoline Properties, Spark Ignition Engine Performance, and Emissions. *Energy Fuels* **1998,** *12* (5), 918-924.

12. Goulay, F.; Derakhshan, A.; Maher, E.; Trevitt, A. J.; Savee, J. D.; Scheer, A. M.; Osborn, D. L.; Taatjes, C. A., Formation of Dimethylketene and Methacrolein by Reaction of the CH Radical with Acetone. *Phys. Chem. Chem. Phys.* **2013,** *15* (11), 4049-4058.

13. Goulay, F.; Trevitt, A. J.; Savee, J. D.; Bouwman, J.; Osborn, D. L.; Taatjes, C. A.; Wilson, K. R.; Leone, S. R., Product Detection of the CH Radical Reaction with Acetaldehyde. *J. Phys. Chem. A* **2012,** *116* (24), 6091-106.

14. Becker, K. H.; Engelhardt, B.; Wiesen, P.; Bayes, K. D., Rate Constants for Methylidyne (X2Π) Reactions at Low Total Pressures. *Chem. Phys. Lett.* **1989,** *154* (4), 342-8.

15. Goulay, F.; Trevitt, A. J.; Meloni, G.; Selby, T. M.; Osborn, D. L.; Taatjes, C. A.; Vereecken, L.; Leone, S. R., Cyclic Versus Linear Isomers Produced by Reaction of the Methylidyne Radical (CH) with Small Unsaturated Hydrocarbons. *J. Am. Chem. Soc.* **2009,** *131* (3), 993-1005.

16. Trevitt, A. J.; Prendergast, M. B.; Goulay, F.; Savee, J. D.; Osborn, D. L.; Taatjes, C. A.; Leone, S. R., Product Branching Fractions of the CH + Propene Reaction from Synchrotron Photoionization Mass Spectrometry. *J. Phys. Chem. A* **2013,** *117* (30), 6450-6457.

17. Carrasco, E.; Smith, K. J.; Meloni, G., Synchrotron Photoionization Study of Furan and 2-Methylfuran Reactions with Methylidyne Radical (CH) at 298 K. *The Journal of Physical Chemistry A* **2018,** *122* (1), 280-291.

18. Winfough, M.; Yao, R.; Ng, M.; Catani, K.; Meloni, G., Synchrotron Photoionization Investigation of the Oxidation of Ethyl tert-Butyl Ether. *J. Phys. Chem. A* **2017,** *121* (7), 1460-1469.

19. Ng, M. Y.; Bryan, B. M.; Nelson, J.; Meloni, G., Study of tert-Amyl Methyl Ether Low Temperature Oxidation Using Synchrotron Photoionization Mass Spectrometry. *J. Phys. Chem. A* **2015,** *119* (32), 8667-8682.

20. Ray, A. W.; Taatjes, C. A.; Welz, O.; Osborn, D. L.; Meloni, G., Synchrotron Photoionization Measurements of OH-Initiated Cyclohexene Oxidation: Ring-Preserving Products in OH + Cyclohexene and Hydroxycyclohexyl + O2 Reactions. *J. Phys. Chem. A* **2012,** *116* (25), 6720-6730.

21. Ng, M. Y.; Nelson, J.; Taatjes, C. A.; Osborn, D. L.; Meloni, G., Synchrotron Photoionization Study of Mesitylene Oxidation Initiated by Reaction with Cl(2P) or O(3P) Radicals. *J. Phys. Chem. A* **2014,** *118* (21), 3735-3748.

22. Romanzin, C.; Boye-Peronne, S.; Gauyacq, D.; Benilan, Y.; Gazeau, M. C.; Douin, S., CH Radical Production from 248 nm Photolysis or Discharge-Jet Dissociation of CHBr3 Probed by

Cavity Ring-Down Absorption Spectroscopy. *J. Chem. Phys.* **2006,** *125* (11), 114312/1-114312/9.

23. Zou, P.; Shu, J.; Sears, T. J.; Hall, G. E.; North, S. W., Photodissociation of Bromoform at 248 nm: Single and Multiphoton Processes. *J. Phys. Chem. A* **2004,** *108* (9), 1482-1488.

24. Osborn, D. L.; Zou, P.; Johnsen, H.; Hayden, C. C.; Taatjes, C. A.; Knyazev, V. D.; North, S. W.; Peterka, D. S.; Ahmed, M.; Leone, S. R., The Multiplexed Chemical Kinetic Photoionization Mass Spectrometer: A New Approach to Isomer-Resolved Chemical Kinetics. *Rev. Sci. Instrum.* **2008,** *79* (10, Pt. 1), 104103/1-104103/10.

25. Chupka, W. A.; Berkowitz, J., Photoionization of Ethane, Propane, and n-Butane with Mass Analysis. *J. Chem. Phys.* **1967,** *47* (8), 2921-2933.

26. Montgomery, J. A., Jr.; Frisch, M. J.; Ochterski, J. W.; Petersson, G. A., A Complete Basis Set Model Chemistry. VI. Use of Density Functional Geometries and Frequencies. *J. Chem. Phys.* **1999,** *110* (6), 2822-2827.

27. Montgomery, J. A., Jr.; Frisch, M. J.; Ochterski, J. W.; Petersson, G. A., A Complete Basis Set Model Chemistry. VII. Use of the Minimum Population Localization Method. *J. Chem. Phys.* **2000,** *112* (15), 6532-6542.

28. Frisch, M. J. T., G. W.; Schlegel, H. B.; Scuseria, G. E.; Robb, M. A.; Cheeseman, J. R.; Scalmani, G.; Barone, V.; Petersson, G. A.; Nakatsuji, H. et. al. *Gaussian 09*, Gaussian Inc.: Wallingford CT, 2009.

29. Cool, T. A.; McIlroy, A.; Qi, F.; Westmoreland, P. R.; Poisson, L.; Peterka, D. S.; Ahmed, M., Photoionization Mass Spectrometer for Studies of Flame Chemistry with a Synchrotron Light Source. *Rev. Sci. Instrum.* **2005,** *76* (9), 094102/1-094102/7.

30. Santoro, F.; Lami, A.; Improta, R.; Barone, V., Effective Method to Compute Vibrationally Resolved Optical Spectra of Large Molecules at Finite Temperature in the Gas Phase and in Solution. *J. Chem. Phys.* **2007,** *126* (18), 184102/1-184102/11.

31. Sharp, T. E.; Rosenstock, H. M., Franck—Condon Factors for Polyatomic Molecules. *J. Chem. Phys.* **1964,** *41* (11), 3453-3463.

32. Ruhoff, P. T., Recursion Relations for Multi-Dimensional Franck-Condon Overlap Integrals. *Chem. Phys.* **1994,** *186* (2), 355-374.

33. Tirado-Rives, J.; Jorgensen, W. L., Performance of B3LYP Density Functional Methods for a Large Set of Organic Molecules. *J. Chem. Theory Comput.* **2008,** *4* (2), 297-306.

34. Taatjes, C. A.; Osborn, D. L.; Selby, T. M.; Meloni, G.; Trevitt, A. J.; Epifanovsky, E.; Krylov, A. I.; Sirjean, B.; Dames, E.; Wang, H., Products of the Benzene + O(3P) Reaction. *The Journal of Physical Chemistry A* **2010,** *114* (9), 3355-3370.

35. Hansen, N.; Klippenstein, S. J.; Miller, J. A.; Wang, J.; Cool, T. A.; Law, M. E.; Westmoreland, P. R.; Kasper, T.; Kohse-Höinghaus, K., Identification of C5Hx Isomers in Fuel-Rich Flames by Photoionization Mass Spectrometry and Electronic Structure Calculations. *J. Phys. Chem. A* **2006,** *110* (13), 4376-4388.

36. Yang, B.; Wang, J.; Cool, T. A.; Hansen, N.; Skeen, S.; Osborn, D. L., Absolute photoionization cross-sections of some combustion intermediates. *International Journal of Mass Spectrometry* **2012,** *309*, 118-128.

37. Cool, T. A.; Wang, J.; Nakajima, K.; Taatjes, C. A.; McLlroy, A., Photoionization Cross Sections for Reaction Intermediates in Hydrocarbon Combustion. *Int. J. Mass Spectrom.* **2005,** *247* (1), 18-27.

Chapter 6 VUV Synchrotron Photoionization and Photodissociation Study of Valeric Acid

6.1 Abstract

The unimolecular dissociation of valeric acid was investigated using the i^{2}PEPICO spectrometer at the VUV beamline of the Swiss Light Source at 298 K. Photoelectrons and photoions were imaged and measured simultaneously to determine highly accurate dissociation dynamics in correspondence to a photoionization event. Breakdown diagrams were used to identify accurate appearance energies at 0 K for each daughter ion. The appearance energies, along with known literature values, were then used to determine unknown thermochemical values for the dissociation reaction species. In the 10.2 – 13 eV photon energy range, three daughter ions at m/z = 43, 60, and 73 were found to form from valeric acid. The dissociation is fast and in parallel for all three daughter ions. Using the previously reported $\Delta_fH°$ for valeric acid, the $\Delta_fH°$ ($C_5H_{10}O_2^+$) was calculated to be 499.5± 9.0 kJ/mol. The BDE of the intermediate cation to form $C_2H_4O_2^+$ (m/z = 60) is 111 kJ/mol. The $\Delta_fH°$ ($C_2H_4O_2^+$) was then calculated to be 511.3 ± 9.0 kJ/mol and the heat of formation of the respective intermediate cation is 420.6 ± 9.0 kJ/mol. The calculated BDE of the intermediate cation that forms $C_3H_5O_2^+$ (m/z = 73) is 132 kJ/mol and the heat of formation for the intermediate is 401.6 ± 9.0 kJ/mol. The calculated $\Delta_fH°$ ($C_3H_5O_2^+$) is 414.4 ± 9.0 kJ/mol. Finally, using the previously reported AIE and heat of formation for the propyl radical (C_3H_7*), the calculated heats of formation for the propyl ion ($C_3H_7^+$) and the associated carboxyl radical ($C_2H_3O_2$*) are 880.6 ± 7.0 kJ/mol and -297.6 ± 8.0 kJ/mol, respectively.

6.2 Introduction

Many studies have shown that carbon dioxide emission, specifically from fossil fuel combustion, is one of the largest contributors to the increasing amounts of greenhouse gases (GHG) in the atmosphere.[1-3] Fossil fuel combustion, such as burning gasoline or diesel, also emits particulate matter, complex hydrocarbons, and nitrogen oxides, which are all decreasing air quality.[4-5] Air pollutants have begun and will continue to negatively impact human health and have been linked to lung cancer, cardiovascular disease, and many respiratory illnesses.[6] Apart from air quality concerns, fossil fuel resources are depleting at a rapid rate and the need for an alternative fuel source is imminent.[4]

Currently, the popular potential alternatives include second generation biofuels and biodiesels that are produced in carbon neutral processes from biomass waste and, therefore, do not compete with food production.[7-9] An ideal biofuel and biodiesel would also emit less greenhouse gases in its entire production and combustion cycle. Therefore, studying the compounds and reactivity that occur in producing and utilizing the biofuels and biodiesels is essential to selecting a future fuel for mass consumption.

Biodiesels are EPA approved alternatives to petroleum based fuels that are available on a mass, commercial scale due to two large factors: lower GHG emissions and compatibility with current diesel engines.[10] Numerous studies have shown that combustion of biodiesels produces less hydrocarbons, nitrous oxides, sulfur, and particulate matter, which are all dangerous air pollutants.[7, 10-11] Not only are emissions lower, biodiesels are also non-toxic, biodegradable, and safer.[10] Biodiesels are composed of esters of long chain fatty acids, usually 12 to 24 carbon atoms long.[11] The common method to produce biodiesels is base catalyzed transesterification process of "waste" oils and fats into the biodiesel compounds.[11] Carboxylic acid and alcohol

groups are contained in all of the long chain fatty acids present in the oils and fat compounds of the starting materials.[11-12] Therefore, studying the combustion of simple carboxylic acids, such as valeric acid, can provide insight and a basis for studying these more complex molecules found in biodiesels.

The investigation of the photoionization and photodissociation of valeric acid presented in this study was conducted at the VUV beamline of the Swiss Light Source (SLS) using double imaging photoelectron photoion coincidence spectroscopy (i^2PEPICO). The breakdown diagram of valeric acid was analyzed to determine highly accurate dissociative photoionization onsets as well as the dissociation dynamics of internal energy selected gas phase ions.

6.3 Experimental Methods

The experiment presented here was conducted using the X04DB VUV beamline coupled with the double imaging photoelectron-photoion coincidence (i^2PEPICO) spectrometer at the SLS at the Paul Scherrer Institute. The i^2PEPICO apparatus was in the symmetric set-up, which allowed for both photoelectrons and photoions to be imaged concurrently. Details describing the experimental apparatus has been previously explained elsewhere and only a brief description will be provided here.[13-17]

The purpose of the experiment is to study the unimolecular dissociation dynamics of the chemical of interest by analyzing ions with a selected and specific internal energy. The i^2PEPICO spectroscopy technique, when coupled with the VUV light, allows for the internal energy of a selected ion with a well-defined energy state to be measured.[18] The experimental apparatus measures and images photoelectrons and photoions simultaneously to determine which ions correspond to a photoionization event. The ionization process is shown in the equation below: [19]

$$AB + h\nu \rightarrow AB^{+} (E_{int}) + e^{-} (KE) - IE, \qquad \text{(Equation 6.1)}$$

where $AB^{+} (E_{int})$ is the internal energy of the selected ion and e- (KE) is the kinetic energy of the electron in coincidence.[19]

Valeric acid (purity ≥99%, Sigma-Aldrich) was placed into a glass vial and exposed to a high vacuum to allow the gas in the headspace to be drawn into the experimental apparatus. The gas was sampled through a simple nozzle technique designed by Buckland et al.,[20] which allowed for the formation of a molecular beam. The molecular beam was then narrowed by the 1 mm slit of an in-house designed skimmer before entering the experimental chamber to intersect with the light beam for the ionization process.[15, 17] The reaction was carried out at room temperature and pressure was maintained at 10^{-6} mbar by a needle valve. [21] A gas filter made up of nine differentially pumped sections filled with neon as a backing gas was used to suppress higher harmonic radiation resulting from the synchrotron light.[21] The source chamber maintained a pressure of 5×10^{-7} mbar was regulated by a 1500 L/s turbomolecular pump and a 5000 L/s cryogenic pump.[21]

After ionization, a photoelectron triggers the ion time-of-flight analysis and photoions and photoelectrons are pushed in opposite directions by a 120 V/cm electric field to individual Roentdek DLD40 delay line detectors.[15, 22] The electrons and ions of interest in this study, known as zero kinetic energy electrons (ZKE) and "cold ions", are those that move in a straight line and hit the center of their respective detectors. ZKE and "cold ions" correspond to a photoionization event and, therefore, considered to be in coincidence.[15] Electrons and ions that move at an angle and do not hit the center of the detector are later subtracted out of velocity map imaging during data analysis.

Electron velocity map images (VMI) are produced from an in-house program designed by Dr. Andras Bodi.[23] The i^{2}PEPICO program is used to visualize the raw data produced from the experimental apparatus based on mapping information of the photoelectron collision site with the detector and the TOF-MS of the photoions.[23] A customizable input script is optimized to best visualize the signal produced from the multichannel analyzer that counts the total number of active channels that give number points.[23] From the electron VMI, a list of coincidence counts is given as a series of numbers that is then extrapolated to determine the count of ZKE electrons.[23] From the ZKE electron counts, fractional abundances for each mass-to-charge ratio are plotted as a function of photon energy following subtraction of background noise signal to produce a breakdown diagram.[23] The photodissociation reaction presented here is regarded as fast dissociation since 100% of the parent cation dissociates within the experimental time frame. Therefore, a fitted model of the theoretical breakdown curve alone is needed to determine the 0 K appearance energy for the reaction species.[18-19, 24]

6.4 Computational Methods

All theoretical calculations presented in this work are performed using Gaussian 09 software suite.[25] Electron structure calculations, including vibrational and rotational constants, were calculated using the CBS-QB3 composite method.[26-27] Potential energy surface (PES) scans are computed using the B3LYP/6-31G(d) level of theory and used to determine dissociation pathways to identify barriers and transition states.[28] All transition and intermediate state cation compounds identified through PES scans are optimized using the CBS-QB3 composite method and all resulting energy values are reported at 0 K.[26-27]

Following the ionization process, an initial parent cation (AB^+) forms from a neutral valeric acid (AB), that then dissociates into cationic (A^+) and neutral (B) fragments. An example of the complete ionization and dissociation reaction is shown by the equation below:

$$AB + hv \rightarrow AB^+ \rightarrow A^+ + B \qquad \text{(Equation 6.2)}$$

As the initial cation of valeric acid (AB^+) depletes, daughter cations start forming at their relative appearance energy (AE) values.[17] The AE of the daughter ion is determined using the miniPEPICO program.[29] When no dissociation barriers are present or the PES scan determines the mechanism is "uphill", the bond dissociation energy (BDE) can represent the AE of the cation fragment.[18, 29] This is also called thermochemical limit. "Uphill" scans are present in all three dissociation pathways of the daughter ions presented here. AE and BDE are calculated by the equations below:

$$BDE\ (AB^+) = E(\text{fragments}) - E(\text{cation parent}) \qquad \text{(Equation 6.3)}$$

$$AE = AIE + BDE = E(\text{fragments}) - E(\text{neutral parent}) \qquad \text{(Equation 6.4)}$$

where AIE is the adiabatic ionization energy of the parent molecule.

MiniPEPICO computational program is used to produce a theoretical model to best fit to the experimental breakdown diagram.[29] The program uses the RRKM theory to calculate the thermal energy distribution of ions as a function of photon energy while accounting for dissociation rates.[29-30] The rotational and vibrational frequencies of the optimized transition states and parent's neutral and cationic form are entered into the program to calculate dissociation rates.[17, 29] The photodissociation of valeric acid forms three daughter cation fragments in a parallel mechanism, which is also specified in the program. Theoretical dissociation curves for each cation fragment (A^+) are then fitted to the experimental curves to

identify accurate AE of each daughter cationic fragment (A^+). The AE values of all the daughter ions are then used to determine overall thermochemistry values.

The determined AE and literature enthalpy values for the known compounds can be used to determine thermochemical values for any unknown compounds. Here, the thermochemical values for the neutral (B) fragments and valeric acid are known and will be used to solve for the unknown values for the cationic (A^+) daughter fragments and the cationic (AB^+) parent molecule. An outline of the calculation work flow is shown by the following equations: [19, 24]

$$AE - AIE + \Delta [E(AB^+) - E(I^+)] = BDE^o_{0K}(A^+ - B) \quad \text{(Equation 6.5)}$$

$$BDE^o_{0K}(A^+ - B) = \Delta_f H°(B) + \Delta_f H°(A^+) - \Delta_f H°(AB^+) \quad \text{(Equation 6.6)}$$

$$\Delta_f H°(AB^+) = \Delta_f H°(B) + \Delta_f H°(A^+) - BDE^o_{0K}(A^+ - B) \quad \text{(Equation 6.7)}$$

$$\Delta_f H°(\text{Valeric Acid}) = \Delta_f H°(AB^+) - AIE \quad \text{(Equation 6.8)}$$

The BDE and AIE values along with the calculated energy (E) values of the intermediate cation (I^+) that forms the final products are used to determine AE and enthalpy of formation values as described by the equations above.[19, 24] The enthalpy of formation of the neutral parent, valeric acid, is used with the experimental AIE to calculate the enthalpy of formation of the cationic parent (AB^+) for a given dissociation pathway.

6.5 Results

The photoionization and photodissociation of valeric acid were conducted at room temperature and a pressure of 10^{-6} mbar over a 10.2 to 13 eV range with a 120 V/cm electric field. Three daughter cationic fragments were found to form in a parallel dissociation mechanism following the initial ionization of valeric acid. The general schematic of the photodissociation is shown below.

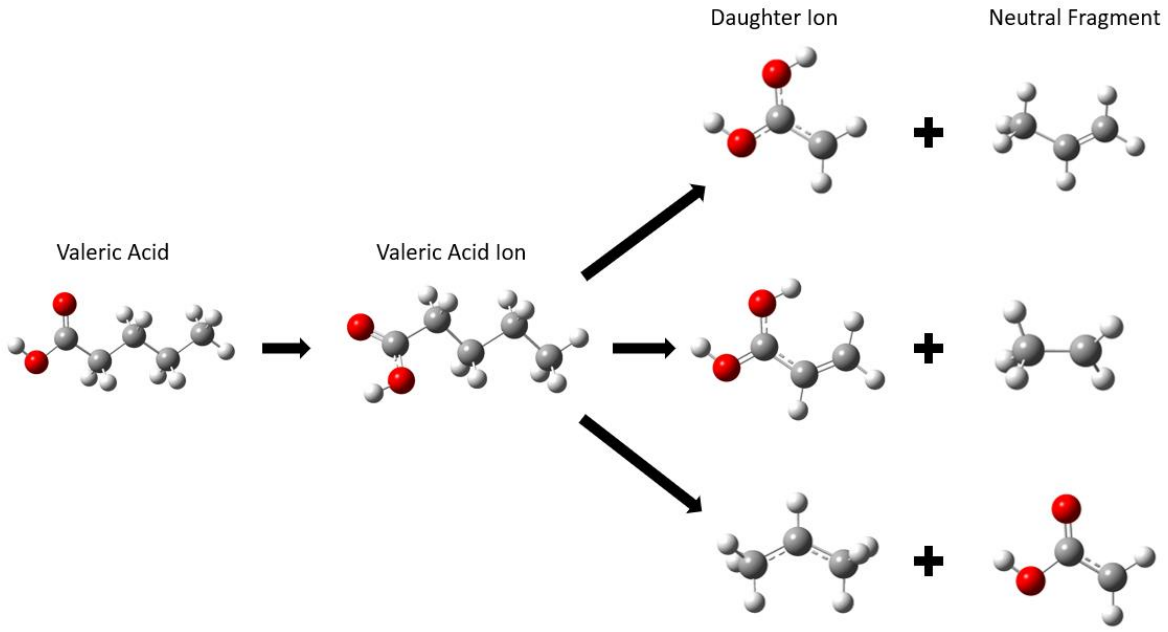

Scheme 6.1 General schematic for the photoionization and photodissociation of valeric acid at 298 K.

The breakdown diagram in Figure 6.1 shows that over the 10.2 -13 eV energy range, valeric acid (VA^+, m/z = 102) cations decay in a parallel mechanism into the three daughter ions: $C_2H_4O_2^+$ (m/z = 60), $C_3H_5O_2^+$ (m/z = 73), and $C_3H_7^+$ (m/z = 43). The theoretical breakdown curve (shown by the solid line) was modeled in the miniPEPICO program and optimized at 300 K for the best fit. Rotational and vibrational frequencies of the optimized structure of valeric acid were entered into the miniPEPICO input file as well as the vibrational frequencies of the parent cation. Using PES scans, the vibrational frequencies from the highest energy intermediate or transition state cations in the relative dissociation pathway for the formation of each daughter ion were also inputted into the program. Further details will be given below.

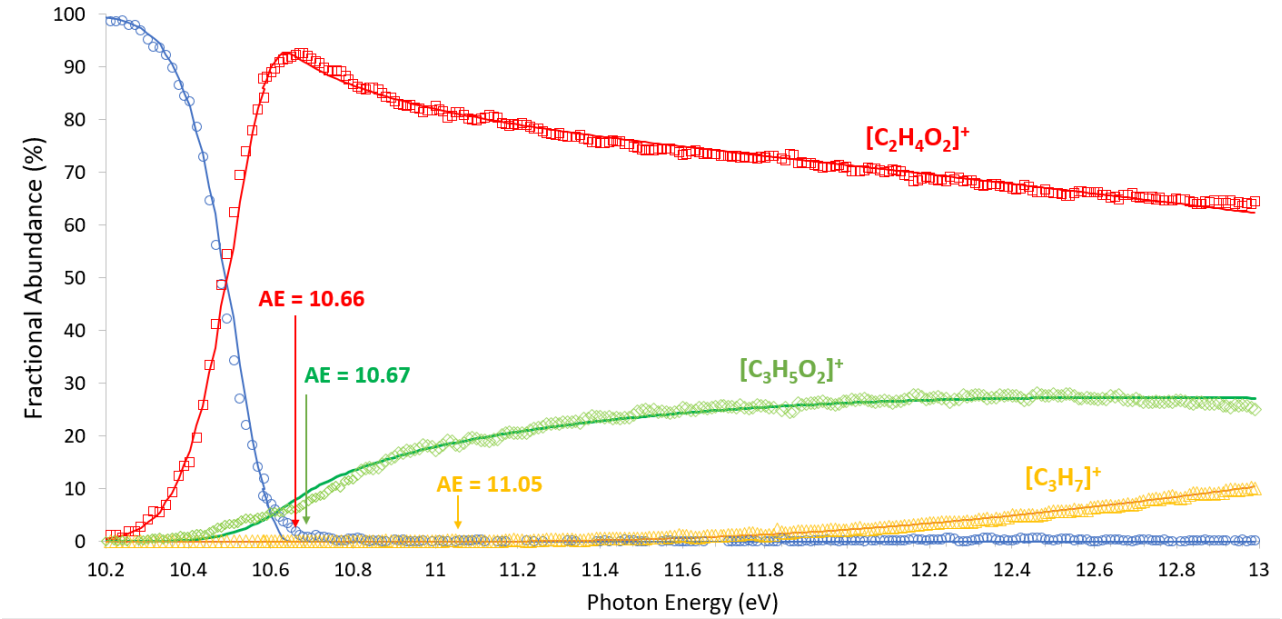

Figure 6.1 Breakdown diagram for the dissociation of valeric acid over the 10.2 – 13 eV photon energy range. The experimental data points are shown by the open shapes and the solid lines are the theoretical dissociations calculated from the miniPEPICO program.

Following the fast dissociation of the $C_2H_{10}O_2^+$ parent ion, the $C_2H_4O_2^+$ (m/z = 60) and $C_3H_5O_2^+$ (m/z = 73) daughter ions begin to form in parallel through differentiating mechanisms described below. The AE at 0K for $C_2H_4O_2^+$ (m/z = 60) and $C_3H_5O_2^+$ (m/z = 73) are 10.66 ± 0.025 eV and 10.67 ± 0.025 eV, respectively. The third daughter ion, $C_3H_7^+$ (m/z = 43), begins to form with a low intensity after 11 eV and has AE of 11.05 ± 0.025 eV at 0 K. The possible sequential dissociation pathways to form $C_3H_7^+$ (m/z = 43) as a granddaughter ion from either $C_2H_4O_2^+$ (m/z = 60) or $C_3H_5O_2^+$ (m/z = 73) was also investigated. However, the dissociation pathways were found to be thermodynamically unfeasible. Therefore, the fragment must also be forming in parallel with the other two daughter ions.

The PES diagrams in Figure 6.2 show the dissociation pathways for valeric acid resulting in the three identified daughter ions. When the pathways were found to be barrierless or "uphill", the AIE of products will serve as the BDE for the associated dissociation pathway.

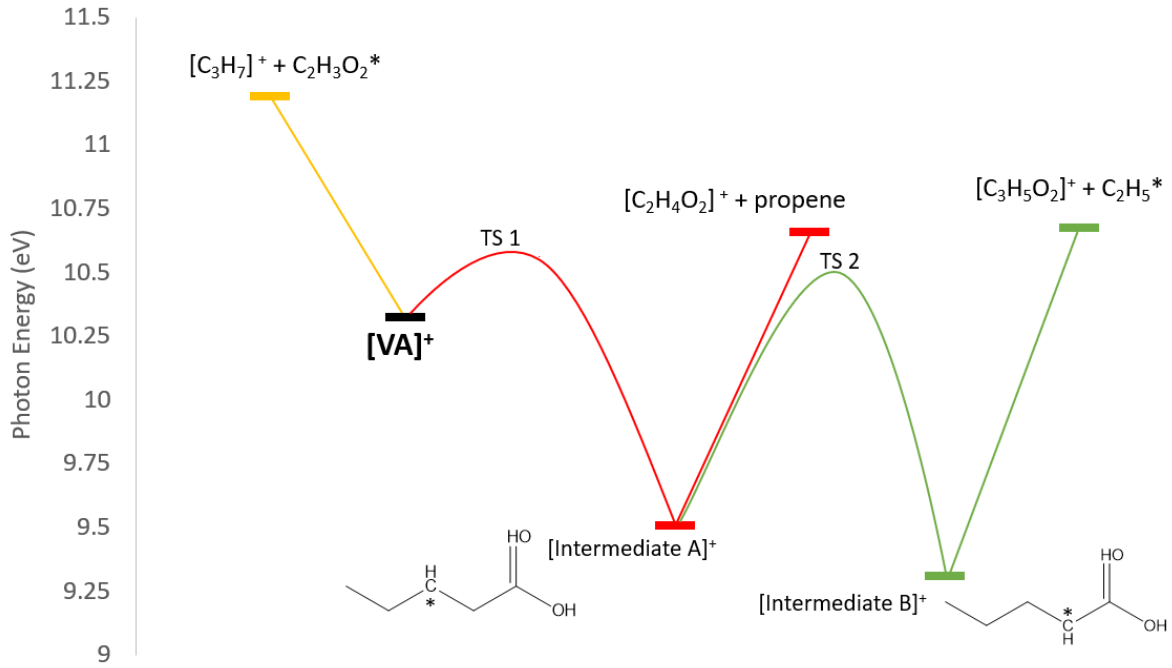

Figure 6.2 Potential energy surface diagrams for the parallel dissociation pathways of valeric acid cation.

To form the daughter ion at m/z = 60, the parent ion, $C_2H_{10}O_2^+$, undergoes a hydrogen transfer from the γ-carbon to the oxygen with a transition state barrier (TS 1) of 23.6 kJ/mol that results in intermediate cation A at 78.9 kJ/mol below the parent ion ($C_2H_{10}O_2^+$) . From the intermediate cation, the bond between the γ-carbon and β-carbon breaks to form the ethylene diol ($C_2H_4O_2^+$) daughter ion and propene as the neutral fragment. This pathway is "uphill" and results in the highest energy point, therefore, the BDE of the two products will serve as the dissociation barrier. The daughter ion at m/z = 73 also forms from intermediate A cation after a hydrogen transfer from the β-carbon to γ-carbon with a transition state barrier (TS 2) of 96.1 kJ/mol forming intermediate B cation with an overall exothermicity of 97.9 kJ/mol. The bond between the γ-carbon and Δ-carbon is then cleaved to form the daughter ion, $C_3H_5O_2^+$, and an ethyl radical (C_2H_5*) as the neutral fragment. The third daughter ion, $C_3H_7^+$, optimizes and forms directly from the parent cation, $C_2H_{10}O_2^+$, in an "uphill" mechanism by the cleavage of the β-

carbon to γ-carbon. The associated neutral fragment is a carboxyl radical ($C_2H_3O_2$*). In the three presented pathways, the products are the highest overall energy points, therefore, the BDE will be relative to the energetics of the intermediate that directly proceeds to product formation. The formation of the intermediates from the parent cation VA^+ occurs through an energy barrier below the fragments. Therefore, the BDE is relative to intermediate A cation for m/z = 60 and intermediate B cation for m/z = 73. For m/z = 43, the difference between the AIE(parent) and the AE(fragment) will serve as the dissociation barrier.

The decomposition of the valeric acid to form the daughter ion at m/z = 43 could have formed compounds with the general formula C_2H_3O with theoretical AE values close to the observed experimental values as a daughter or granddaughter ion. However, the PES scans to form C_2H_3O conformations from the parent ion as well as the two daughter ions at m/z = 60 and m/z = 73 were not thermodynamically feasible or did not result in the desired conformation. The attempted pathways included removal of the alcohol group (-OH) and hydrogen transfers to the beta carbon in all three ions.

6.6 Thermochemistry

Equations 6.5-6.8 will be used to calculate unknown thermochemical values for the applicable reaction species using thermochemical values from literature and the experimentally determined BDE values at 0 K. Adriaanse et al.[31] previous reported the heat of formation of valeric acid is -496.5 ± 4.1 kJ/mol. Using Equation 6.8, the heat of formation of the valeric acid cation is calculated to be 499.55 ± 5.0 kJ/mol. The heat of formation values for propene (m/z = 42), ethyl radical (m/z = 29), and propyl ion ($C_3H_7^+$) (m/z = 43) were also reported in previous studies and will be used to determine the unknown thermochemical values for the identified dissociation reaction species.

Using the calculated energy value of [Intermediate A]$^+$, the BDE of [Intermediate A]$^+$ is computed to be 111 kJ/mol. The reported heat of formation for propene is 20.41± 0.33 kJ/mol and was used to determine that the $\Delta_fH°$ ($C_2H_4O_2^+$) = 511.3 kJ/mol ± 9.0 kJ/mol.[32] For this dissociation pathway, the $\Delta_fH°$ (Intermediate A^+) can also be calculated and is 420.6 ± 9.0 kJ/mol.

Similarly, the $\Delta_fH°$ (C_2H_5*) was previously reported by Tsang et al.[33] to be 119 ± 6.0 kJ/mol. With this value and the calculated BDE of 132 kJ/mol for [Intermediate B]$^+$, the $\Delta_fH°$ ($C_3H_5O_2^+$) is found to be 414.4 ± 9.0 kJ/mol. The heat of formation for [Intermediate B]$^+$ could then be resolved and is determined to be 401.6 ± 9.0 kJ/mol.

For the final dissociation pathway which forms the propyl ion ($C_3H_7^+$) at m/z = 43, the heat of formation for the propyl ion and the associated neutral carboxyl radical ($C_2H_3O_2$*) can be calculated. The heat of formation and AIE of the propyl radical have been previously reported to be 100 kJ/mol ± 2.0 kJ/mol and 8.09 ± 0.01 eV, respectively.[33-34] With these values, the heat of formation of the propyl ion is calculated to be 880.6 ± 8.0 kJ/mol and the heat of formation of the carboxyl radical is computed to be -297.6 ± 8.0 kJ/mol.

6.7 Conclusions

In the investigation presented here, the unimolecular dissociation of valeric acid was studied using the i^{2}PEPICO spectrometer at the VUV beamline of the Swiss Light Source at 298 K for the 10.2 – 13 eV range. The i^{2}PEPICO apparatus was in the symmetric set-up and photoelectrons and photoions were imaged and measured simultaneously. Therefore, when coupled with VUV light, the internal energy of a selected ion with a well-defined energy state was able to be measured and used to determine which ions corresponded to a photoionization event. Theoretical and experimental breakdown diagrams were used to determine accurate the

AE at 0 K for the three daughter ions and unknown thermochemical values for the dissociation reaction species. The heat of formation of the valeric acid cation was calculated to be 499.5 ± 5.0 kJ/mol. Using the AE of 10.66 eV for the daughter ion at m/z = 60 and computed energy values, the and the BDE of [Intermediate A]$^+$ was found to be 111 kJ/mol. The $\Delta_f H°$ ($C_2H_4O_2^+$) was then calculated to be 511.3 kJ/mol ± 9.0 kJ/mol and the $\Delta_f H°$ (Intermediate A^+) to be 420.6 ± 9.0 kJ/mol. Similarly, using the AE of 10.67 eV for the daughter ion at m/z = 73 and the calculated BDE of 132 kJ/mol for [Intermediate B]$^+$, the $\Delta_f H°$ ($C_3H_5O_2^+$) = 414.4 ± 9.0 kJ/mol and the $\Delta_f H°$ (Intermediate B^+) = 401.6 ± 9.0 kJ/mol. The third daughter ion at m/z = 43 has an appearance energy of 11.05 eV and a calculated heat of formation of 880.6 ± 7.0 kJ/mol. The heat of formation for the carboxyl radical ($C_2H_3O_2$*) was also calculated to -297.6 ± 7.0 kJ/mol.

6.8 Acknowledgements

This work was funded by the American Chemical Society–Petroleum Research Grant #56067-UR6 and the University of San Francisco Faculty Development Fund. The double imaging photoelectron photoion coincidence experiment was performed at the Swiss Light Source at the Paul Scherrer Institut in Villigen, Switzerland through funding by the Swiss FederalOffice for Energy (BFE Contract 101969/152433) and the National Science Foundation (CHE-1266407).

6.9 References

1. Agency, U. S. E. P. Climate Change: Basic Information. https://19january2017snapshot.epa.gov/climatechange/climate-change-basic-information_.html.
2. Droege, P., Renewable Energy and the City: Urban Life in an Age of Fossil Fuel Depletion and Climate Change. *Bulletin of Science, Technology & Society* **2002,** *22* (2), 87-99.
3. Gaffney, J. S.; Marley, N. A., The impacts of combustion emissions on air quality and climate – From coal to biofuels and beyond. *Atmospheric Environment* **2009,** *43* (1), 23-36.
4. Höök, M.; Tang, X., Depletion of fossil fuels and anthropogenic climate change—A review. *Energy Policy* **2013,** *52*, 797-809.
5. Klass, D. L., Energy Consumption, Reserves, Depletion, and Environmental Issues. In *Biomass for Renewable Energy, Fuels, and Chemicals*, Academic Press: San Diego, 1998; pp 1-27.
6. Agency, U. S. E. P. Climate Changes Impacts on Human Health.

7. Kohse-Höinghaus, K.; Oßwald, P.; Cool, T. A.; Kasper, T.; Hansen, N.; Qi, F.; Westbrook, C. K.; Westmoreland, P. R., Biofuel Combustion Chemistry: From Ethanol to Biodiesel. *Angewandte Chemie International Edition* **2010,** *49* (21), 3572-3597.
8. Naik, S. N.; Goud, V. V.; Rout, P. K.; Dalai, A. K., Production of first and second generation biofuels: A comprehensive review. *Renewable and Sustainable Energy Reviews* **2010,** *14* (2), 578-597.
9. Schenk, P. M. T.-H., S.R.; Stephens, E.; Marx, U. C.; Mussgnug, J. H.; Posten, C.; Kruse, O.; Hankamer, B., Second Generation Biofuels: High-Efficiency Microalgae for Biodiesel Production. *Bioenerg. Res.* **2008,** *1* (1), 20-43.
10. Biodiesel Biodiesel Basics. https://www.biodiesel.org/what-is-biodiesel/biodiesel-basics.
11. Unit, E. S. R. What is Biodiesel. http://www.esru.strath.ac.uk/EandE/Web_sites/02-03/biofuels/what_biodiesel.htm.
12. Clark, J. M.; Nimlos, M. R.; Robichaud, D. J., Comparison of Unimolecular Decomposition Pathways for Carboxylic Acids of Relevance to Biofuels. *The Journal of Physical Chemistry A* **2014,** *118* (1), 260-274.
13. Shuman, N. S.; Stevens, W. R.; Lower, K.; Baer, T., Heat of Formation of the Allyl Ion by TPEPICO Spectroscopy. *The Journal of Physical Chemistry A* **2009,** *113* (40), 10710-10716.
14. Borkar, S. N. Very Accurate Gas-Phase Thermochemistry Through Photoelectron

Photoion Coincidence (PEPICO) Spectroscopy. University of the Pacific, Stockton, California, 2013.
15. Bodi, A.; Johnson, M.; Gerber, T.; Gengeliczki, Z.; Sztáray, B.; Baer, T., Imaging photoelectron photoion coincidence spectroscopy with velocity focusing electron optics. *Review of Scientific Instruments* **2009,** *80* (3), 034101.
16. Johnson, M.; Bodi, A.; Schulz, L.; Gerber, T., Vacuum ultraviolet beamline at the Swiss Light Source for chemical dynamics studies. *Nuclear Instruments and Methods in Physics Research Section A: Accelerators, Spectrometers, Detectors and Associated Equipment* **2009,** *610* (2), 597-603.
17. Winfough, M.; Voronova, K.; Muller, G.; Laguisma, G.; Sztáray, B.; Bodi, A.; Meloni, G., Furfural: The Unimolecular Dissociative Photoionization Mechanism of the Simplest Furanic Aldehyde. *The Journal of Physical Chemistry A* **2017,** *121* (18), 3401-3410.
18. Baer, T.; Sztáray, B.; Kercher, J. P.; Lago, A. F.; Bödi, A.; Skull, C.; Palathinkal, D., Threshold photoelectron photoion coincidence studies of parallel and sequential dissociation reactions. *Physical Chemistry Chemical Physics* **2005,** *7* (7), 1507-1513.
19. Baer, T., Ion dissociation dynamics and thermochemistry by photoelectron photoion coincidence (PEPICO) spectroscopy. *International Journal of Mass Spectrometry* **2000,** *200* (1), 443-457.
20. Buckland, J. R.; Folkerts, R. L.; Balsod, R. B.; Allison, W., A simple nozzle design for high speed-ratio molecular beams. *Measurement Science and Technology* **1997,** *8* (8), 933.
21. VUV Photoionizaition Overview. Institute, P. S., Ed. Villigen PSI, Switzerland.
22. Bouwman, J.; Sztáray, B.; Oomens, J.; Hemberger, P.; Bodi, A., Dissociative Photoionization of Quinoline and Isoquinoline. *The Journal of Physical Chemistry A* **2015,** *119* (7), 1127-1136.
23. Bodi, A. *i2PEPICO software tools*.
24. Mazyar, O. A.; Mayer, P. M.; Baer, T., Isomerization and dissociation in competition: the two-component dissociation rates of methyl acetate ions. *International Journal of Mass Spectrometry and Ion Processes* **1997,** *167-168*, 389-402.
25. Frisch, M. J. T., G. W.; Schlegel, H. B.; Scuseria, G. E.; Robb, M. A.; Cheeseman, J. R.; Scalmani, G.; Barone, V.; Petersson, G. A.; Nakatsuji, H. et. al. *Gaussian 09*, Gaussian Inc.: Wallingford CT, 2009.
26. Montgomery, J. A., Jr.; Frisch, M. J.; Ochterski, J. W.; Petersson, G. A., A Complete Basis Set Model Chemistry. VII. Use of the Minimum Population Localization Method. *J. Chem. Phys.* **2000,** *112* (15), 6532-6542.

27. Montgomery, J. A., Jr.; Frisch, M. J.; Ochterski, J. W.; Petersson, G. A., A Complete Basis Set Model Chemistry. VI. Use of Density Functional Geometries and Frequencies. *J. Chem. Phys.* **1999,** *110* (6), 2822-2827.
28. Tirado-Rives, J.; Jorgensen, W. L., Performance of B3LYP Density Functional Methods for a Large Set of Organic Molecules. *J. Chem. Theory Comput.* **2008,** *4* (2), 297-306.
29. Sztáray, B.; Bodi, A.; Baer, T., Modeling unimolecular reactions in photoelectron photoion coincidence experiments. *Journal of Mass Spectrometry* **2010,** *45* (11), 1233-1245.
30. Di Giacomo, F., A Short Account of RRKM Theory of Unimolecular Reactions and of Marcus Theory of Electron Transfer in a Historical Perspective. *Journal of Chemical Education* **2015,** *92* (3), 476-481.
31. Adriaanse, N.; Dekker, H.; Coops, J., Heats of combustion of normal saturated fatty acids and their methyl esters. *Recueil des Travaux Chimiques des Pays-Bas* **1965,** *84* (3), 393-407.
32. Furuyama, S.; Golden, D. M.; Benson, S. W., Thermochemistry of the gas phase equilibria i-C3H7I , C3H6 + HI, n-C3H7I , i-C3H7I, and C3H6 + 2HI , C3H8 + I2. *The Journal of Chemical Thermodynamics* **1969,** *1* (4), 363-375.
33. Tsang, W., *Heats of Formation of Organic Free Radicals by Kinetic Methods*. Energetics of Organic Free Radicals: Springer, Dordrecht, 1996; Vol. 4.
34. Dyke, J.; Ellis, A.; Jonathan, N.; Morris, A., Vacuum ultraviolet photoelectron spectroscopy of transient species. Part 18.—The cyclopropyl, isopropyl and n-propyl radicals. *Journal of the Chemical Society, Faraday Transactions 2: Molecular and Chemical Physics* **1985,** *81* (10), 1573-1586.